UNIVERSITY OF STRATHCLYDE
DEPARTMENT OF PHYSICS

Intra-pulse dynamics of laser-driven ion acceleration in ultra-thin foils

by

Hersimerjit Padda

in partial fulfilment of the requirements for the degree of Doctor of Philosophy in Physics

2017

Copyright Declaration

This thesis is the result of the author's original research. It has been composed by the author and has not been previously submitted for examination which has led to the award of a degree.

Signed:

Date:

Abstract

This thesis reports on experimental and numerical investigations of ion acceleration driven by the interaction of short, intense laser pulses with ultra-thin, solid targets in which relativistic transparency is induced. In particular, it explores the multiple laser-ion acceleration mechanisms that take place over the duration of the laser pulse. Investigating these acceleration mechanisms is important for understanding the underlying physical dynamics and optimising laser-driven ion acceleration.

The investigations featured in this thesis result from intense laser-solid interactions conducted at the Rutherford Appleton Laboratory, using the Vulcan Petawatt laser system. The first investigation explores the spatial-intensity profile of the proton beam accelerated from thin (tens of nanometre) aluminium targets. The beam of accelerated protons displayed a variety of features, including a low-energy annular profile, a high energy component with a small divergence and Rayleigh-Taylor-like instabilities. A particularly interesting observation is the low-energy annular profile, which is shown to be sensitive to target thickness and proton energy.

Numerical investigations using particle-in-cell (PIC) simulations exhibit the same trends and demonstrate that the radiation pressure from the laser pulse drives an expansion of the target ions within the spatial extent of the laser focal spot. This induces a radial deflection of relatively low energy sheath-accelerated protons to form an annular distribution. Through variation of the target foil thickness, the opening angle of the ring is shown to be correlated to the point in time during the laser pulse interaction at which the target becomes transparent to the laser (in a process termed relativistic induced transparency). The ring is largest when transparency occurs close to the peak of the laser intensity.

The second investigation focuses on the rising edge profile of the laser pulse and the correlation between its temporal width and the resultant maximum proton

energy. An important parameter to consider when irradiating nanometre-thick foils is the laser contrast. However, the effect of the temporal width of the laser pulse at 1% of the peak, where the intensity is $\sim 10^{18}$ Wcm^{-2}, has not been previously explored. Using CH targets with a fixed thickness, a range of proton energies, from 20-70 MeV, are measured experimentally. The temporal width of the laser pulse is measured using a second order autocorrelator and is used to model the rising edge of the laser pulse on target. The temporal width at 50%, 10% and 1%, of the peak of the pulse, is measured. The measured proton energies are found to strongly correlate with the temporal width at the 1% level, and as the duration at this pulse width increased the maximum proton energy decreased.

Using particle-in-cell simulations, a detailed numerical investigation is carried out to understand the effect the rising edge of the laser pulse has on proton energies. By increasing the temporal width at 1%, the expansion of the target increased, resulting in a less efficient acceleration of protons. Furthermore, by inducing a small expansion in the target before the peak of the pulse arrives, the hole boring mechanism of RPA can be optimised along the laser axis. However, in the case where the temporal width at 1% is relatively larger, the hole boring mechanism no longer dominates the interaction, as the target undergoes relativistic induced transparency on the rising edge of the pulse, limiting the effect of hole boring. Improving the laser contrast on the picosecond time-scale could result in higher and stable proton energy.

Acknowledgements

The completion of this thesis and work presented within could not have been done without the help and support of a number of people.

First and foremost, I would like to thank my supervisor, Prof. Paul McKenna, for his constant advice, guidance, encouragement and support throughout my PhD and for giving me the chance to work in a friendly and stimulating environment. I will always be grateful to him for believing in me and offering me the possibility of talking part in this cutting-edge research.

I would also like to thank Dr. Ross Gray for all his support during experiments throughout my PhD and having patience when I did not understand concepts straight away. Also, a big thank you to Dr. Martin King for his plasma physics expertise, and helping perform and interpret the PIC simulations presented in this thesis. Thanks to Remi for providing theoretical knowledge when I was struggling to understand complex physics.

I would also like to say a massive thank you to the guys I had the pleasure of sharing an office with, Bruno, Haydn, Matthew and Nick. The constant banter and coffee breaks will be missed. I would additionally like to thank my friends and colleagues in the group, Adam, Chris, Dean, Graeme, Katie, Rachel, Sam and Zoe.

Also, I would like to thank the collaborators who I have worked with over the past 4 years; Clare, Aaron, Deborah, Domineco, Satya and Marco at Queens University Belfast, Oliver, George and Zulfikar at Imperical College London, Luca from the Centro de Laseres Pulsados (CLPU) and David Carroll and David Neely from the Central Laser Facility (CLF). I would also like to thank the CLF staff and the Vulcan laser team, without whom the experimental campaigns providing the data presented here would not have been possible.

Outside of PhD life I'd like to thank all my friends that had to deal with me talking about physics for the past three years. A special mention to the united

nation of jobbies group, Chris, Jonathan and Muneeb for all of the weekends away travelling. JOBBY!!!! Also, Callum, Laura and Steven for providing countless nights of alcohol and banter.

Finally, I would like to thank my family for their complete support throughout my entire life and constantly encouraging me. Without you I would not be where I am today.

Publications

1. Intra-pulse transition between ion acceleration mechanisms in intense laser-foil interactions

H. Padda, M. King, R. J. Gray, H. W. Powell, B. Gonzalez-Izquierdo, L. C. Stockhausen, R. Wilson, D. C. Carroll, R. J. Dance, D. A. MacLellan, X. H. Yuan, N. M. H. Butler, R. Capdessus, R. Torres, M. Borghesi, D. Neely, and P. McKenna. *Physics of Plasmas* **23**, 063116, 2016

2. Laser contrast effects on laser-driven proton energies in the relativistic induced transparency regime

H. Padda, M. King, R. J. Gray, A. Alejo, C. Armstrong, D. C. Carroll, R. J. Dance, N. P. Dover, O. C. Ettlinger, A. Higginson, C. Scullion, R. Wilson, S. Kar, Z. Najmudin, M.Borghesi, D. Neely, and P. McKenna. (In preparation)

3. Enhanced laser energy coupling to protons via a self-generated plasma channel in the relativistic-transparency regime

H. W. Powell, M. King, R. J. Gray, D. A. MacLellan, B. Gonzalez-Izquierdo, L. C. Stockhausen, G. Hicks, N. P. Dover, D. R. Rusby, D. C. Carroll, **H. Padda**, R. Torres, S. Kar, R. J. Clarke, I. O. Musgrave, Z. Najmudin, M. Borghesi, D. Neely, and P. McKenna. *New Journal of Physics* **17**, 103033, 2015

4. Ion acceleration and plasma jet formation in ultra-thin foils undergoing expansion and relativistic transparency

M. King, R. J. Gray, H. W. Powell, D. A. MacLellan, B. Gonzalez-Izquierdo, L. C. Stockhausen, G. Hicks, N. P. Dover, D. R. Rusby, D. C. Carroll, **H. Padda**, R. Torres, S. Kar, R. J. Clarke, I. O. Musgrave, Z. Najmudin, M. Borghesi, D. Neely, and P. McKenna. *Nuclear Instruments and Methods in Physics Research Section A: Accelerators, Spectrometers, Detectors and Associated Equipment* **829**, 163,

2016

5. Angularly resolved characterization of ion beams from laser-ultrathin foil interaction

C. Scullion, D. Doria, L. Romagnani, H. Ahmed, A. Alejo, O. C. Ettlinger, R. J. Gray, J. Green, G. S. Hicks, D. Jung, K. Naughton, **H. Padda**, K. Poder, G. G. Scott, D. R. Symes, S. Kar, P. McKenna, Z. Najmudin, D. Neely, M. Zepf, M. Borghesi. Journal of instrumentation **11**, 09, C09020, 2016

6. Laser accelerated ultra high dose rate protons induced DNA damage under hypoxic conditions

P. Chaudhary, D. Gwynne, D. Doria, L. Romagnani, C. Maiorino, **H. Padda**, A. Alejo, N. Booth, D. Carroll, S. Kar, P. McKenna, M. Borghesi, K.M. Prise. Radiotherapy and Oncology, 118, S24-S25, 2016

7. Time of Flight based diagnostics for high energy laser driven ion beams

V. Scuderi, G. Milluzzo, A. Alejo, A.G. Amico, N. Booth, G.A.P. Cirrone, D. Doria, J. Green, S. Kar, G. Larosa, R. Leanza, D. Margarone, P. McKenna, **H. Padda**, G. Petringa, J. Pipek, L. Romagnani, F.Romano, F. Schillaci, M. Borghesi, G. Cuttone, G. Korn. Journal of instrumentation **12**, 03, C03086-C03086, 2017

Role of the author

Throughout this PhD study, the author gained experience in the design, planning and implementation of experimental campaigns. The work presented in this thesis primarily involved the use of the Vulcan Petawatt laser system at the Central Laser Facility, but the author also contributed to experiments using the Astra-Gemini laser system.

Chapter 5: The author played a key role during the the experimental campaign. The target area operations were led by Dr. R. J. Gray (University of Strathclyde) and Dr. H. W. Powell (University of Strathclyde). The author was responsible for installing and running the Thomson parabola spectrometer, dosimetry stack, and scanning image plate, with help from Dr. L. C. Stockhausen (CLPU) and Dr. H. W. Powell. Dr. B. Gonzalez-Izquierdo (University of Strathclyde) set up the transmission diagnostic and helped with the collection of data. The analysis and processing of the data from the Thomson parabola spectrometer, dosimetry stack and laser transmission diagnostics after the experiment was carried out by the author. The author played a leading role in running and analysing the initial 2D simulation study. Additional 2D and 3D simulations presented were carried out by Dr. M. King (University of Strathclyde) and analysed by the author.

Chapter 6: The author played a central role in planning and running the main experimental diagnostics. The target area operations were led by Dr. R. J. Gray and Dr. R. J. Dance (University of Strathclyde). The author was responsible for the installation of the key diagnostics of the campaign; three Thomson parabola spectrometers and dosimetry stacks. The image plate and dosimetry stack were scanned and analysed by the author. The 2D PIC simulations and initial analysis was carried out by Dr. M. King and analysis was done by the author. The author fully analysed the data presented in this thesis and contributed to writing the publications resulting from this work.

Contents

List of Figures

List of Tables

Chapter 1

Introduction

Accelerators have been at the forefront of science since the 1920s, providing scientists with the necessary tools to undertake research in many fields of physics and understand the building blocks of matter itself. Presently, laboratory accelerators are used to create conditions that occurred shortly after the big bang enabling physicists to probe the deepest mysteries of the universe. Other uses of accelerators include, serving as tools for medical and industrial applications and nuclear energy.

Early particle accelerators such as the Cockcroft-Walton generator or the Van de Graaff generator utilised static electric fields to accelerate particles to energies. In the 1920s a Norwegian physicist, Rolf Wideroe first proposed the linear particle accelerator using a series of oscillating electric fields to accelerate charged particles along the beam line [6]. This device, known as a linac, accelerated particles up to energies of keV. Around 10 years later Ernest Lawrence came across Wideroe's article and was intrigued by the concept of particle acceleration [7]. Lawrence built an alternative accelerator which used a circular path with electromagnets to guide particles along a circular path instead of a linear beam line. This device, called a cyclotron, was only 10 cm in diameter and could be held in one hand. In the present day, these accelerators have increased in size and still provide a lot of

science for researchers.

Modern day accelerators are generally based on radio-frequency (RF) cavities creating oscillating fields to keep particles in phase with the accelerating field. However, the electrical breakdown which occurs in the metal walls of the cavity which limits the maximum accelerating gradient possible to tens of MV/m. To overcome this and increase the energy of particles, the spacing of electrodes and thus the accelerator size is increased. The Large Hadron Collider (LHC) is a synchrotron accelerator with a 27 km circumference. It is designed to accelerate protons up to a maximum energy of 7 TeV to research fundamental particle physics. For other applications such as medical oncology, proton energies of hundreds of MeV are required and hence the accelerator size is typically in metres. These large scale accelerator facilities result in huge financial cost of infrastructure.

A potential solution to the limitation of conventional accelerators is to use plasma itself as a accelerating medium as it is already broken down. Tajima and Dawson [8] proposed an intense laser-plasma accelerator for electrons where it is possible to create electric fields up to hundreds of GV/m using Laser Wake Field Acceleration (LWFA) [9]. The electron plasma wave acts as an accelerating structure for injected electrons and experiments have since demonstrated electron bunches of 4.2 GeV [10] from a centimetre of under-dense gas, with accelerating gradients up to GV/m [9, 11–15].

Using a solid target laser-generated hot electrons can produce a high electrostatic field of the order of $\sim$TV/m, resulting from a charge separation, which can accelerate ions up to tens of MeV/per nucleon. The very first energetic ions produced by a laser interacting with matter were reported by Linlor *et al* [16]. These early experiments produced protons with a maximum energy of 5 MeV using a CO_2 laser delivering pulses with a nanosecond duration [17]. The beams of accelerated ions from these laser systems were found to have a broad energy

spectrum with a sharp high energy cut off.

In the last two decades there has been a renewed interest in laser-driven ion acceleration due to the development of chirped pulse amplification (CPA) [18] in the late 1980s, resulting in the production of ultra-short (picosecond) and high intensity laser pulses, ($> 10^{18}$ Wcm^{-2}) [19]. This increase in intensity resulted in the energy of accelerated protons reaching 58 MeV in 2000 (Snavely *et al* [20]) with laser intensities of $\sim 10^{20}$ Wcm^{-2}. Recently proton energies of 85 MeV have been reported using micron thick, low density targets [21] and intensities of $\sim 10^{21}$ Wcm^{-2}.

Ions accelerated via laser-solid interactions have unique properties such as ultrashort bunch duration (at source) and ultra low emittance [22,23]. Also, due to low costs and compact size, laser accelerated ions are seen as an attractive source for a range of applications, as discussed in the next section.

1.1 Applications of laser-driven ion acceleration

Hadron therapy

One of the most exciting potential applications of laser-driven ion acceleration is hadron therapy. It is viewed as a potential alternative to x-ray radiotherapy to treat cancerous tumours. Ions have a unique energy deposition characteristic, as shown in figure 1.1. They deposit low levels of dose as they travel through tissue and slow down until they reach the end of their path where they deposit the remainder of their energy. This peak at the end of their passage is known as the Bragg peak. By controlling the initial energy of the ions it is possible to accurately control the depth to which they penetrate, targeting the tumour and providing minimal dose to the surrounding healthy tissue. This treatment could also be used for deep seated tumours, which in the past would have been untreatable. For x-rays and electrons on the other hand, the highest dose is

delivered at the surface of the body with the dose deposition decaying quickly with depth within the body. This results in a significant dose being delivered to healthy tissue, and can cause organ damage and growth of secondary tumours.

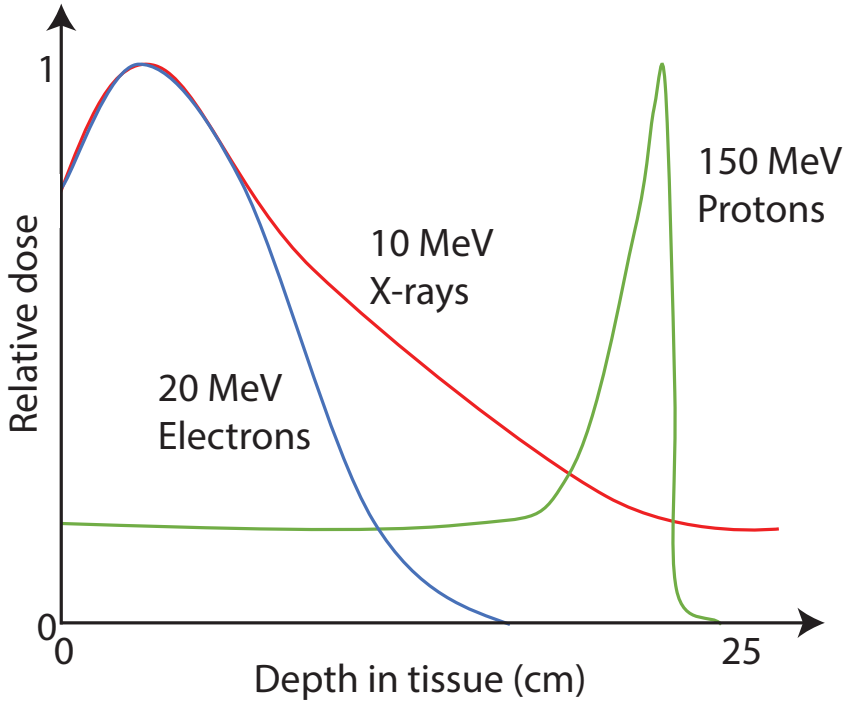

Figure 1.1: Example of dose deposition in tissue for 20 MeV electrons (blue), 10 MeV x-ray beam (red) and a single proton at 150 MeV (green).

A number centres are already performing hadron therapy using conventional accelerator technology, such as cyclotrons and synchrotrons, to provide the ion beam [24, 25]. However, these accelerators require a considerable amount of investment and can cost up to £250 million per centre depending on the type of facility. Due to this high cost, there is a great deal of interest in alternative methods, such as laser-plasma based accelerators, to produce high energy ions. For laser-driven hadron therapy to be feasible, the ion energy must be in the range of 250 MeV to penetrate to deep-seated tumours. Ion beams from laser driven interactions could make the irradiation facility much more compact and less expensive in comparison [26–28]. Another method being proposed is to have the

laser accelerated ion beam injected into a conventional accelerator, thus reducing the size of accelerator needed to boost ions to the required energies [26, 27].

Fast ignition ICF

Fusion is widely considered to be an attractive energy source, due to the fact that it is not carbon-based and unlike fission produces no long-lived waste products. One method of confining a fusion plasma is inertial confinement fusion (ICF), in which a capsule filled with deuterium and tritium (D-T) fuel is compressed to release large quantities of energy through nuclear fusion. In the indirect drive approach [29], the capsule is placed inside a metal cylinder (hohlraum) the inner surface of which are irradiated by lasers. The laser energy is absorbed by the holraum walls converting it into x-rays. These x-rays heat the capsule surface, driving ablation and sending shock-waves into the capsule to compress it. The fuel in the capsule is compressed until it ignites and energy is released during the nuclear burn up of the fuel. However, studies have shown that the compression of the capsule can be sensitive to instabilities, such as the Rayleigh-Taylor instability [1] and symmetry of irradiation, which makes it difficult to achieve uniform compression.

Another approach, proposed by Tabak *et al* [30], is known as the fast ignition approach, which relaxes the compression symmetry requirements. A larger gain can be achieved by applying a final burst of energy to the capsule near the end of compression, rather than using the same laser to drive the entire compression. In this scheme the pellet is compressed by a large number of lasers pulses and a separate high intensity laser pulse is used to deliver energetic particles to the compressed pellet to ignite the fuel. Initially, electrons generated from high intensity laser plasma interactions were proposed and the physics of fast electron generation and transport was widely studied experimentally. However, the electron beams produced in experiments are found to be highly divergent and it is

difficult to couple the hot electron energy to the compressed plasma hot spot due to electron transport effects such as filamentation [31]. This means that the interaction needs to take place close to the hot spot to ensure a sufficient amount of energy is deposited in the correct location. The use of cone-guiding has also been investigated to improve electron energy transport to the compressed fuel [32, 33].

An alternative approach has been proposed using accelerated protons from laser-solid interactions to transport the energy to the compressed fuel [34]. The proton source can be located away from the core but still deposit energy into the hot-spot due to the deposition properties discussed earlier. A thin convex foil can be encased in the cone and energetic ions can be generated when the laser pulse interacts with the foil [32, 35]. The beam of protons can be focussed on the tip of the cone by curving the foil. Using protons instead of electrons avoids the issue of electron transport physics, but requires higher laser drive pulse energy.

Proton radiography

Radiography using ions was first proposed in the late 1960s, where ion beams generated from conventional accelerators were used to probe objects and measure density fluctuations [36, 37]. Protons accelerated from laser-plasma interactions can also be used for imaging applications due to their favourable characteristics and was demonstrated by Borghesi *et al* [38].

As laser-driven protons have an exceptionally good emittance, due to the laminarity of the beam and small source size, they can provide a very high spatial resolution. Also, due to their short pulse length and broad energy spectrum, time resolved measurements can be made due to the time of flight spreading of ions with different energies. Proton probing has become a standard diagnostic for high energy density physics experiments [39, 40]. Faenov *et al* [40] have used proton radiography of a spider's web and demonstrated resolution of structures less than 1 μm in size. This method has also been used to probe the sheath field and ex-

pansion of the rear surface of targets [22]. This was carried out by using a second target and laser pulse, which were perpendicular to the main interaction [22]. The proton beams accelerated from the probe target expands and propagates past the rear surface of the main target. The strong electric and magnetic fields generated by the main interaction will cause deflections of the probe protons, which results in a modification of the spatial-intensity profile of the beam. These laser-driven proton beams have been implemented to probe plasmas in order to make temporal and spatial measurements of the electric and magnetic fields [41–44], plasma channel formation [45] and the propagation of collisionless shocks [46].

Additionally, there are a number of other applications of laser-driven ions including proton heating [47–50], radioisotope production, [51–55] and neutron production [56]. A recent review paper by Schreiber *et al* [57], provides a detailed outline of source development and potential application from laser-driven ion acceleration.

1.2 Challenges for laser-accelerated ions

Laser-accelerated ions have a great deal of potential for a number of different applications. However, each application requires different ion beam characteristics. The beam parameters required for each of the applications discussed so far are listed in 1.1.

Application	Key parameters
Hadron therapy	E_p upto 250 MeV, high rep. rate, energy spread $< 1\%$
Fast ignition	E_p 5-15 MeV, $>10\%$ efficiency, energy spread $< 20\%$
Radiography	High flux, broadband, low emittance, $E_p > 1$ MeV

Table 1.1: Proton beam requirements for three example applications [5].

The production of proton beams from micron-thick targets have been studied extensively over the past decade and have ideal properties for applications such as radiography [42]. It could potentially be used in-conjunction with conventional accelerators by injecting ions into a cyclotron, boosting ion energies required for hadron therapy [28]. However, the quality of these beams would need to be improved with current laser technology such as increasing the intensity for maximising the ion energy [5]. A number of studies have been carried out to control the energy spectral width of the sheath accelerated beams but none have been successful so far in creating an energy spread less than 1%.

A number of different acceleration mechanisms have been proposed, which will be discussed in-depth in chapter 3, and investigated which promise improved energy scaling with laser intensity, higher ion energies, monoenergetic beams and higher (laser to ion energy) conversion efficiency. One of the proposals is the radiation pressure acceleration (discussed in chapter 3) scheme where high intensity lasers can be used to accelerate ions from an ultra-thin target [58–60] or push a compressed layer of electrons, from the front surface, through a target [61,62] giving high quality beams, where the ion energy in this regime scales with intensity.

1.3 Thesis outline

The presented PhD work was intended to develop and explore advance approaches of high intensity laser-driven ion acceleration using ultra-thin nanometre foils. New pathways are crucial to push the current limits of laser-generated ion beams towards parameters necessary for potential applications. In light of this, proton acceleration from the Vulcan petawatt laser system was investigated, namely the spatial-intensity profile of the beam and the effects the laser pulse rising edge, in the picosecond range, has on ion energies. This work was conducted as part of the

Advance Strategies for Accelerating Ions with Lasers (A-SAIL) project involving several institutions throughout the UK.

This thesis begins with an introduction to the relevant fundamental physics of laser-matter interactions in chapter 2. Chapter 3 presents a more detailed discussion of laser-driven ion acceleration and the different mechanisms, as well as a review of previous work and ongoing research in the field. A discussion of the experimental methods, such as laser systems and diagnostics employed, and a description of the PIC code used to carry out simulations to investigate the underlying physics is presented in chapter 4.

Chapter 5 presents experimental results of laser-driven ion acceleration from ultra-thin foils, carried out using the Vulcan petawatt laser system. Here the spatial-intensity profile of the proton beam is investigated to diagnose intra-pulse transition between different acceleration mechanisms. Chapter 6 presents an experimental investigation of the effects of the pulse rising edge intensity profile on the picosecond range on laser-driven proton acceleration. In the final chapter, results from chapters 5 and 6 are summarised and potential future work is discussed.

Chapter 2

Fundamentals of laser-plasma interactions

This chapter gives a brief introduction to fundamental laser-plasma interaction physics.

When an ultra-intense laser pulse interacts with a solid target, it ionises the front surface of the target liberating electrons which are then accelerated to relativistic velocities in the laser field. The mechanisms and the fundamental principles of a single electron moving in a laser field, and propagation of a laser pulse within a plasma are discussed. Whilst there are many aspects of laser-plasma interactions, only the fundamentals and the most important in the context of this thesis will be introduced in this chapter. These concepts are discussed in far greater detail in existing literature, such as books by P. Gibbon [1], W. L. Kruer [63] and A. Macchi [64].

2.1 Fundamental principles

To understand the underlying interaction between a laser pulse and a solid, the sensible place to start is with Maxwell's equations of electromagnetism, equations 2.1 - 2.4. These equations can be used to describe the propagation of light as an electromagnetic wave and the relationship between the electric and magnetic fields of the laser pulse.

$$\nabla \cdot \boldsymbol{E} = \frac{\rho}{\varepsilon_o} \tag{2.1}$$

$$\nabla \cdot \boldsymbol{B} = 0 \tag{2.2}$$

$$\nabla \times \boldsymbol{E} = -\frac{\partial \boldsymbol{B}}{\partial t} \tag{2.3}$$

$$\nabla \times \boldsymbol{B} = \mu_o \boldsymbol{J} + \frac{1}{c^2}\frac{\partial \boldsymbol{E}}{\partial t} \tag{2.4}$$

where c, ε_o and μ_o terms are the physical constants for the speed of light in vacuum, and the permittivity and permeability of free space, respectively. Also, it should be noted that $c = \sqrt{1/\varepsilon_o \mu_o}$. $\boldsymbol{E}$ and $\boldsymbol{B}$ represent the electric and magnetic fields, and ρ and $\boldsymbol{J}$ are charge and current densities respectively.

In vacuum the laser pulse is free from charge, $\rho = 0$ and $\boldsymbol{J} = 0$, therefore equations (2.1) and (2.4) can be simplified to:

$$\nabla \cdot \boldsymbol{E} = 0 \tag{2.5}$$

$$\nabla \times \boldsymbol{B} = \frac{1}{c^2}\frac{\partial \boldsymbol{E}}{\partial t} \tag{2.6}$$

Using the vector identity $\nabla \times (\nabla \times \boldsymbol{A}) = \nabla(\nabla \cdot \boldsymbol{A}) - \nabla^2 \boldsymbol{A}$, it is possible to derive a single differential equation to describe the propagation of light. Substituting Faraday's law (equation 2.3) and the simplified Gauss' law for an electric field in a vacuum (equation 2.5) into the vector identity gives:

$$\nabla \times (\nabla \times \boldsymbol{E}) = \nabla \times (-\frac{\partial \boldsymbol{B}}{\partial t}) = \nabla(\nabla \cdot \boldsymbol{E}) - \nabla^2 \boldsymbol{E} \tag{2.7}$$

Since the laser pulse is considered to be in vacuum the $\nabla(\nabla \cdot \boldsymbol{E})$ term is eliminated by equation 2.5 leading to the wave equation:

$$\nabla^2 \boldsymbol{E} = \frac{1}{c^2} \frac{\partial^2 \boldsymbol{E}}{\partial t^2} \tag{2.8}$$

A general solution of the wave equation is:

$$\boldsymbol{E} = \hat{e}_x E_o \sin(\omega_L t - k_L z) \tag{2.9}$$

where E_o is the laser electric field amplitude and in this case points along the x-axis. The laser pulse wave vector and angular frequency are described by k_L and ω_L respectively, with the pulse propagating along the z-axis. Substituting equation 2.9 into the wave equation (equation 2.8) the dispersion relation in vacuum can be found:

$$\omega_L^2 = k_L^2 c^2 \tag{2.10}$$

To obtain the relationship between the electric and magnetic fields the plane wave equation, equation 2.9, can be substituted into Faraday's Law, equation 2.3, and evaluated to yield:

$$\boldsymbol{B} = \frac{1}{c} \hat{e}_y E_o \sin(\omega_L t - k_L z) \tag{2.11}$$

Comparing equation (2.9) and equation (2.11) gives a simple relationship be-

tween the electric and magnetic fields to show that they are orthogonal:

$$|\mathbf{B}| = \frac{1}{c}|\mathbf{E}| \tag{2.12}$$

Thus, the k vector, $\mathbf{E}$ and $\mathbf{B}$ fields of the plane wave are perpendicular to each other as shown schematically in the diagram below.

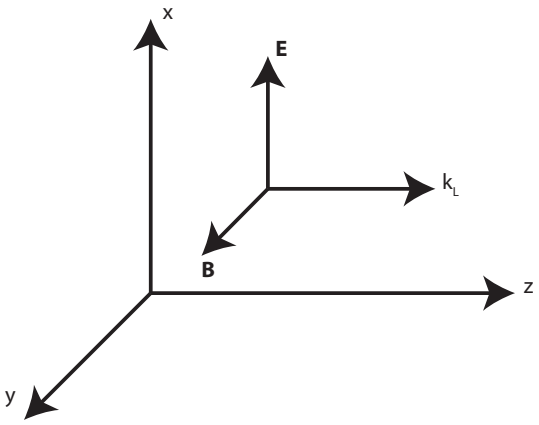

Figure 2.1: k_L, $\mathbf{E}$ and $\mathbf{B}$ of the plane wave are mutual perpendicular to each other, and $\mathbf{E}$ and $\mathbf{B}$ are in phase

The intensity of the laser pulse can be found to equal the flow rate of electromagnetic energy per unit area, the Poynting vector. Taking the time average over the fast oscillations of the laser field, the intensity is:

$$I = \left\langle \left| \mathbf{E} \times \frac{\mathbf{B}}{\mu_o} \right| \right\rangle = \frac{\varepsilon_o c}{2} E_o^2 \tag{2.13}$$

2.2 Single electron in an intense laser field

As ions are too heavy to be directly accelerated by current laser systems, their acceleration occurs due to a charge separation electrostatic field generated when the laser field displaces the electrons. It is therefore important to understand the mechanisms by which electrons are accelerated to explore ion acceleration.

It begins by understanding the motion of a single electron in a electromagnetic wave.

A free electron in the presence of an electromagnetic wave will oscillate due to the Lorentz force driven by the electric and magnetic fields. The Lorentz force is defined as:

$$\mathbf{F}_L = \frac{d\boldsymbol{p}_e}{dt} = -q(\mathbf{E} + \boldsymbol{v}_e \times \mathbf{B}) \tag{2.14}$$

where $\boldsymbol{p}_e = \gamma m_e \boldsymbol{v}_e$ is the electron momentum, m_e and $\boldsymbol{v}_e$ is the electron mass and velocity respectively and $\gamma = \sqrt{1 + (\boldsymbol{p}_e/mc)^2} = 1/\sqrt{1 - (\boldsymbol{v}_e/c)^2}$ is the Lorentz factor. The electric and magnetic field amplitude can be related by equation 2.12, $|\mathbf{B}| = \frac{1}{c}|\mathbf{E}|$ (using Faraday's law, equation 2.3).

The velocity of the electron can be described in two cases depending on the laser intensity. For low intensities the electron motion is non-relativistic ($\boldsymbol{v}_e << c$), as the electron motion is dominated by the electric field ($q\mathbf{E}$) and therefore the electron oscillates only along the laser polarisation direction. The contribution to motion from the magnetic field can be considered to be negligible.

$$\boldsymbol{v}_e = \frac{eE_o}{m_e\omega_L}\sin(\omega_L t - k_L z) \tag{2.15}$$

However, as the electron approaches the speed of light ($\boldsymbol{v}_e \sim c$) the magnetic component ($q\boldsymbol{v}_e \times \mathbf{B}$) must also be considered causing the electron to be pushed along the laser propagation axis with velocity.

$$\boldsymbol{v}_e = \frac{e^2E_o^2}{4m_e^2\omega_L^2}\cos(2\omega_L t - k_L z) \tag{2.16}$$

It should be noted that in the relativistic case, the electron oscillates at twice the laser frequency compared to the non-relativistic case. The importance of the relativistic effects when the electron oscillates close to the speed of light can be simplified to the dimensionless light amplitude, a_o:

$$a_o = \frac{eE_o}{m_e \omega_L c} = 0.85\sqrt{I_L \lambda_L^2} \tag{2.17}$$

where I_L is in units of $\sim 10^{18}$ Wcm^{-2} and λ_L is in μm. Two regimes can be defined with $a_o < 1$ corresponding to the non-relativistic regime and $a_o > 1$ when the electron oscillation becomes relativistic.

2.3 Ponderomotive force

The previous section discussed electrons in an infinite laser field, where they do not gain energy as they return to their equilibrium position at the end of each oscillation cycle. This is known as the Lawson-Woodward theorem and is used to provide insight into how electron motion changes as relativistic effects become important. However, a more realistic situation is discussed here where the laser pulse is tightly focused and has a Gaussian profile, spatially and temporally. The electron oscillates in the laser field, but every half cycle it is pushed out towards a region of lower intensity. During the return cycle the electron experiences a weaker restoring force resulting in the electron not returning to it original position, as illustrated in figure 2.2. When averaged over many oscillations, this results in electrons being pushed from regions of high intensity to regions of lower intensity resulting in a net energy gain. This effect is created by the ponderomotive force.

For the non-relativistic case, the ponderomotive force is defined as:

$$\mathbf{F}_p = -\frac{e^2}{4 m_e \omega_L^2} \nabla \mathbf{E}^2 \tag{2.18}$$

In the non-relativistic regime the electrons experience the force along the electric field. At relativistic intensities the electrons experience a drift motion in the transverse direction. The relativistic ponderomotive force is found to be:

$$\mathbf{F}_p = -m_e c^2 \nabla \sqrt{1 + a_o^2/2} = -m_e c^2 \nabla \gamma \tag{2.19}$$

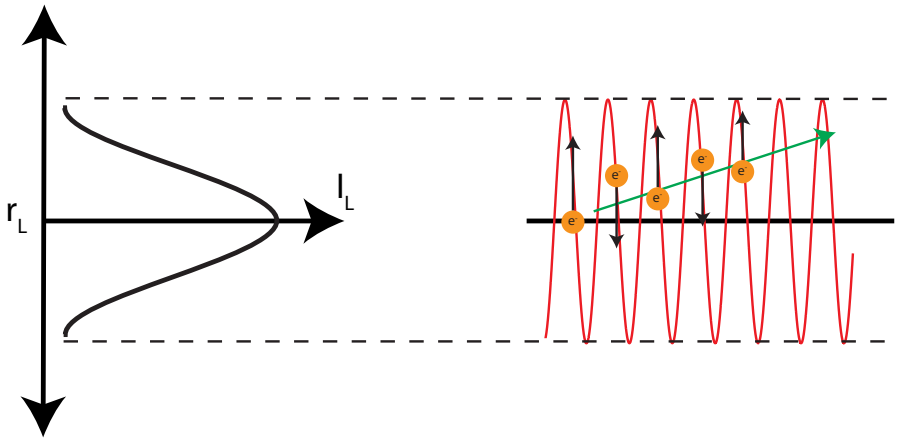

Figure 2.2: Illustration of the radial intensity profile of the laser pulse and a single electron drift due the resulting ponderomotive force [1].

The electron kinetic energy gained over the laser cycle can be expressed as the ponderomotive potential [65].

$$U_p = m_e c^2 (\gamma - 1) \tag{2.20}$$

Using the ponderomotive potential, the angle at which electrons are ejected from the laser axis in the relativistic regime can be found. Momentum is transferred from multiple photons to the electron oscillating in the laser fields. Using conservation of parallel momentum, the momentum gained by electron from photons and can be expressed as:

$$p_\parallel = n\hbar k = \frac{n\hbar\omega_L}{c} = \frac{U_p}{c} = m_e c(\gamma - 1) \tag{2.21}$$

The relationship between $p_\parallel$ and $p_\perp$ is:

$$p_\parallel = \frac{p_\perp^2}{2m_e c} \tag{2.22}$$

thus giving the emission angle:

$$tan\,\theta = \frac{p_{\perp}}{p_{\parallel}} \tag{2.23}$$

or equivalently:

$$cos\,\theta = \sqrt{\frac{\gamma - 1}{\gamma + 1}} \tag{2.24}$$

It is clear that there is a relationship between the ejection angle and the electron energy as shown in figure 2.3. As the laser pulse becomes relativistic, γ increases and causes the ejection angle to decrease (equation 2.24), which causes the ejected electrons to propagate along the laser axis.

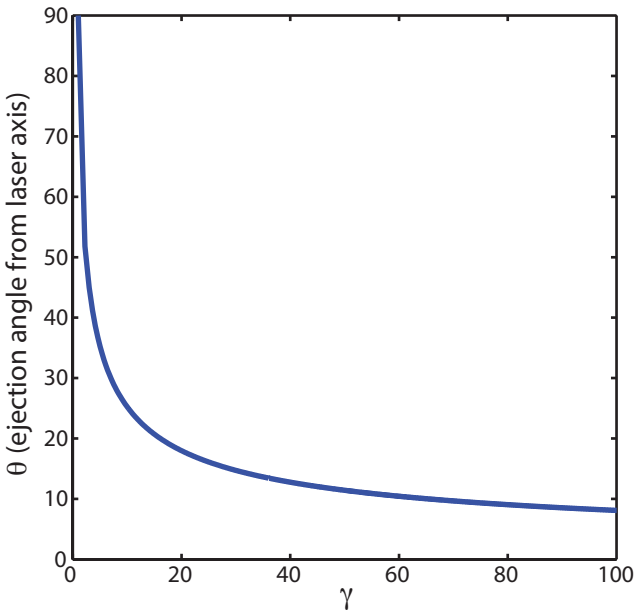

Figure 2.3: Emission angle of an electron interacting with a laser pulse. The emission angle becomes closer to the laser axis as the γ factor increases.

2.4 Laser induced ionisation

Now that the motion of a single electron in a laser field has been discussed, the next step is to look at the laser interaction with matter and how a plasma is created. Initially the laser pulse ablated the target at low intensity and as the intensity increases the ionisation process occurs. A process by which a solid target is turned into a plasma. This process is not the main interest of this study, but it is important to understand the initial steps that take place. This interaction takes places when the amplified spontaneous emission (ASE) which precedes the main laser pulse on the order of a few nanoseconds, comes into contact with the solid target.

An estimate of the laser intensities required for ionisation is obtained by calculating the electric field strength that binds an electron to its atom. For example, at the Bohr radius, a_B, the electric field strength of an electron bound to a hydrogen atom, is given by

$$E_a = \frac{e}{4\pi\epsilon_o a_B^2} \approx 5.1 \times 10^9 \text{ V/m} \tag{2.25}$$

$$a_B = \frac{4\pi\epsilon_o \hbar^2}{m_e e^2} \approx 5.3 \times 10^{-11} \text{ m} \tag{2.26}$$

where ϵ_o is the permittivity of free space and $\hbar$ is the reduced Planck's constant. Now we can equate the binding electric field with the laser intensity required to ionise the hydrogen atom.

$$I_a = \frac{\epsilon_o c E_a^2}{2} \approx 3.51 \times 10^{16} \text{ W/cm}^2 \tag{2.27}$$

Above this intensity the target material will begin to ionise and form a plasma solely by the laser's electric field.

Multi-photon ionisation

In the case where the energy of a single photon is smaller than the ionisation potential of the bound state, an electron can still gain enough energy to overcome the potential barrier of the nucleus by absorbing several low energy photons in a short time. This process is known as multi-photon ionisation. As more electrons are stripped from the nucleus, it becomes more difficult to strip successive electrons. The ionisation rate for n-th electron, Γ_n, is defined as:

$$\Gamma_n = \sigma_n I_L^n \tag{2.28}$$

where σ_n is the cross section of this process, which decreases with the number of photons required for ionisation, n. However, the ionisation rate increases with I_L, ensuring ionisation will occur at sufficiently high intensities.

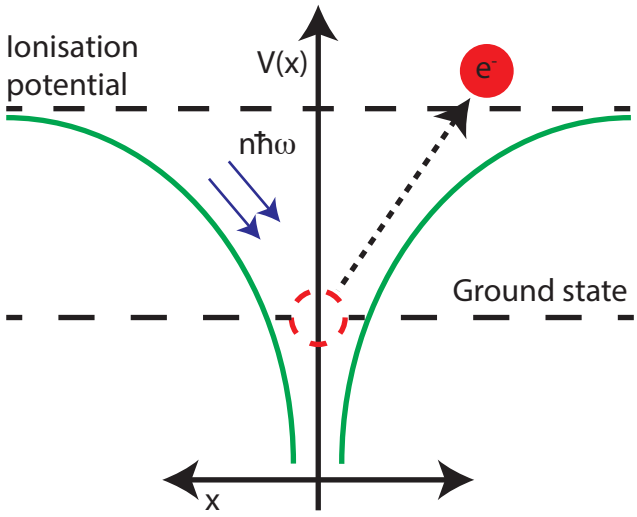

Figure 2.4: Illustration of the multiphoton ionisation process.

If the energy of the photon is low then the electron will require a number of photons with a total energy exceeding the ionisation potential to escape the atom. The kinetic energy of the freed electron can be calculated by

$$E_f = (n+s)\hbar\omega_L - E_{ion} \tag{2.29}$$

where s is the excess number of photons absorbed and E_{ion} is the ionisation potential. It would require ≈ 12 photons to ionise the hydrogen atom using a laser with 1.054 μm wavelength.

This mechanism occurs during the very early interaction between the laser pulse and matter. As the intensity increases and the main pulse comes into contact with the target, other mechanisms become important and begin to dominate the ionisation process.

Tunnel and barrier suppression ionisation

Laser-driven ion acceleration schemes utilise a laser intensity that greatly exceeds the threshold for hydrogen ionisation described in equation (2.27). The laser fields superposition on the coulombic field between the electrons and nucleus causes the Coulomb barrier to be suppressed. Thus ionisation can occur by escape of the electron wavepacket over the barrier. There is also a finite probability of ionisation occurring by the wavepacket tunnelling through the suppressed barrier as shown in figure 2.5.

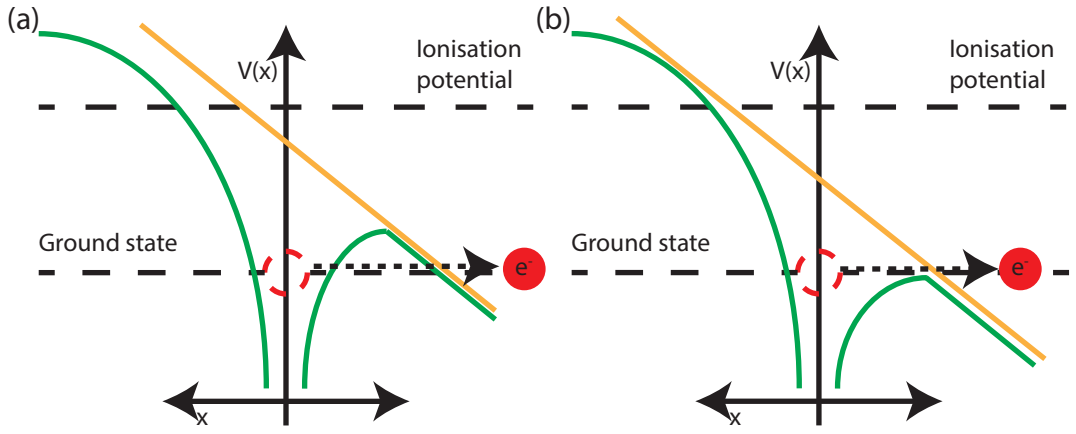

Figure 2.5: Schematic of barrier suppression ionisation. The electron can escape the potential well of the atom by (a) is barrier suppression leading to tunnelling ionisation, (b) is barrier suppression leading to over-the-barrier ionisation.

The dominant ionisation mechanism (multiphoton or over the barrier) in a given interaction is determined by the Keldysh parameter [66]:

$$K = \omega_L \sqrt{\frac{2E_{ion}}{I_L}} \tag{2.30}$$

When $K > 1$ multi-photon ionisation dominates. However if $K < 1$ then the process is dominated by tunnelling and barrier suppression ionisation.

2.5 Plasma

In 1859 Sir William Crookes identified a new state of matter whilst studying discharges in Crookes tubes. However it was first called a "plasma" in 1928 by Irving Langmuir. A formal description is given by Francis Chen [67]:

"A plasma is a quasi-neutral gas of charged and neutral particles which exhibits collective behaviour."

This definition describes the plasma as being charge neutral on a macroscopic scale where the number of positive and negatively charge particles are approximately the same. *"Collective behaviour"* means that the motion of particles are not only dependant on local conditions, but are also driven by long range electromagnetic forces. As charges move around in a plasma, electric fields are generated which drive currents and creates magnetic fields.

To technically define a plasma a number of criteria also have to be satisfied [67]:

• The dimension of the system must be much larger than the shielding distance (The distance at which the local electric field can influence the particles).

• Many particles must exist within the shielding distance. The shielding is only valid if there are enough particles contained within the plasma.

• The collision rate must be small compared to the characteristic plasma oscillation frequency.

Debye length

Since ions have a lower charge to mass ratio they are considered to be immobile compared to the electrons inside the plasma, on the time-scale of the interaction with a short laser pulse. Displacement of electrons creates a positively charged background. The electrons will react to the potential of the ion, limiting the separation and thus the distance the field acts over within the plasma. This shielding distance is an important parameter for characterising a plasma and is known as the Debye length, λ_D, and is given by:

$$\lambda_D = \sqrt{\frac{\varepsilon_o k_B T_e}{e^2 n_e}} \tag{2.31}$$

where k_B is the Boltzmann constant, T_e is the electron temperature and n_e is the electron density. The Debye length is used to determine the distance at which an ion's electric field is sufficiently shielded so that it will not have any effect on the surrounding plasma particles.

Plasma frequency

Another key parameter is the frequency at which the electrons oscillate about the ion background. If an electron is displaced from its rest position, an electric field is created that will act to reverse the electron's motion and pull it back to its original position. The electrons will usually overshoot their original position, resulting in an oscillation around the rest position with a characteristic frequency known as the plasma frequency, ω_p, given by:

$$\omega_p = \sqrt{\frac{n_e e^2}{\gamma m_e \epsilon_o}} \tag{2.32}$$

We can also define the ion plasma frequency, ω_{pi} in a similar way if we replace n_e and m_e with the ion density, n_i and ion mass m_i in equation 2.32.

2.6 Laser interaction with the front surface of a solid

As discussed earlier, the initial interaction of the laser pulse ionises the front surface of the target. This results in the generation of front surface plasma which expands into the surrounding vacuum. This expanding plasma plays a significant role in the transfer of laser energy to the electrons, and will be discussed later in this chapter. The distance over which the plasma expands during the laser-plasma interaction is the plasma density scale length, L, and can be estimated as:

$$L \simeq c_o \tau_L \tag{2.33}$$

where τ_L is the laser pulse duration and c_o is the ion speed of sound, which can be expressed as:

$$c_o = \sqrt{\frac{k_B(ZT_e + T_i)}{m_i}} \tag{2.34}$$

where Z is the ionisation state, T_e is the plasma electron temperature, T_i is the plasma ion temperature and m_i is the ion mass. As the front surface plasma expands outwards, the initial step-like density of the cold target changes to create a density profile which exponentially decays with the plasma density scale length:

$$n_e(z) = n_0 \exp\left(-\frac{z}{L}\right) \tag{2.35}$$

z is the distance from the target front surface to the expansion front and n_0 is the initial electron density of the target. The scale length can be characterised as the distance over which the electron density falls to $1/e_N$ ($e_N = 2.718$) of the initial value.

Laser propagation in a plasma

In the previous section the motion of electrons in a infinite plane wave is discussed, as well as in a temporally and spatially inhomogeneous laser field. Now the propagation of the laser pulse in a plasma, containing a large number of ions and electrons, is considered. In section 2.4, the initial laser-solid interaction process was discussed, but no comment was made regarding the laser propagation inside the plasma, formed by ionisation at the front surface.

When an electron is displaced from the ion background an electrostatic restoring force, F_e, given by:

$$F_e = m_e \frac{d^2\mathbf{r}}{dt^2} = -q\mathbf{E} \tag{2.36}$$

where $\mathbf{r}$ is the displacement vector. In a quasi-neutral medium it can be assumed that the charge is $\rho \approx 0$ and recalling Faraday's law equation 2.3 and Amperes law equation 2.4 the wave equation for a plasma is defined by:

$$\nabla^2 \boldsymbol{E} = \frac{1}{c^2}\frac{\partial^2 \boldsymbol{E}}{\partial t^2} + \mu_0 \frac{\partial \mathbf{J}}{\partial t} \tag{2.37}$$

Substituting for $\mathbf{J} = -en_e\frac{d\mathbf{r}}{dt}$, the current density and the simple plane wave solution, equation 2.9 into the plasma wave equation, the plasma dispersion relation is defined as:

$$\omega_L^2 = k^2c^2 + \omega_p^2 \tag{2.38}$$

Hence,

$$k = \frac{\omega_p}{c}\left(\frac{\omega_L^2}{\omega_p^2} - 1\right)^{\frac{1}{2}} \tag{2.39}$$

When $\omega_L = \omega_p$ equation 2.39 tends to zero and the laser does not propagate in the plasma and is reflected. From this condition a density can be defined above

which the wave vector becomes imaginary. This is the critical density, n_{crit}, and is defined as:

$$n_{crit} = \frac{m_e \epsilon_o \omega_L^2}{e^2} \tag{2.40}$$

It can also be given in practical units as:

$$n_{crit} = \frac{1.11 \times 10^{21}}{\lambda_L^2[\mu\text{m}]}[\text{cm}^{-3}] \tag{2.41}$$

where λ_L is the laser wavelength. When $n_e > n_{crit}$ the laser will not propagate into the plasma. This regime is known as overdense. When $n_e < n_{crit}$ the laser will propagate through the plasma and interact with the electrons. This is known as the underdense regime. In this thesis, we initially deal with solid density targets and therefore the interaction is in the overdense regime. For a 1.054 μm pulse (the Vulcan Petawatt system) the critical density is 1×10^{21} cm^{-3}. For example, an aluminium target has an electron density of $\approx 800 n_{crit}$. Equations 2.40 and 2.41 are valid for non-relativistic laser intensities.

When the laser intensity is high, the electron quiver velocity becomes relativistic. The critical density equation must take into account the relativistic increase of the electron mass and thus becomes:

$$n_{crit}^{'} = \gamma n_{crit} = \frac{\gamma m_e \epsilon_o \omega_L^2}{e^2} \tag{2.42}$$

The presence of the Lorentz factor,γ, acts to increase the mass of electrons as they oscillate in the laser field at relativistic velocities. The relativistic critical density is higher than the non-relativistic critical density, allowing the laser pulse to propagate through targets which are classically overdense. This is known as relativistic induced transparency [68].

The laser field is able to penetrate beyond the relativistically corrected critical density surface as the evanescent electric field is defined as:

$$E_L(z) = E_L(z_e)exp(-\frac{z}{l_s}) \tag{2.43}$$

where z_e is the position of the critical surface and l_s is the skin depth, which is generated beyond the critical surface by the laser field. l_s is defined as:

$$l_s = \frac{c}{\sqrt{\omega_p^2 - \omega_l^2}} \tag{2.44}$$

For a solid target with $n_e \gg n_{crit}$, $l_s \simeq c/\omega_p$.

Laser self-focusing

The plasma refractive index, n_r is a function of the plasma frequency ω_p and the laser frequency ω_L, as follows:

$$n_r = \sqrt{1 - \left(\frac{\omega_p^2}{\gamma\omega_L^2}\right)} \tag{2.45}$$

It can also be written in terms of the plasma density, n_e, and the critical density, n_{crit}, as:

$$n_r = \sqrt{1 - \left(\frac{n_e}{\gamma n_{crit}}\right)} \tag{2.46}$$

As the laser pulse propagates through the plasma, the electrons experiencing high intensities will be expelled to region of lower intensities due to the ponderomotive force. With respect to the propagation axis of the laser pulse, the electrons will be pushed radially outwards, resulting in a radial density gradient where the lowest density corresponds to the region of the highest laser intensity. This will consequently result in a refractive index profile with a maximum corresponding to the laser axis, as shown in Fig. 2.6. This radial variation in refractive index results in ponderomotive self focusing.

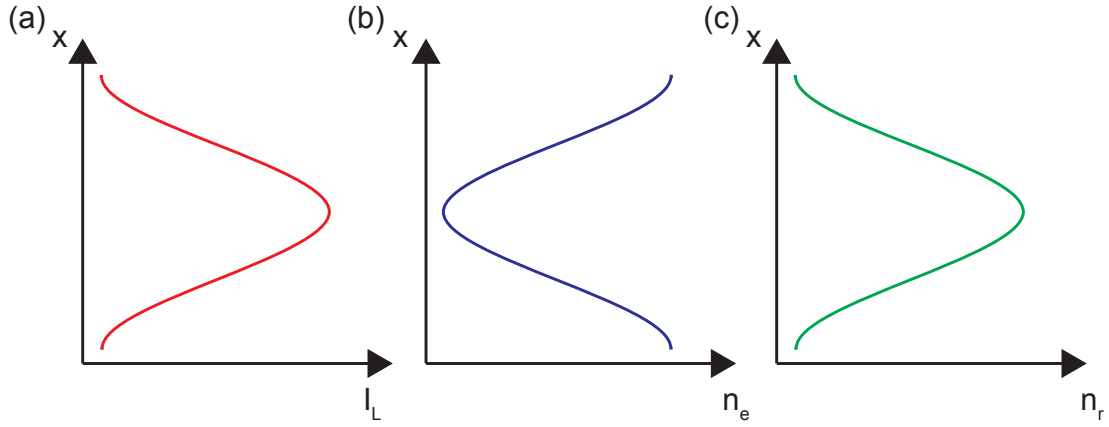

Figure 2.6: (a) Intensity variation of the laser pulse (b) radial plasma electron density profile (c) radial refractive index profile

At relativistic intensities, the velocity of the electrons in the oscillating electric field of the laser pulse tends to the speed of light and the relativistic increase in the electron mass must be taken into account. Since the frequency of plasma electrons scales with the electron density and the inverse of electron mass as discussed earlier, if the mass of the electrons was to increase this will result in a decrease of the electron frequency and increase in the refractive index of the plasma.

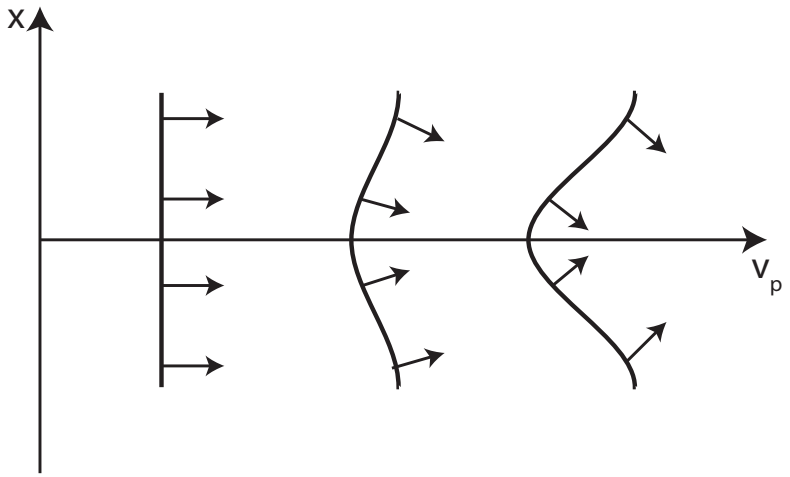

Figure 2.7: Illustration of realtivistic self-focusing due to increase in the on-axis refractive index resulting in the phase velocity of the laser becoming slower on-axis

Therefore, relativistic self-focusing can also occur due to an increase in the on-axis refractive index caused by a reduction in plasma frequency when electron motion becomes relativistic. Self-focusing is caused by the phase velocity of the laser becoming slower on-axis, causing the laser wavefront to bend, as shown in figure 2.7.

Relativistic induced transparency

As discussed earlier the laser pulse can only propagate up to the critical density of a plasma. At this point the pulse is either reflected or absorbed, see section 2.7.

Initially when the laser pulse irradiates the front surface of tens of nanometer thick foil, it heats and displaces the electrons at the front surface. As the pulse accelerates the electrons, they reach relativistic velocities causing an increase in their mass due to the Lorentz factor, γ. At the critical surface there is a interplay between the electron density and the critical density. The electron mass is increased by the Lorentz factor and as the electrons are accelerated the electron density decreases. The critical density is increased by the Lorentz factor. As discussed in the previous section the corrected refractive index depends on the ratio between the electron density and the critical density ($n_e/\gamma n_{crit}$), resulting in the refractive index being reduced. This enables the laser pulse to propagate further into the target. Also the skin depth (equation 2.44), at which the laser field decays evanescently beyond the critical surface, increases because the plasma frequency is reduced by the Lorentz factor. When this relativistically corrected skin depth is comparable or greater than the target thickness, the laser pulse will be transmitted.

At peak intensities achievable with current state-of-the-art laser technology, some degree of target expansion is required for RIT to occur. The reduction in the n_e, together with the relativistic increase in the critical density, results in the

criteria ($n_c/n'_{crit} < 1$) for relativistic self-induced transparency being met. The onset of relativistic self-induced induced transparency has been investigated in detail with ultra-fast temporal resolution by Palaniyappan *et al* [69–71].

To achieve relativistic induced transparency at solid density higher intensity lasers are required. For example, for fully ionised aluminium, a Lorentz factor of γ =780 would be required and thus $a_o \approx 1100$ or $I_L \approx 10^{24}$ W/cm^2.

2.7 Absorption

A Significant topic of importance in laser-solid experiments is how the energy of the laser pulse is absorbed in the overdense target. The incident laser pulse can only propagate up to the critical density. The energy transfer from the laser to the electrons, and subsequently to the ions, depends upon a number of different parameters such as; laser intensity, polarisation and angle of incidence. Collisional and collisionless absorption processes occur. At the intensities discussed in this thesis, $\sim 10^{20}$ W/cm^2, the electron motion is in the relativistic regime. At this intensity where the electron motion is relativistic and the mean free path of the electrons is large, collisionless absorption processes, tend to dominate.

Inverse bremsstrahlung

When a electron collides with another charged particle it de-accelerated and emits radiation, this is know as bremsstrahlung radiation. Inverse bremsstrahlung is the opposite phenomenon where the electron is accelerated by the laser electric field resulting in a transfer of energy from the photons to the electrons. Typically, the electron will not gain energy as it will experience an equal and opposite acceleration in the oscillating field of the laser pulse. However, if the electron collides with an ion during the oscillation, energy will be transferred from the electron to the ion, resulting in a net loss of energy by the laser through collision.

This mechanism typical dominates at intensities $< 10^{14}$ Wcm^{-2} [1].

Resonance absorption

At laser intensities in the range of $10^{14} - 10^{17}$ Wcm^{-2} and the front surface of the target has a plasma scale length is greater than the laser wavelength, resonance absorption mechanism dominants the absorption process. Also, it requires a linearly polarised laser pulse with its electric field perpendicular to the target density gradient interacts with a target at an oblique incidence (θ_L) [1]. At higher intensities resonance absorption is still present but is no longer dominates the absorption process.

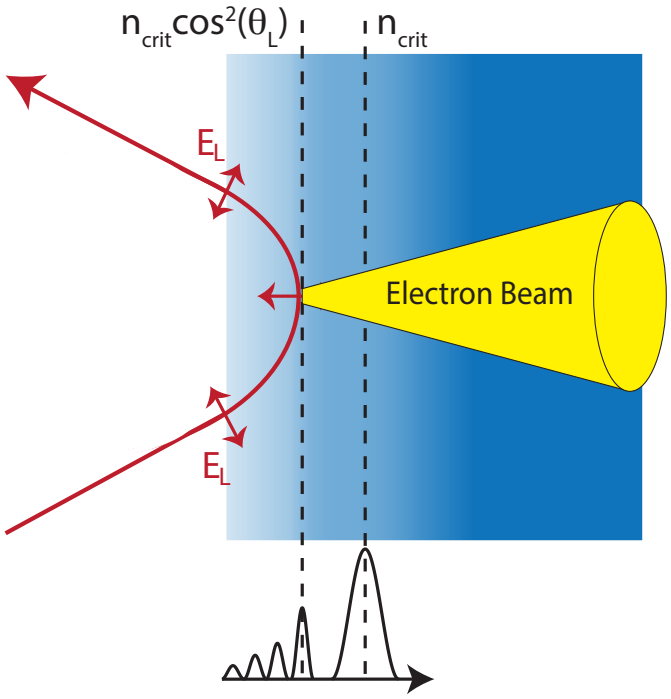

Figure 2.8: Schematic of resonant absorption. The p-polarised laser pulse injects electrons into the target at the reflected point of the laser pulse.

The laser pulse propagates through the expanding plasma where it is constantly refracted by the increasing electron density. At $n_{crit}\cos^2(\theta_L)$, due to refraction then laser pulse is reflected and its electric field oscillates normal to the critical

surface. This is explained by considering the dispersion relation shown in equation 2.38 but modifying the laser k-vector transverse to the density gradient to include the incidence angle which becomes $k_y = (\omega_L/c)sin^2\theta$. The dispersion relation can be rearranged to give:

$$\omega_L^2 = \omega_p^2 + \omega_L^2 \sin^2\theta \tag{2.47}$$

The electric field component normal to the target surface can tunnel through beyond $n_{crit}\cos^2(\theta_L)$, as it decays evanescently, to resonantly drive a plasma wave at the laser frequency at the critical surface. The resulting plasma wave can then transfer its energy to the plasma via wave breaking or damping effects.

Vacuum absorption

A similar mechanism, known as vacuum heating, begins to dominate the absorption process [72], when the plasma scale length is much less than the laser wavelength. Absorption takes place when the laser pulse cannot penetrate past $n_{crit}\cos^2(\theta_L)$ [1]. The electrons oscillate in the electric field of the laser but due to the sharp transition from solid to vacuum plasma waves cannot be excited. Instead the electrons are pulled from the solid target into vacuum by the first half period of the electric field and then accelerated back into the overdense plasma by the second half period. When the electrons pass beyond the $n_{crit}\cos^2(\theta_L)$, the electric field has a weaker influence as it is only able to penetrate a skin depth beyond the critical surface. This results in a net energy gain for the electron as the restoring force of the laser on the electrons is weaker. This injects a population of fast electrons into the target.

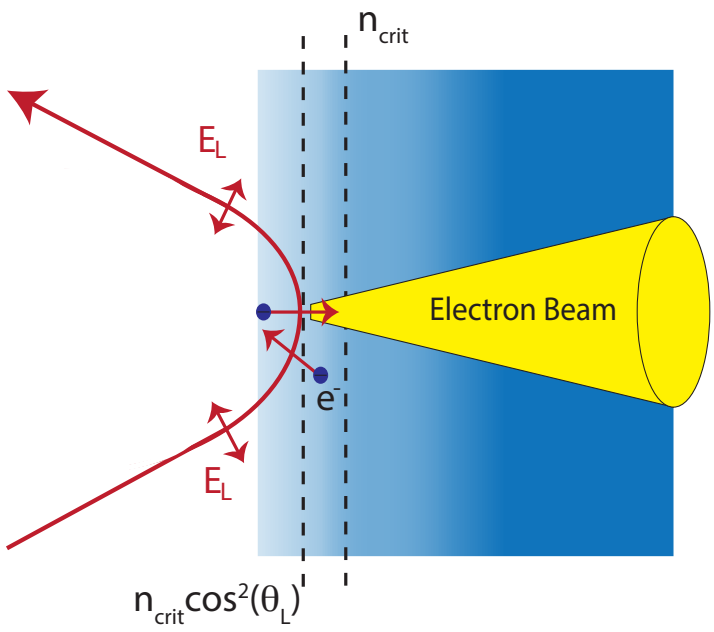

Figure 2.9: Schematic of vacuum heating where the electric field of the laser pulse pulls electrons from the solid target and accelerated them back into the target.

j x B absorption

Another mechanism by which electrons are accelerated by the laser fields is $\mathbf{j} \times \mathbf{B}$ heating. It is the dominant mechanism at relativistic intensities ($\geq 10^{18}$ W/cm^2), where the velocity of the electrons is close to the speed of light and the magnitude of the $v \times \mathbf{B}$ component of the Lorentz force (equation 2.14) becomes comparable to the electric field component. This mechanism was first proposed by Kruer and Estabrook in 1985 [73]. The electron motion due to the $v \times \mathbf{B}$ component is directed along the propagation direction of the laser and thus the electrons are injected at twice the laser frequency which can be expressed by:

$$\mathbf{F} = \frac{-m_e}{4} \frac{\partial v_{osc}^2(x)}{\partial x} (1 - \cos(2\omega_L t)) \tag{2.48}$$

where v_{osc} is the electron quiver velocity. The first term acts to ponderomotively drive electrons away from region of high intensity and the second term is the $\mathbf{j} \times \mathbf{B}$ component in which the electron oscillates at twice the laser frequency.

This is for a linearly polarised laser pulse and is most efficient at target normal. In the case of a circular polarised pulse, the oscillating component goes to zero and reduces the heating of electrons in the plasma.

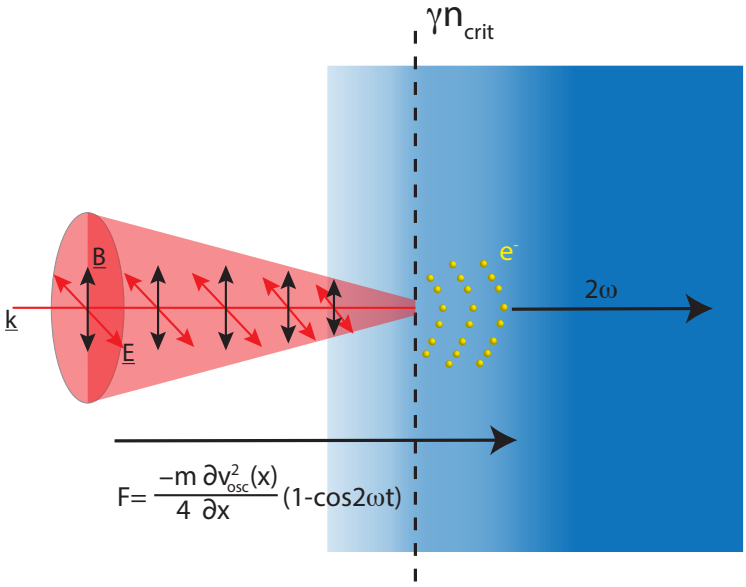

Figure 2.10: Schematic of $\mathbf{j} \times \mathbf{B}$ heating. Electrons are injected into the target along laser axis and at twice the laser frequency. Adapted from [2].

It should be noted that $\mathbf{j} \times \mathbf{B}$ heating is considered the dominate absorption mechanism at peak intensities in this study but the other processes are still present but to a lesser extent. In the next section the propagation of the accelerated electrons inside the target is discussed.

2.8 Fast electron transport

The previous section described the mechanisms by which the laser pulse transfers energy to the electrons [74]. Although the laser pulse cannot propagate beyond the critical surface, the hot electrons produced by absorption processes still propagate into the solid target, generating a mega-ampere (MA) current [75]. The electric field generated by such a current are of the order of $\approx$ TV/m, which

acts to stop the current propagation within a distance of a few microns from the fast electron source. In order for the fast electron current to propagate a relatively colder, return current is generated to maintain local charge quasi-neutrality ($j_f + j_r \approx 0$ where j_f and j_r are forward and return current densities). The maximum value of the current that can propagate without generating a magnetic field to reverse the flow of electrons is given by the Alfvén limit [76]:

$$I_{max} = \frac{\beta\gamma m_e c^2}{e} = 1.7 \times 10^4 \beta\gamma \tag{2.49}$$

where $\beta = v/c$, v is the electron velocity and $\gamma = (1 - \beta^2)^{-0.5}$. For an 1 MeV electron beam the Alfvén limit is found to be ~ 47 kA. This value is considerably less than the predicted magnitude of the fast electron current and experimentally values considerable larger than this are known to propagate. The magnitude of the return current must be large enough to bring the fast electron current below the Alfvén limit in order for the fast electrons to propagate.

For the laser and target parameters in this thesis, the fast electrons injected into that target can be considered to be collisionless as their mean free path is much larger than the thickness of the target. However, the return current propagating in the opposite direction is affected by collisions and as a result the fast electrons are indirectly affected. The hot electron propagation is also affected by the self-generation of resistive magnetic fields this will affect the collimation of the fast electron beam. The magnetic fields also act on the fast electrons directly through filamentation [49, 50].

Once the fastest electrons have reached the rear surface of the target, no return current can be drawn to enable further propagation and a charge separation field of the order of TV/m is generated. Such field leads to the reflection of the slower electron propagation when it reaches the target rear and may be also be induced at the front surface. This effect is known as electron recirculation and takes place over the duration of the laser pulse [77–79]. This effect increases as target

thickness is decreased since the distance electrons have to travel from the front to the rear surface of the target is reduced [77].

2.9 Plasma instabilities

The plasma generated when high intensity laser pulses interact with solids is generally subjected to a variety of instabilities. For ultra thin foil there are a number of instabilities that can occur over the interaction. Some can result in an energy exchange between particles, such as the streaming instability, where co-propagating electron-ion and ion-ion beams transfer energy between particle species [3, 67]. Also, instabilities such as the Rayleigh-Taylor can be detrimental. For laser-driven ion acceleration, Rayleigh-Taylor instability has been shown to cause poor ion beam quality in the radiation pressure regime [80] and also in the direct drive ICF where the fuel capsule is inefficiently compressed [1]. The following section gives a summary of the relevant instability mechanisms and the roles they play in laser driven ion acceleration. A full theoretical description of these and of other plasma instabilities can be found in textbooks by P. Gibbon [1], W. L. Kruer [63] and T. J. M. Boyd and J. J. Sanderson [3].

Rayleigh-Taylor instability

The most prominent instability in nanometer thin foils is the Rayleigh-Taylor instability (RTI), where low density material accelerates a high density material and vice versa. The interface between both materials is subject to the RTI, where perturbation grows. The low density material penetrates into the high density material forming bubbles, whilst the high density material forms spikes as it travels through the low density material [67]. Some examples of such instabilities include mushroom cloud from a nuclear explosion, where low density gas is accelerated and pushed against higher density gas regions above the explosion centre

and supernova explosions where the heavy elements are ejected and accelerated into the interstellar medium surrounding the star. RTI is investigated intensively in inertial confinement fusion, where the instability can result in high amplitude perturbations which lead to inefficient compression of the fuel capsule.

Perturbations that occur at the interface between two densities are due to pressure differences being applied, such as acceleration of one fluid into the other leading to the growth of ripples. These ripples arise from the interchange between the high and low densities as suggested in Fig. 2.11.

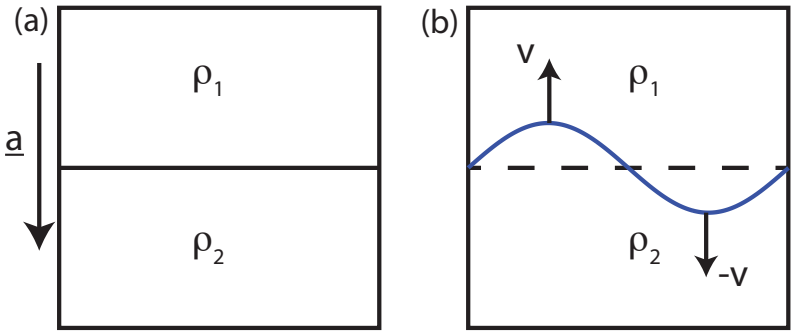

Figure 2.11: Schematic showing (a) the initial conditions of two fluids with different densities separated by a boundary and (b) a perturbed interface with a peak and a trough moving in opposite directions with the same velocity [3].

When a low density fluid is accelerated into a high density fluid, the boundary between both of them becomes unstable and the growth rate of the instability increases exponentially [3]:

$$\xi = \xi_o e^{\sqrt{Akat}} \tag{2.50}$$

where $A = \frac{\rho_1 - \rho_2}{\rho_1 + \rho_2}$, ρ_1 and ρ_2 are the heavy and light fluid densities, respectively, k is the mode number of the perturbation and a is the acceleration.

If the acceleration, a, is directed from ρ_2 onto ρ_1 the situation is stable with the instability growth rate given by a decaying exponential. However, in the opposite case, where the less dense fluid is accelerated into the heavier fluid, the growth

rate increases exponentially leading to the formation of the characteristic bubbles and troughs.

RTI is also observed when intense radiation pressure from a laser pulse interacts with nanometer thin foils [60, 81]. The instability has been observed in the spatial-intensity measurement of laser-accelerated proton beams, where so called "bubbles" were observed [80]. In the case of laser-plasma interactions, the laser photons are the light fluid and the dense fluid is the target electrons. Perturbations on the target front surface can occur from either the structure of the surface or rippling of the critical density surface which act to seed the instability. As discussed earlier, the electrons in the regions of high intensity along laser axis are radially accelerated, resulting in a lower density and regions of higher photon pressure. As a result, the ion population will have the spatial profile of electrons imprinted onto it through the electrostatic field, resulting in a ion beam with bubble structures [80, 81]

Streaming instabilities

Streaming instabilities occur when a beam of particles is driven through a plasma resulting in populations of particles with some relative velocity. The beam of particles injected into the plasma are considered to be the fast population with a background of slow particles. Excitation of wave modes between the streaming species will result in a transfer of energy.

The beam of particles streaming into the plasma generates an unbalanced space-charge separation field, where the electric field growth will act to decelerate the fast particles and accelerate the background particles [82]. The small disturbance in the system will result in the propagation of a plasma wave and will act to accelerate some of the particles in the beam and decelerate others towards the initial perturbation point. This will result in a particle density fluctuation, and if correctly phase matched, the initial perturbation will be enhanced. This results

in a growth of the density fluctuations and a longitudinal electrostatic wave which enables energy transfer between the particles [3].

This type of instability has been identified as a possible energy transfer mechanism between electrons and ions in the relativistic transparency regime [83]. In this case, the electrons are driven by the laser pulse through the target which has become relativistically transparent and have a larger velocity than the TNSA ions. A resonant energy transfer can take place between electrons and ions. This type of two stream instability is known as the Buneman instability [84].

In a simple non-relativistic case, where the electrons stream through background ions, the dispersion relation can be described as [3]:

$$1 = \frac{\omega_{pi}^2}{\omega^2} + \frac{\omega_{pe}^2}{(\omega - kv_e)^2} \tag{2.51}$$

where ω_{pe} is the plasma electron frequency and ω_{pi} is the plasma ion frequency.

For the relativistic case where the Buneman instability plays a role, the growth rate is given by [3]:

$$\Gamma_{max} = \frac{\sqrt{3}}{2\sqrt{2}} \left(\frac{Zm_e}{m_i} \right)^{1/3} \omega_{pe}^2 \tag{2.52}$$

Both equations are representative of a fast electron population streaming with a cold ion background. The concept of the relativistic Bunemann instability as a possible mechanisms for the transfer of energy from volumetrically heated electron and the TNSA ions in ultra-thin foils undergoing RIT was introduced by Albright *et al* [83, 85]. This mechanisms has been identified as a possible energy transfer between transfer mechanism in the Break-out Afterburner ion-acceleration mechansim, which is discussed in the next chapter.

In another study, King *et al* introduced the possible role of ion-ion two streaming [86]. Using particle-in-cell simulations it is shown that if a population of ions can be accelerated where it can propagate through a slow propagating ion popu-

lation, an energy exchange can occur. For ion-ion two streaming the dispersion relationship described in equation 2.51 can be written as:

$$1 = \frac{\omega_{pf}^2}{(\omega - kv_f)^2} + \frac{\omega_{ps}^2}{(\omega - kv_s)^2} \tag{2.53}$$

where subscripts f and s represent the fast and slow ion population, respectively [86]. In a scenario where radiation pressure acceleration (see chapter 3) and RIT take place during the interaction, the relativistic electron stream can be included in the dispersion relation to give:

$$1 = \frac{\omega_{pf}^2}{(\omega - kv_f)^2} + \frac{\omega_{ps}^2}{(\omega - kv_s)^2} + \frac{\gamma^{-1}\omega_{pe}^2}{(\omega - kv_e)^2} \tag{2.54}$$

leading to a energy exchange between three different particle population [86].

Chapter 3

Laser driven ion acceleration

The previous chapter presented an overview of fundamental physics occurring during the interaction of an intense laser pulse with an overdense plasma. This chapter focuses on the mechanisms which drive ion acceleration and the properties of the resulting ion beams. A brief overview of laser-driven ion acceleration is presented, with a description of the different mechanisms that have been investigated and developed. A comprehensive summary of laser-plasma ion acceleration can be found in two review papers by Daido *et al* [5] and Macchi *et al* [87].

Ion acceleration was first studied in the 1960s using CO_2 lasers with intensities $< 10^{17}$ W/cm^2 and pulse lengths in the nanosecond regime. However, since the development of CPA laser systems (see chapter 4) producing ultra-shot pulses and the resulting higher laser intensities, there has been a renewed interest in laser-driven ion acceleration due to high flux ion beams and multi-MeV ion energies obtained from the interaction with overdense plasmas.

Electrostatic fields are required to accelerate protons and heavier ions. These fields are set-up by the charge separation between electrons and ions. The electrons have much lower mass than the ions and gain energy from the laser field and in turn are driven forward resulting in charge separation with an associated electrostatic field. Essentially the electrons act as a mediator to transfer energy

from the laser to ions. The acceleration gradient in a laser-plasma interaction is much larger than that found in conventional radio frequency methods [8].

In order for the laser pulse to accelerate ions to relativistic velocities, the intensity of the laser pulse would need to be greater than $\geq 10^{24}$ W/cm^2. With current technology the peak intensities being achieved are approximately 2 orders of magnitude lower than this [88]. However, future multi-petawatt laser facilities such as ELI may make it possible to reach these intensities.

3.1 Target Normal Sheath Acceleration

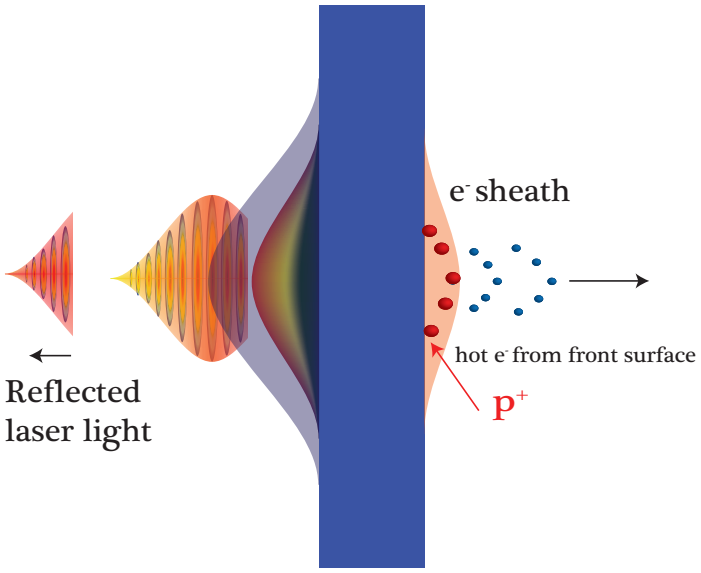

Figure 3.1: Schematic showing a laser pulse interacting with the front surface of a target and the formation of a sheath at the rear surface, resulting in the ionisation and acceleration of the rear surface layers of the target.

The most widely investigated laser-ion acceleration mechanism is target normal sheath acceleration (TNSA) [5, 87]. As discussed in chapter 2, when the high intensity laser pulse interacts with the target front surface, part of the laser energy is absorbed and accelerates electrons through various absorption mechanisms. These hot electrons are accelerated from the front surface into the bulk of

the target material. When they reach the target rear, the sufficiently energetic electrons break out into the vacuum and form a charged cloud. This leaves the bulk of the target positively charged generating a strong quasi-electrostatic field, $\sim$TVm^{-1}, at the rear of the surface. Expansion of the front surface can also occur due to ionisation of the front surface, producing an electron sheath expanding in the opposite direction to the laser propagation. The strength of the rear side electrostatic field can be estimated as:

$$E_{sheath} \simeq \frac{k_B T_e}{e\lambda_d} \tag{3.1}$$

using typical parameters, electron energy $k_B T_e$=1 MeV and λ_D=1 μm, E_{sheath} $\simeq$1 TVm^{-1}

As discussed in chapter 2, the majority of the fast electrons within the target experience recirculation, in which they will be reflected by the sheath field formed at both surfaces [20]. As the electrons reflux between both surface fields, they act to increase the strength of the fields, resulting in enhancing the ion acceleration process [77].

In the level of vacuum typically achieved in large interaction chambers all targets have a thin layer of contaminant hydrocarbons on both surfaces. This consists of water vapour and possibly hydrocarbon compounds from vacuum pumps, which typically lead to the acceleration of energetic hydrogen, oxygen and carbon ions from the sheath field. Due to their high charge-to-mass ratio (q/m), protons are efficiently accelerated by the sheath field [20]. However, there are typically multiple ion species accelerated from the target, creating a layering of the ion layer expansion with the highest q/m ions ratio being accelerated first. The direction of the resulting ion layer expansion is centred on the normal to the target rear surface and this is why this acceleration mechanism is known as target normal sheath acceleration [20, 89].

A number of models have been developed to predict TNSA energy scaling and

the number of ions in the bunch. The most well known model is the Mora model [90]. This is a 1D plasma expansion model which uses collisionless plasma expansion to predict the position and velocity of the ion front. It assumes that the ions are cold and initially at rest with a sharp boundary with the vacuum, while the electron density, n_e follows a Boltzmann distribution:

$$n_e(z) = n_{eo} \exp\left(- \frac{e\Phi}{k_B T_e} \right) \tag{3.2}$$

e is the electric charge and Φ is the electrostatic potential. The electric field at the ion front is found to be:

$$E_{front} \approx \frac{2E_o}{(2\exp(1) + \omega_{pi}^2 t^2)^{1/2}} \tag{3.3}$$

exp(1) is Euler's number. Equation (3.3) can be integrated using $dv_{front}/dt = ZeE_{front}/m_i$ to find the maximum ion front velocity:

$$v_{front} = 2c_s \ln \tau + \sqrt{\tau + 1} \tag{3.4}$$

where $\tau = \omega_{pi} t / \sqrt{e \exp(1)}$ and c_s is the ion sound speed. From this the maximum cut off energy can be found:

$$\epsilon_{max} \simeq 2\varepsilon_o [\ln(2\tau)]^2 \tag{3.5}$$

where $\varepsilon_o = Zk_B T_e$. The analytic solutions also predict an exponential decreasing energy spectrum given by:

$$\frac{dN}{d\epsilon} = \left(\frac{n_{i0} c_s t}{\sqrt{2\epsilon\epsilon_o}} \right) \exp\left(- \sqrt{\frac{2\epsilon}{\epsilon_o}} \right) \tag{3.6}$$

where t is the acceleration time and ϵ is ion energy. A full derivation and further details can be found in [90]. However, the Mora mode is limited to idealistic conditions and general assumptions such as a Boltzmann distribution of electron

energies and single electron temperature. Also, the dynamics of the model are in 1D and therefore limited to resolving 1D features in the proton spectrum. In order to obtain a complete picture of TNSA, 3D particle-in-cell simulations must be performed. An example experimental measurement of a proton spectrum in the TNSA regime is shown in figure 3.2.

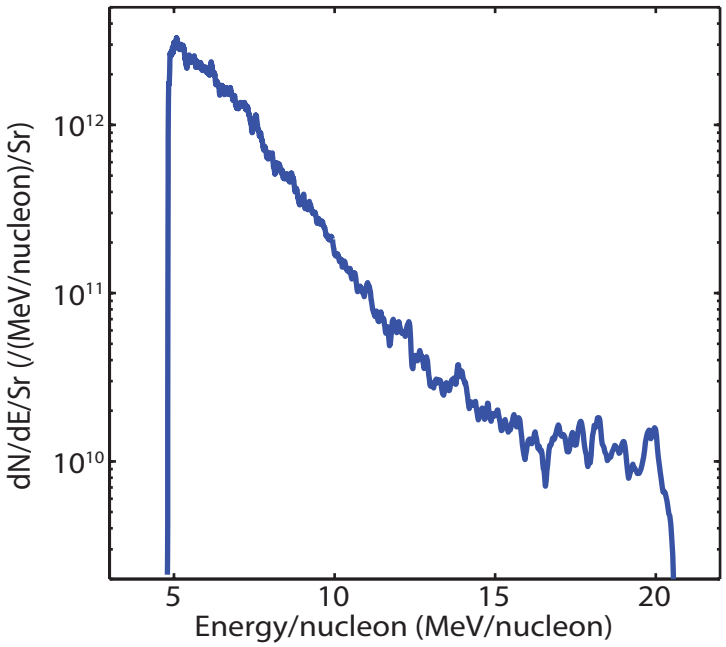

Figure 3.2: Example experimental measurement of the proton spectrum in the TNSA regime.

The rear surface sheath electrostatic field has been shown to have a Gaussian distribution in the transverse direction by Romagnani *et al* [22]. This was measured using a laser driven proton beam to probe the electric field on another target irradiated by a separate laser pulse. The resultant ions accelerated in the sheath field are directed away from the rear surface along the target normal direction.

As the ions experience a Gaussian transverse distribution in the magnitude of the accelerating field, ions located in the centre of this distribution will be accelerated faster than those at a larger radius from the centre. This will result in a Gaussian shaped ion front as shown schematically in figure 3.3 (a).

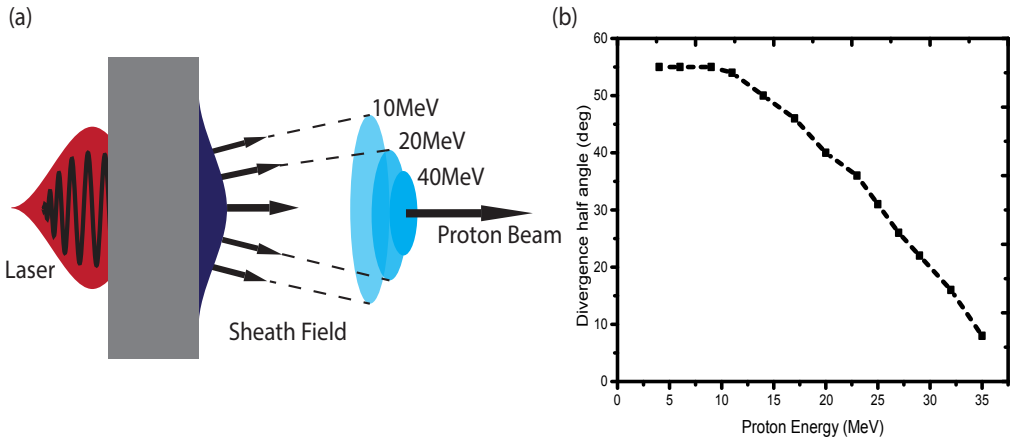

Figure 3.3: (a) Illustration showing the energy dependence of the ion beam divergence in the TNSA regime. (b) Experimental measurements of the proton beam divergence using the Vulcan laser, adapted from [4].

Due to the spatial-intensity distribution of the acceleration field, the highest energy ions originate at the central region of the field, while the lowest energy ions are produced in regions of larger radii, as illustrated in figure 3.3 (a) [91]. However, low energy ions are still produced in the centre. This results in the beam decreasing divergence with increasing ion energy, as shown in figure 3.3 (b).

The sheath area can be estimated from the divergence angle, θ, of the hot electron population traversing the target (assuming a fixed divergence angle) [92]:

$$S_{sheath} = \pi(r_L + L\tan\theta)^2 \tag{3.7}$$

Where r_L is the radius of the laser focal spot and the thickness of the target is given by L.

Ions beams generated in the TNSA regime have been extensively studied experimentally [20,93–97] and numerically [78,98–101]. Early experiments focussed on the origin of the ions, with some arguing that they originated from the front surface [93,102,103] and propagate through the target, while others claimed that

they are generated from the rear surface of the target [20, 104, 105]. By cleaning each surface separately, with an ion gun, Allen *et al* [106] found that the ions originate from both the front and rear surface of the target. Later, this was confirmed by Fuchs *et al* [92,107] who also showed that the number of ions generated from the rear surface dominates over that of the front surface.

By machining structures into the rear surface of the target, Cowan *et al.* [108] mapped the target rear surface into the spatial intensity profile of the proton beam. This method can be used to measure the size of the source as the electrostatic sheath field follows the contour of the target surface. This was done by using targets with equally sized grooves on the rear surface and counting the number of grooves reproduced in the spatial profile of the proton beam [108,109]. For target thicknesses from 5 μm to 100 μm, a source size of a few hundred microns was found. Another method of measuring the ion source size is to place a metallic mesh at a given distance between the target and detector [38]. The grid will imprint on the detector and it can be interpolated back to the target to get a source size.

For the TNSA mechanism, the maximum ion energy is linked to the laser intensity and the pulse duration. Experimental measurements of the maximum proton energy as a function of laser pulse duration and intensity using various laser systems are summarised in Borghesi *et al* [97]. For pulse durations less than 150 fs the maximum energy was found to scale as $\propto I\lambda^2$, while for pulse durations between 300 fs and 1 ps it was $\propto \sqrt{I\lambda^2}$. Until recently the highest proton energies measured from a laser-foil interaction were 58 MeV from a 100 μm plastic foil target [20]. However, using low density CH foils with a target thickness of 900 nm, Wagner *et al* [21], observed 85 MeV protons. This maximum energy is nearly 50% higher than the energy achieved in 2000 by Snavely *et al* [20]. More in-depth reviews of TNSA can be found in two review papers by Daido *et al* [5] and Macchi *et al* [87] where they discuss the progress of laser driven ion acceleration.

3.2 Radiation Pressure Acceleration

Recently, the radiation pressure associated with very intense laser pulses has received a great deal of attention due to its predicted ability to produce ion beams with a mono-energetic spectrum and low divergence. Theoretical studies carried out by Esirkepov *et al* [58] and Robinson *et al* [60] have shown that for sufficiently high laser intensities, radiation pressure acceleration dominates over TNSA in the acceleration of ions [110]. The radiation pressure from a laser pulse directly accelerates electrons in the focal spot, setting up electrostatic fields due to charge separation which results in the acceleration of ions.

Radiation pressure acceleration (RPA) has two distinct mode. The first is hole boring, where the laser irradiates the front surface of the target and pondermotively drives the electrons at the critical surface into the target causing profile steeping. The displaced electrons create an electrostatic field which accelerates the ions. The second phase is light sail, where if the target is sufficiently thin, the compressed electron layer reaches the target rear side whilst the laser drive is still present, enabling a whole section of the target to be accelerated.

The radiation pressure exerted on the target can be approximated by [111]:

$$P_{rad} = (2R + A)\frac{I_L}{c} \tag{3.8}$$

Where A is the coefficient of absorption, R is the coefficient of reflectivity of the laser pulse from the target and I_L is the laser intensity. Note that $R + A + T = 1$ where T is the coefficient of transmission.

Initially it was thought that it would require $I_L \sim 10^{23}$ Wcm^{-2} [58] for RPA to be the dominant mechanism for the acceleration of ions. However it has been suggested that by using circularly polarised laser pulses, a similar effect can be seen at $I_L \sim 10^{21}$ Wcm^{-2}. At this intensity and polarisation the pondermotive heating of the electrons and subsequent expansion of the target is suppressed and

the electrons are compressed and driven into the target [60, 112–114]. The key features of the mechanism are a favourable ion energy scaling, $E \propto I_L^2$ compared to $E \propto I_L^{1/2}$ for TNSA. The resultant RPA ion beam is also predicted to be mono-energetic [58].

Hole Boring mode

In the Hole boring mode of RPA the laser interacts with an overdense plasma as illustrated in figure 3.4 (a).

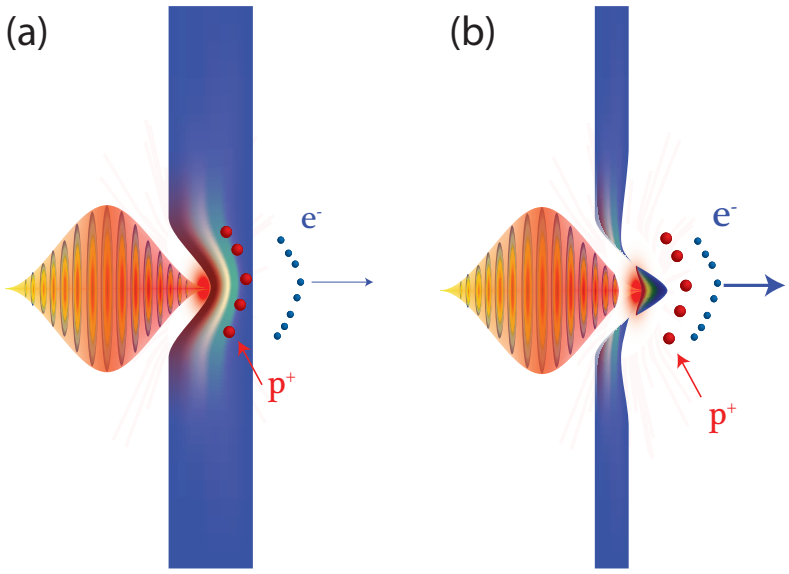

Figure 3.4: Schematic of the (a) hole boring mode of RPA where the electrons at the front side are compressed. (b) light sail mode of RPA

During the initial interaction, the plasma thermal pressure is greater than the radiation pressure. However, as the laser intensity increases the radiation pressure dominates over the plasma thermal pressure and the electrons are pushed forward into the target, creating a density spike in the electron population. As the electrons are quickly piled up in front of the laser pulse, the target ions remain immobile and a charge separation field is generated. This field acts to accelerate the ions [115]. The compressed electron layer driven by the laser forms an elec-

trostatic shock which propagates through the target with ions accelerated by the charge separation field, as shown in figure 3.5. The shock front reflects bulk ions preceding it, resulting in them being accelerated.

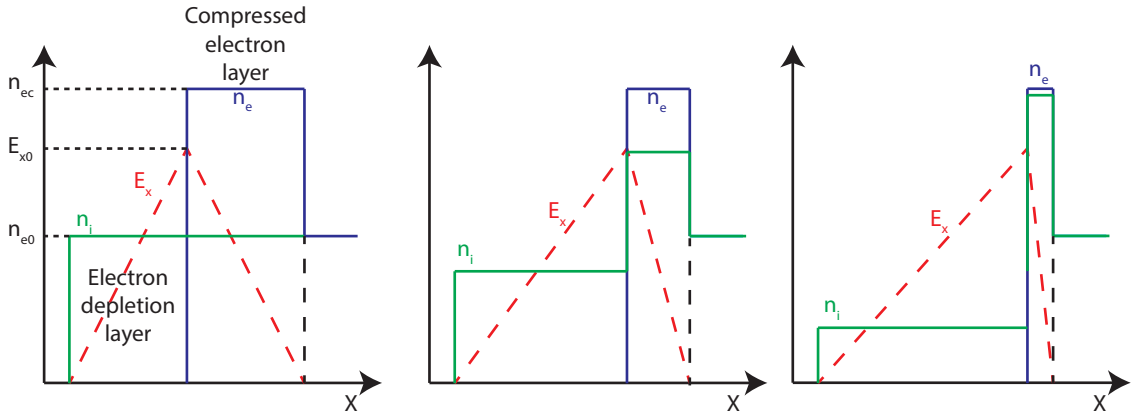

Figure 3.5: Schematic showing the temporal evolution of the hole boring front, with increasing time (a-c), with the electron density in blue, ion density in green and the charge separation field generated in the red dashed line.

Early 1D PIC simulations, Wilks *et al* [61] derived the velocity of the critical surface due to the radiation pressure to find the hole boring velocity. Using conservation of energy and momentum between the laser and particles accelerated by the hole boring front, gives the following expression for non-relativistic hole boring [61]:

$$\frac{v_{HB}}{c} = \sqrt{\frac{n_{crit}}{n_e}\frac{I_L\lambda^2}{2.74\times10^{18}}\frac{Z}{A}\frac{m_e}{m_p}} \tag{3.9}$$

where n_{crit} is the electron critical density, n_e is the electron density, I_L is the laser intensity, λ is the laser wavelength, Z is the ionisation state, A is the mass number and m_e and m_p are the electron and proton mass, respectively.

For relativistic intensities, this equation predicts v_{HB} to be greater than the speed of light. A relativistically corrected hole boring model has been developed by Robinson *et al* [62, 115, 116]:

$$\frac{v_{HB}}{c} = \frac{\sqrt{\Xi}}{1+\sqrt{\Xi}} \tag{3.10}$$

where $\Xi = \frac{I_L}{n_i m_i c^3}$

In this case the v_{HB} is dependent on the laser intensity, the target ion density and ion mass. The model also estimates the maximum ion energy obtained after acceleration:

$$\varepsilon_{max} = m_i c^2 \left(\frac{2\Xi}{1+2\sqrt{\Xi}} \right) \tag{3.11}$$

The hole boring mode lasts up until either the laser pulse has ended or the hole boring front has reached the rear of the target [99].

The monoenergetic properties and favourable energy scaling of the hole boring mode has been demonstrated experimentally. Studies by Haberberger *et al* [117] and Palmer *et al* [118], where CO_2 laser systems were used to produce a monoenergetic ion beam from a near critical density gas jet plasma. These beams have been attributed to hole boring from the front surface driving a shock and accelerating the bulk ions. Using microsphere targets, Henig *et al* [119] measured protons up to 8 MeV accelerated from the initial hole boring front. Hole boring is the dominant mechanism in micron thick targets at sufficiently high laser intensities. For nanometre-thin targets the dominant ion acceleration mechanism transitions to the light sail mode of RPA.

Light Sail mode

For tens of nanometre thick targets, radiation pressure acceleration occurs in the light sail mode, where the whole target volume may be accelerated. All of the electrons within the focal spot of the laser pulse are accelerated forward by radiation pressure, accelerating the ions whilst the target propagates forward with the laser pulse, as illustrated in figure 3.4 (b). This mode of RPA is expected

to dominate over the hole boring when the compressed electron layer is pushed out of the target whilst the laser pulse is still present. As discussed earlier, using a circularly polarised laser to inhibit front surface expansion, allows signatures of RPA can be observed in ultra-thin foil targets at present day laser intensities [5, 87].

As was the case with the hole boring mode ions are accelerated by the strong charge separation field set up when the radiation pressure accelerates electrons from the focal spot of laser pulse. The velocity of the target which is accelerated under radiation pressure can be calculated using the conversation of momentum between the target and the laser pulse is given by:

$$v_{ls} = \frac{(2R + A)\tau_{acc}}{\rho L} \frac{I_L}{c} \tag{3.12}$$

Where ρ is the plasma density, L is the target thickness and τ_{acc} is the acceleration time of the target, which is a fraction of the laser pulse duration. As this is the non-relativistic case, the ion energy is found to scale with intensity squared, $E_i \propto I_L^2$.

Also, equation 3.12 indicates that the maximum energy is obtained from the thinnest foils and lowest densities. The plasma must remain overdense for radiation pressure to efficiently apply pressure and the electrons and ions must remain in unison. If the target is too thin then electrons will be quickly accelerated away from the ions and the electrostatic pressure in the plasma cannot balance out the radiation pressure from the light. Too thick and its inertia prevents efficient acceleration. The optimum thickness for the target can estimated by:

$$L \approx \sqrt{\frac{(2R + A)\epsilon_o I_L}{c n_e^2 e^2}} \tag{3.13}$$

Despite the high ion energies found in numerical simulations, the ability to replicate these results in the laboratory was found to be difficult. Simulations

carried out were either in 1D or featured a laser pulse with a flat top profile with a transverse intensity gradient [60]. It is found that when using a laser pulse with a transverse intensity gradient the target surface buckles and the surface is no longer normal to the incident laser radiation which results in electrons being heated [113]. As the electrons are heated, the plasma will expand giving rise to TNSA-like processes discussed in section 3.1, and transparency processes, which will be discussed later in this chapter.

Dollar *et al.* [120] showed that in thicker targets, electron heating is suppressed. However, for thinner targets it was found that there was no difference in the electron temperature between circular and linear polarisation. The spectra from accelerated carbon ions did show quasi-monoenergetic features similar to the results obtained by Henig *et al.* [121]. In recent experimental studies using a picosecond laser pulse with ultra-thin foils, Kar *et al* [122] have shown evidence of a narrow energy spread in the ion spectra. Using Thompson parabola spectrometers to measure the spectral features and radiochromic film for the spatial profile of the proton beam, a narrow ion beam with a divergence of 13^o was observed [122].

It has been shown that thin foils can become unstable due to the Rayleigh-Taylor like instability when irradiated by a high intensity laser, which prevents the ions being accelerated efficiently [61, 123, 124]. This has been observed experimentally also, where clear bubble-like modulations in the accelerated proton beam were measured [80].

3.3 Relativistic transparency regime acceleration

So far, the laser-driven ion acceleration mechanisms described (TNSA and RPA) require the target to remain overdense during the interaction with the laser

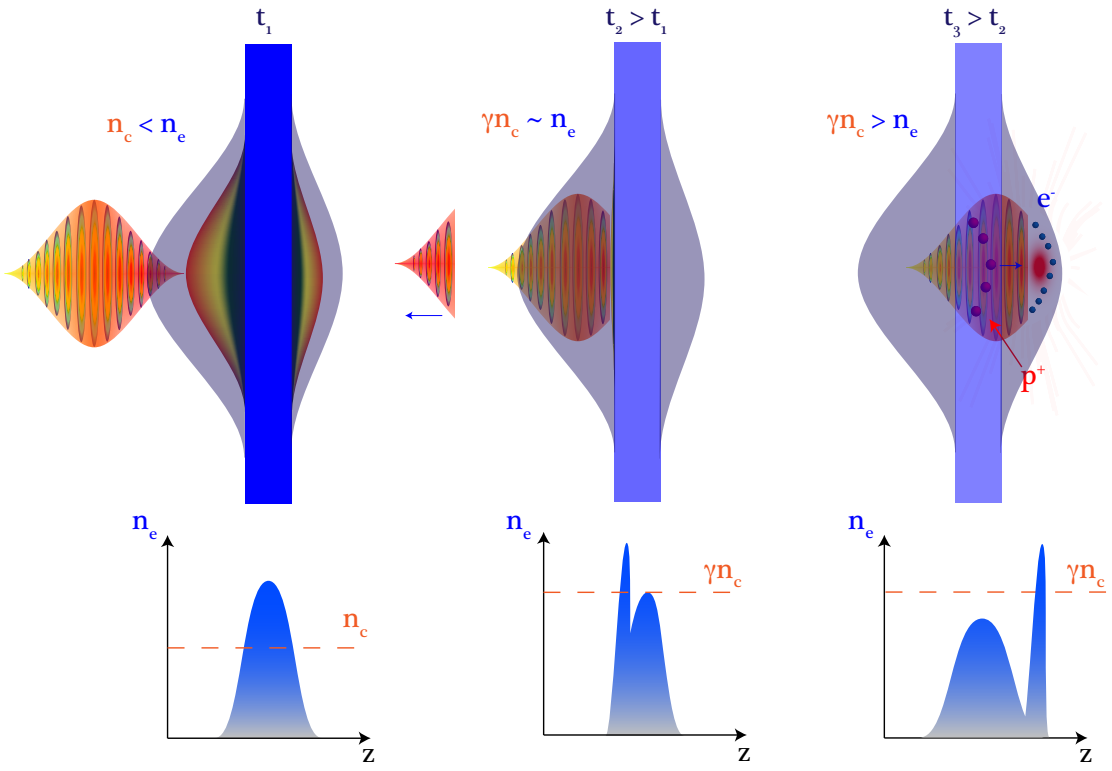

Figure 3.6: Illustration of the Relativistic induced transparency process. At t_1, the rising edge of the laser pulse heats the plasma electrons inducing an expansion of both surfaces. Due to the expansion of the target and increasing laser intensity, at $t_2 > t_1$ the electrons are driven forward into the target by the laser ponderomotive force. At $t_3 > t_2$ the electron density continues to decrease due to the plasma expansion and the increasing critical density results in the plasma becoming relativistically transparent. The laser can then propagate through the plasma which otherwise remain classically overdense.

pulse. In reality, accelerating ions while an ultra-thin foil target remains intact is difficult to achieve, as the target undergoes expansion due to the rising edge of the laser pulse. As discussed in chapter 2, the target may become relativistically transparent during the interaction as the density of the target decreases while the critical density increases due to the γ Lorentz factor. This effect can be labelled relativistic self induced transparency (RSIT) [125]. It is a hybrid of self induced transparency (SIT), where the target density drops below a fixed laser critical density, and relativistic induced transparency (RIT), where the relativistically corrected critical density of the laser pulse is larger than the electron density. For example, for a fully ionised aluminium target, a Lorentz factor of γ =780 would

be required such that the critical density defined by the laser pulse would be equal to the solid density of the target, which corresponds to a $a_o \approx 1100$ or $I_L \approx 10^{24}$ W/cm^{-2}. However, realistically due to target expansion, the target can become underdense at lower intensities than this. The relativistically corrected plasma critical density is defined as:

$$n_{crit}^{'} = \gamma n_{crit} = \frac{\gamma m_e \epsilon_o \omega_L^2}{e^2} \tag{3.14}$$

As discussed in chapter 2, an overdense plasma is defined as the case when the plasma frequency is higher than the laser frequency, $\omega_p > \omega_L$, which in terms of the target critical density can written as $n_e > n_{crit}^{'}$. The critical density is corrected due to the Lorentz factor as the laser intensity increases resulting in an increase in the electron mass. Typically at the peak of the pulse, n_e is observed to drop below $n_{crit}^{'}$ ($n_e < n_{crit}^{'}$) and at this point, the overdense plasma will become relativistically underdense and the remainder of the laser pulse can propagate through the plasma. Figure 3.6 shows an illustration of this process. The onset of relativistic induced transparency has been investigated in detail with ultra-fast temporal resolution by Palaniyappan *et al* [69–71].

The acceleration of ions in the transparency regime plays a role in the context of this thesis as the targets used in the experimental study are in the thickness range of 10-1000 nm. Laser-driven ion acceleration using ultra-thin foil targets is a complex process where multiple mechanisms can take place [126–128]. If we take a step back before transparency occurs, the mechanisms described earlier in this chapter (TNSA and RPA) will take place on the rising edge of the laser pulse while the target is still considered overdense. A number of studies have been carried out to show a significant enhancement of the maximum proton energies in the transparency regime [129–131], which will be discussed in this section.

When the target undergoes transparency it reduces the efficiency of ion acceleration through the RPA mechanism, as this requires the target to be intact. The

radiation pressure expression can be rewritten as:

$$P_{rad} = (1 + R - T)\frac{I_L}{c} \tag{3.15}$$

Using equation 3.15 it can be shown that the transmission of part of the laser pulse inhibits the radiation pressure acting on the target. However, as the transmitted laser pulse propagates through the target, it can volumetrically heat target electrons, generating strong longitudinal electrostatic fields to enhance sheath accelerated ions. This enhancement has been observed in a number of simulation studies using ultra high contrast laser pulses and nanometre scale targets [99,132].

In 2006, simulation and theoretical studies by Yin *et al* [133, 134] and Albright *et al* [83, 85] introduced the term laser 'break-out afterburner' (BOA) to describe the enhanced acceleration of TNSA ions during transparency. The precise mechanism by which energy is transferred to boost ion acceleration is still under active investigation. Albright *et al* [83, 85] suggest that this proceeds via the relativistic Buneman instability this can occur [84] due to the comparable drift velocity between the electrons and ions [83], as discussed in section 2.9. It should be noted, that the simulations carried out showed a self-cleaning effect on multi-species targets. This effect is when the protons are 'self-cleaned' from the rapid expansion of the target, arising due to their higher charge-to-mass ratio, during the TNSA phase. The volumetric heating of electrons thus mainly affects the remaining heavier plasma ions. Analytically, the maximum ion energy in the BOA regime is [135, 136]:

$$\epsilon_{max} \simeq (1 + 2\alpha)qT_e \tag{3.16}$$

This maximum ion energy is shown to scale with electron temperature and the fitting parameter α, which is estimated to be 3 [83, 85]. In this regime, it is necessary for the target to undergo transparency close to the peak intensity of

the pulse for efficient acceleration.

Experimentally, studies performed in the relativistic transparency-enhanced-acceleration or BOA regime have shown a considerable enhancement of the maximum energy of carbon ions and protons [137–139]. Studies by Jung *et al* [138] using an ion wide angle spectrometer (iWASP) [140], demonstrated maximum ion energies occurring off-axis, with an angle between 5^o and 15^o. The energy of the C^{6+} ions off-axis was shown to be a factor of 2 higher than the ions observed along the laser axis. These results showed good agreement with simulations by Yin *et al* [141], where the highest energy ions were emitted off-axis rather than on-axis in two lobes. This is a two stage process which starts with the laser ponderomotive force causing a depletion of electrons in the centre of the laser focus. This results in an azimuthal electron structure [142], which imprints in the ion beam, resulting in high energy ions being accelerated off-axis. An analytical model, based on experimental results, has also been developed by Jung *et al* [143] in the BOA regime for the ion energy scaling and is expressed as:

$$\epsilon_{max} \approx 5\tau_{acc}^{0.28}(a_o - 1) \tag{3.17}$$

Where τ_{acc} is the laser pulse duration in units of femtoseconds. It should be noted that this model only assumes a single species and charge state. This scaling law is also used to derive an expression to find the optimum target thickness (in units of nanometre) for a laser system:

$$L \approx 9.8 \times 10^{-10} I_L^{13/24} \tau_{acc}/n_e \tag{3.18}$$

This expression depends on the target density, n_e, when the peak of the laser pulse interacts with the plasma and n_e is considered a free parameter. Also, laser contrast is not implemented in the model. Similar studies by Henig *et al* [131], tested the effect of target thickness on ion acceleration in the transparency regime.

Carbon ions with peak energies up to 14 MeV/u from a 30 nm DLC target were observed. Also, by doubling the pulse energy the maximum energy of carbon ions increased up to 42 MeV/u [144].

Another mechanism that has been reported to take place in the relativistic transparency regime but for thicker, micrometre targets, is the the relativistically induced transparency acceleration scheme (RITA) [145]. In this scheme, unlike the BOA mechanism, the ion acceleration enhancement is a result of the target's front surface undergoing transparency. In the RITA scheme, the laser pulse produces a plasma due to the expansion of the target's front surface by heating the electrons. The heavy ions are considered to be immobile in this case. As the rising edge of the laser pulse increases, it ponderomotively drives relativistic electrons forward creating a dense build up of electron density just beyond the relativistically corrected critical surface. This effect is referred to as a snowplow, as the laser is pushing the electrons forward over the duration of the pulse. As the electrons are driven forward, a charge separation field is generated between the ions and electrons. This electrostatic potential propagates behind the snowplow and could be used to produce quasi-monoenergetic ion bunches. The peak energy of these bunches could be adjusted by the controlling the rise time of the laser pulse and the density gradient [145]. However, if the laser pulses rising edge time is too short or the expansion of the plasma density is too long, then the snowplow effect will not form. This will result in less efficient acceleration of ions.

A number of recent experimental studies using ultra-thin (nanometre) targets have demonstrated a new understanding of electron and ion dynamics by variation of fundamental laser parameters, such as the polarisation [146, 147] and by inducing a controlled prepulse [126]. Using a 40 fs (FWHM) laser pulse and a 10 nm aluminium target, Gonzalez-Izquierdo *et al* [146] demonstrated for the first time that an ultra-intense laser pulse can induce a relativistic plasma aperture which results in diffraction of the transmitted laser light, which ponderomotively

changes. A double lobe feature in the electron spatial profile was measured and demonstrated to be controllable by varying the polarisation of the laser pulse. The effects on laser-accelerated protons were also investigated in a follow on study [147]. The diffraction features observed in the electron beam due to the laser polarisation are mapped into the spatial profile of the proton beam by inducing modulations in the longitudinal electrostatic field.

Experiments carried out using picosecond laser systems, have shown ion acceleration enhancement by using a controlled prepulse before the main pulse arrives at the target [126]. It was shown that along with the TNSA and RPA mechanisms, a high energy proton component is produced when the target becomes relativistically transparent. By placing the target at an angle with respect to the laser axis, Powell *et al* [126] separated the TNSA and RPA accelerated proton beams to discover that the laser axis component is enhanced. Using 2D and 3D PIC simulations it was found that a plasma jet is formed at the target rear. This jet is confined along the laser axis due to the formation of azimuthal magnetic fields which guide it into the expanded layer of accelerated protons. The portion of the laser pulse which is transmitted through the plasma directly accelerates electrons trapped within this jet. This results in a similar two streaming effect between the electrons and ions as reported by Palaniyappan *et al* [71].

Chapter 4

Methodology

The previous two chapters have outlined the theory and fundamental physical concepts of high power laser-plasma interactions and ion acceleration mechanisms. In this chapter the methods and techniques employed in the experimental and numerical studies are discussed. A range of diagnostics are required to experimentally characterise the interaction, which enables the properties of the plasma to be probed. Modelling techniques are utilised to understand the complex processes of the physics.

The basic concept of laser physics was laid down by Einstein in 1917 when he predicted that an atom could decay from an excited state via spontaneous or stimulated emission. In 1960 the first functioning optical laser was built by Theodore Maiman [148]. Through various developments in laser technology in the past five decades the laser energy has increased whilst pulse duration has decreased, to the point where intensities beyond 10^{21} Wcm^{-2} are available. Increasing the laser power requires either reducing the pulse duration or increasing the energy in the laser pulse. High power laser-plasma experiments such as the ones presented in this thesis are often preformed at large facilities where large teams are employed to develop and maintain the laser systems. The experiments themselves are often performed by a group of visiting researchers and can last

from a few weeks to months depending on the complexity of the experiment. The first week or two of such experiments are typically spent setting up the beamline, defining and referencing the target position, often referred to as the target chamber centre (TCC), and installing and aligning diagnostics to TCC.

In this chapter we will discuss the laser systems used to produce high intensity pulses, diagnostics used to obtain experimental results and the numerical codes used to interpret the data presented in chapters 5-6.

4.1 High power laser technology

Prior to the 1960s, optics were the basis of a relatively small set of industries related to optical instruments, cameras, microscopes and scientific applications. The invention of the laser changed this dramatically, although at first it was generally regarded that 'the laser is a solution in search of a problem' as there were few applications. Now we have lasers in everyday use in communication networks (fibre optics), barcode scanners and laser cutting.

The term laser is an acronym which stands for Light Amplification by Stimulated Emission of Radiation. The amplification of light by stimulated emission relies on the creation of a population inversion in the gain medium, meaning that the population is greater in the upper level than in the lower level. Typically this includes a 4 energy level configuration, illustrated in figure 4.1, with an external energy source, typically a flash lamp, which is used to 'pump' a sufficient number of electrons from the ground level E_1 to an excited level E_2. These electrons then rapidly decay to a metastable state E_3 without the emission of a photon. The energy loss here is considered to non-radiative and is transferred to other atoms in the system. The transition from E_3 to E_4 is the lasing transition, where photons are emitted coherently. This is due to the long lifetime of E_3, which allows a population inversion. After the electron has emitted a photon, another

radiationless transition occurs from the lower laser level E_4 to the ground level E_1.

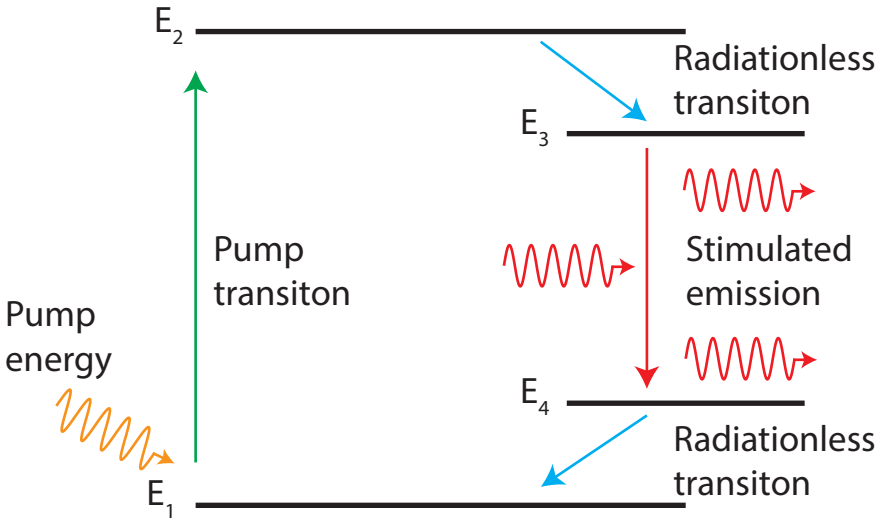

Figure 4.1: Illustration of the stimulated laser transition. In the gain medium electrons are excited from the ground level E_1 to E_2 where it decays to a metastable state E_3. At this stage a population inversion is created and the laser transition occurs when the electron decays from E_3 to E_4. Both E_2 to E_3 and E_4 to E_1 are radiationless tranisitions.

During the initial years after the first laser was built, the development was rapid, with the development of new lasing materials that resulted in improved gain characteristics and optics with higher damage thresholds, which enabled an increase in laser energy. However, the progress of the laser slowed down significantly in the 1970's as laser systems reached the upper limits of optical damage thresholds. At the time, a method was proposed to overcome the intensity limit by increasing the beam diameter of the laser pulse to below the damage threshold. However, increasing the size of optics eventually becomes expensive, which limits the size of the facility that can be built. Thus, the laser systems were restricted to an intensity of $\approx 10^{16}$ Wcm^{-2}, with pulses delivered in nanosecond duration with an energy of a kilojoule. Finally, a solution was found in the mid 1980s when the intensity barrier was overcome with the development of chirped

pulse amplification (CPA).

Chirped Pulse Amplification

CPA technique was first introduced by Strickland and Mourou [18]. It revolutionised laser technology, enabling relativistic intensities, greater than 10^{18} Wcm^{-2} for $\lambda = 1$ μm lasers to be reached [149]. To reach relativistic intensities when focused onto a target, the initial nJ energy seed pulse must be amplified to 100's J to reach the intensities required of a petawatt laser system. CPA was designed to avoid and overcome the damage threshold of the components in the optical systems, in particular the gain medium. The pulse is stretched in time before the amplification by using a pair of diffraction gratings and the intensity of the pulse is reduced as illustrated in figure 4.2.

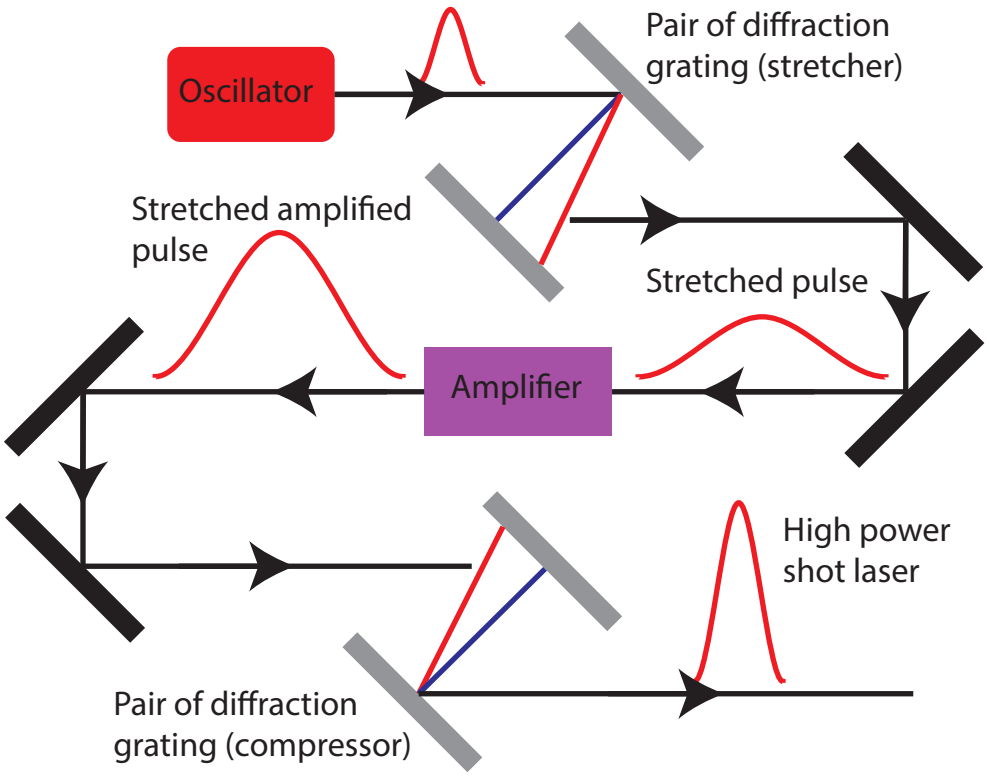

Figure 4.2: Schematic illustration of the CPA laser scheme.

The different wavelengths in the system get dispersed in time by the grating. The pulse is then passed through the gain medium and amplified resulting in a high energy but long pulse durations. A second pair of gratings are used to compress the pulse as close to the original pulse length as possible. Development of CPA allowed the generation of high intensity pulses and petawatt laser systems.

Amplified Spontaneous Emission

As discussed earlier, electrons are pumped in the gain medium to an excited state and when more electrons exist in the excited state compared to the ground state, a population inversion is achieved. Stimulated emission occurs when an electron decays from an excited state to the ground state when stimulated by a coherent laser photon [150]. However, if a photon does not stimulate the excited electron, it can decay to the ground state spontaneously and emit an incoherent photon, as illustrated in figure 4.3.

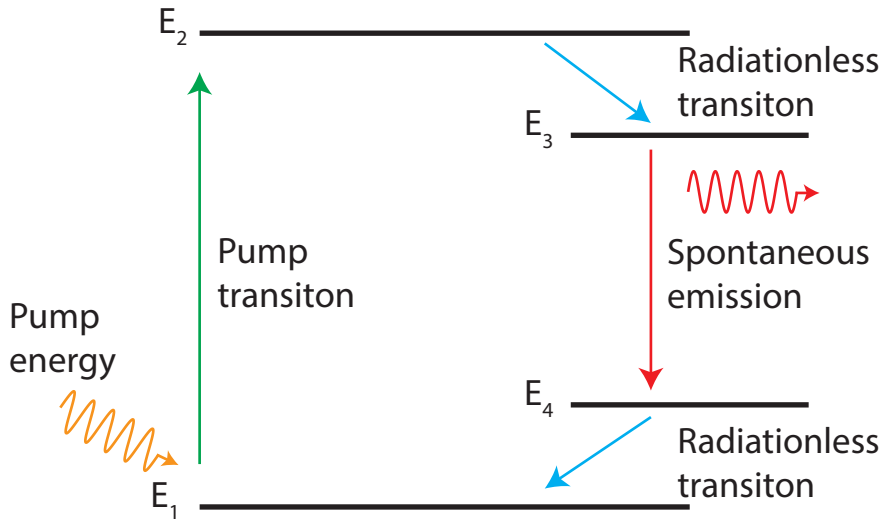

Figure 4.3: Illustration of the spontaneous laser transition. In the gain medium electrons are excited from the ground level E_1 to E_2 where it decays to a metastable state E_3. At this stage a photon is emitted without being stimulatied by another photon and the electron decays to E_4. Both E_2 to E_3 and E_4 to E_1 are radiationless transitions.

This results in a flux of incoherent emission which precedes the peak of the pulse and is be amplified along with it in the amplifier. The amplified spontaneous emission (ASE) can stretch to many nanoseconds before the main pulse. Due to its random nature ASE can seriously alter the physics when the laser pulse irradiates a solid target. With laser intensities in this thesis reaching up to 10^{20} Wcm^{-2}, the pedestal could have an intensity of the order of 10^{14} Wcm^{-2}, above the threshold for ionisation of matter. For micron-thick targets, the pedestal results in pre-expansion of the target and a density gradient at the front surface. However, nanometer thin targets can be destroyed before the peak of pulse arrives due to this pedestal. The ratio between the peak of the pulse and the pedestal is known as the 'laser contrast' and is an important parameter.

Minimising the ASE level of the laser pulse is of key importance to the next generation of intense laser pulses. This can be done by pulse cleaning and amplification techniques such as optical parametric amplification (OPA) in the laser chain, or by employing a plasma mirror in the beam. OPA cannot be achieved by population inversion in a conventional gain medium. Therefore spontaneous emission does not occur and the pulse can be pre-amplified without increasing the ASE level until the main amplification stage. A typical method to clean the ASE up to a nanosecond before the main pulse is to gate it using a Pockels cell. However, when the pulse is temporally re-compressed, a pedestal is still present and therefore the level of ASE needs to be minimised at an early stage. A detailed discussion of amplification methods and OPA is presented in the next section. Additionally, sources of unwanted lasing can arise in the laser chain from internal reflections, giving rise to prepulses in the temporal profile of the laser pulse. This is minimised by implementing wedged shaped optics in the laser chain to redirect the reflection of the laser pulse.

Amplification

There are typically several stages of amplification in a CPA system. After the initial seed pulse has been stretched there will be one or more amplifiers in which the gain occurs. If the gain is high, this can act to enhance ASE as well as the stimulated emission. However, having a gain media with less energy pumped in to it, and the seed pulse making a number of passes, can help to reduce the amplification of the spontaneous emission [150].

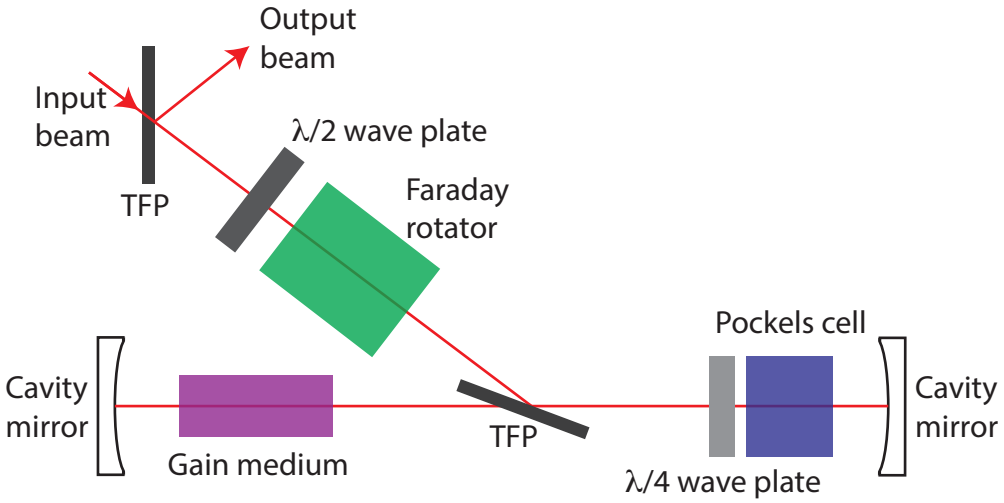

Figure 4.4: Regenerative amplifier setup

A common method of amplification used is the regenerative amplifier and can be used in the oscillator and pre-amplification stage [150]. Here the initial pulse is injected into the optical cavity through a half-wave plate polariser, which changes the pulse polarisation by 45°, and a Faraday rotator, which rotates the polarisation again by an amount depending on its pulse length. The pulse is then passed through a second thin-film polariser (TFP) which reflects or transmits the pulse depending on its polarisation. A schematic of the set-up is shown in figure 4.4. If reflected, the pulse enters the Pockel cell where it behaves like a quarter-wave plate when voltage is applied and will be reflected from the cavity mirror. A second pass reverses the polarisation such that it will be transmitted through

TFP and amplified with each pass of the gain medium. Once the laser pulse has made the required number of passes, a second voltage is applied to Pockel cell which rotates it back to its original polarisation and is reflected out of the cavity. However, in the case where no voltage is applied to the Pockels cell then the linear polarised light will be reflected out of the cavity by the TFP in one round trip. The Faraday rotator acts as an optical switch changing the polarisation to the condition for reflection from the TFP and to the next stage in the laser system.

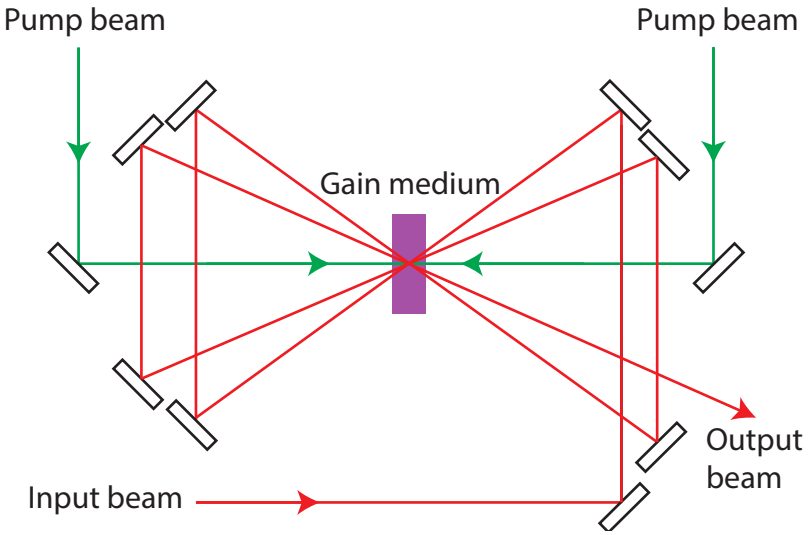

Figure 4.5: Multipass amplifier setup

Another technique commonly used to amplify the laser pulse is the multipass amplifier [150]. The pulse is passed through the gain medium several times by reflection from a series of mirrors, as illustrated in figure 4.5. Since the gain medium is not located within a cavity, a single pass gain may be much higher than in a regenerative amplifier (where the medium has to be pumped harder). An advantage that a multipass amplifier has over a regenerative amplifier is that it introduce less material in the path of the pulse and does not introduce a prepulse. However, the overlap between the signal and pump pulse is not as good as in a regenerative amplifier and thus efficiency is not as high.

Both techniques are typically used in the pre-amplification stage of a CPA laser

system. As it is necessary for laser-solid interactions to have a high contrast laser pulse, and due to the nature of amplification of the stimulated and spontaneous emission using these methods, other techniques are required to minimise the ASE of laser pulse such optical parametric amplification.

Optical parametric chirped pulse amplification

OPA is typically used in the pre-amplification stage of a laser system to amplify the seed pulse from the oscillator. OPA is a different approach to amplify the pulse and is now commonly incorporated into CPA systems in a method known as optical parametric chirped pulse amplification (OPCPA) [150, 151]. The amplification takes place within a crystal that exhibits χ^2 non-linearity. This means there is a parametric transfer of energy between a weaker signal pulse and the stronger pump pulse. If both pulses are matched in phase then the pump pulse is converted to the same frequency, ω_p, as the signal pulse, ω_s. Through the χ^2 interaction, the pump and signal pulses produce a third wave, the idler wave, with a frequency ω_i which is equal to the difference between the pump and signal:

$$\omega_i = \omega_s - \omega_p \tag{4.1}$$

All of the energy from the pump pulse is converted to light in the form of the signal and idler waves, resulting in no thermal energy being deposited in the gain medium. This eliminates the problems caused by thermal lensing in the amplifiers and ASE from the laser pulse. OPA provides a number of advantages over conventional amplification methods. No energy is stored within the medium itself and amplification can only take place when the pump and signal pulse are present. Another advantage is that OPCPA does not suffer from reduction in the bandwidth and can support amplification over a large bandwidth, which is necessary to produce short pulses [150].

Plasma mirror

The intensity contrast of the laser beam plays a vital role in high power laser-solid interactions. Some techniques can be implemented in the laser chain to improve the contrast, however it is never completely eliminated. As the pedestal of the laser pulse may be a factor of 10^6-10^7 lower than the peak intensity of the pulse, when focused onto a target.

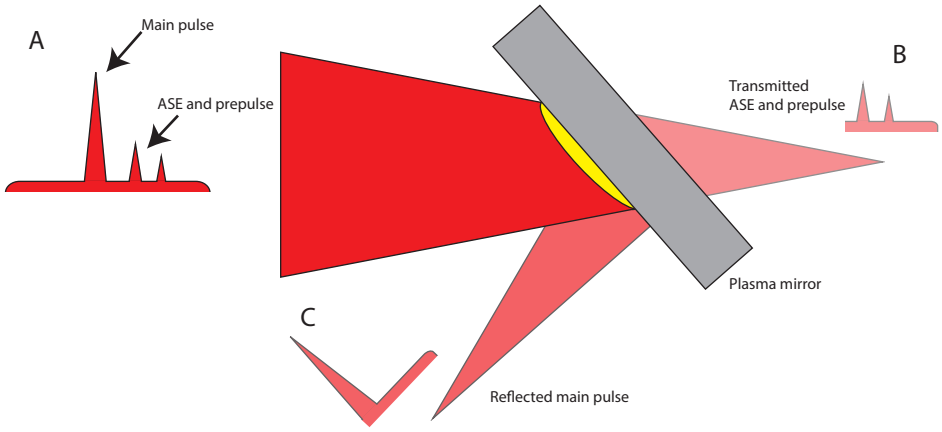

Figure 4.6: Schematic of an intense laser pulse incident on a plasma mirror. The laser pulse with ASE and pre-pulse is directed on to the mirror (A). The low intensity ASE and pre-pulse are transmitted (B) while the main pulse is reflected from the plasma is generated on the front surface of the mirror (C).

To enhance the contrast by minimising the effect of ASE and any prepules in the laser pulse, a plasma mirror can be implemented into the beam path [152]. A plasma mirror is normally comprised of an anti-reflection coated, optically flat dielectric substrate that is placed in the beam path. The results presented in chapter 5 and 6 utilise a plasma mirror positioned in the focusing beam, as shown in figure 4.6.

The principle operation of the plasma mirror hinges on the transition from a highly transmissive medium to a reflective one. The focal spot of the beam is adjusted so that the intensity of the ASE is too low to generate a plasma on

the surface of the glass. When the rising edge of the main pulse exceeds $\sim 10^{14}$ Wcm^{-2} the glass is quickly ionized, forming a thin overdense plasma layer on the front surface of the plasma mirror [152]. The plasma generated reflects the high intensity part of the main pulse improving the contrast by a factor of $\sim 10^2$. The concept of the plasma mirror is illustrated in figure 4.6.

4.2 Vulcan PW laser system

The Vulcan laser system is located at the Central Laser Facility within the Rutherford Appleton Laboratory in Oxfordshire. It delivers pulses into two target areas, Target Area West (TAW) and Target Area PetaWatt (TAP). A schematic of Vulcan is shown in figure 4.7. The results reported in this thesis, were obtained on experiments performed using TAP, where a short pulse PW beam with 600 J is delivered in a nominal pulse length of 600 fs centred at a wavelength of 1.054 μm. Additionally, a second beam can be used to deliver a nanosecond pulse of up to 300 J of energy.

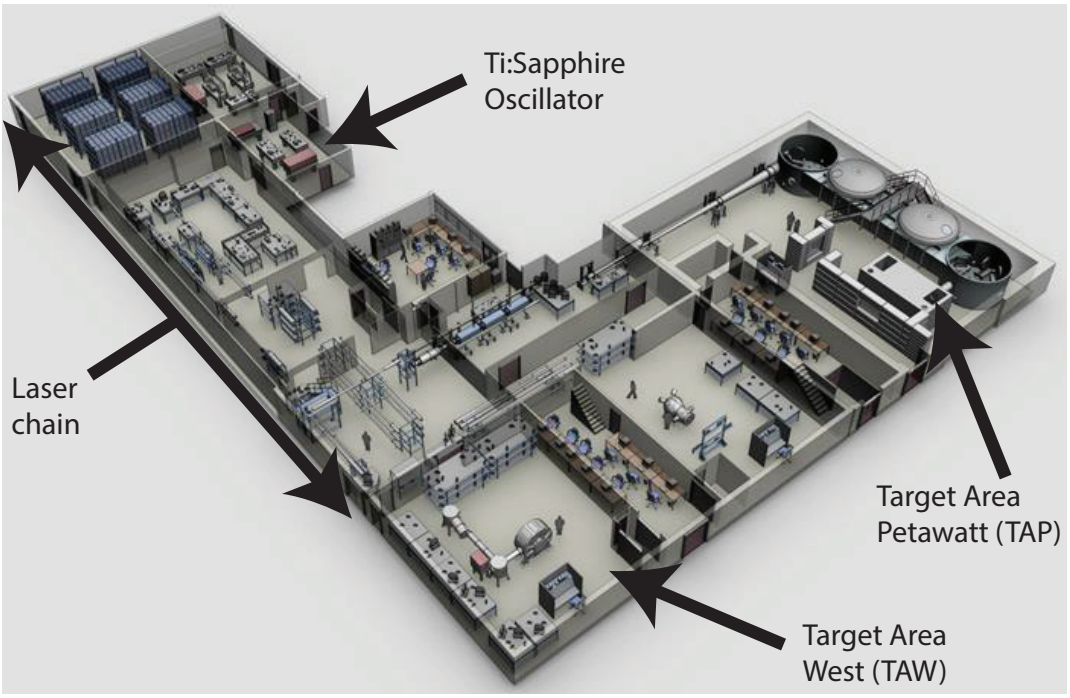

Figure 4.7: Layout of the Vulcan laser and the two target areas [167].

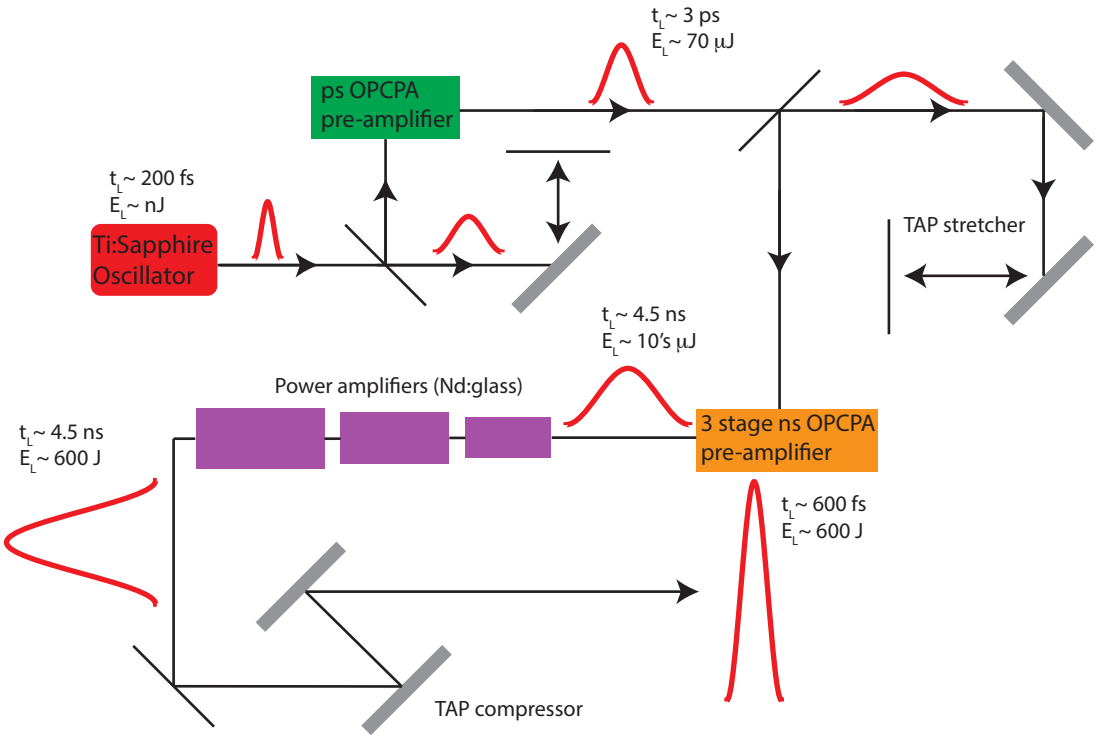

Figure 4.8: Vulcan laser system and amplification chain

An illustration of the short pulse laser beam is outlined in figure 4.8. The TAP laser pulse begins with a Ti:Sapphire oscillator capable of producing 200 fs pulses with nJ energy and a bandwidth of 15 nm. This seed pulse is directed to the picosecond OPCPA stage where it undergoes pre-amplification and is stretched to 3 ps with an energy of 70 μJ [153]. After pre-amplification, the seed pulse undergoes further stretching to 4.5 ns and is then directed to the 3 stage nanosecond OPCPA for further pre-amplification, where the energy is increased from 70 μJ to tens of milli joules [154]. After the 3 stage OPCPA, the pulse is injected into the amplification chain, which consists of neodymium doped glass (Nd:glass) rods and disks. These rods and disks are pumped using a large number of flash lamps, increasing the energy of the pulse to ~600 J. After the Nd:glass amplifiers the pulse is expanded in a vacuum spatial filter to a diameter of 60 cm and is then

sent into the compressor to re-compress it from 4.5 ns to ∼600 fs [155]. The pulse is then directed to the target chamber and where it is focused down to a ~ 6 μm focal spot using a 60 cm diameter f/3.1 off-axis parabola.

4.3 Diagnostics

The previous section discussed the technology and equipment required for the laser to reach the target. This section will describe some of the methods and diagnostics implemented in understanding the laser-plasma interaction processes taking place. The field of laser-plasma diagnostics is too large to be covered in this thesis. However an overview of the different diagnostics used in the field can be found in a review paper by M. Roth [156]. The main diagnostics used in this thesis are the Thomson parabola spectrometer, radiochromic film with stacked filters, a laser transmission diagnostic and a second order autocorrelator.

RadioChromatic film

One of the most robust and common diagnostics used in laser driven ion acceleration experiments is Radiochromic film (RCF). RCF is a self developing dosimetry film which can be used to measure the spatial characteristics and energy of the ion beam. The film is typically made up of a surface layer, an active layer and a clear polyester layer. The active layer consists of a colourless chemical monomer which when exposed to ionising radiation reacts to form an optically dense polymer. For the experiments described in this thesis GAFCHROMIC HD-V2 and EBT2 are used and their composition is shown in figure 4.9. The most significant difference between these types of film is that EBT2 is much more sensitive to lower proton fluxes.

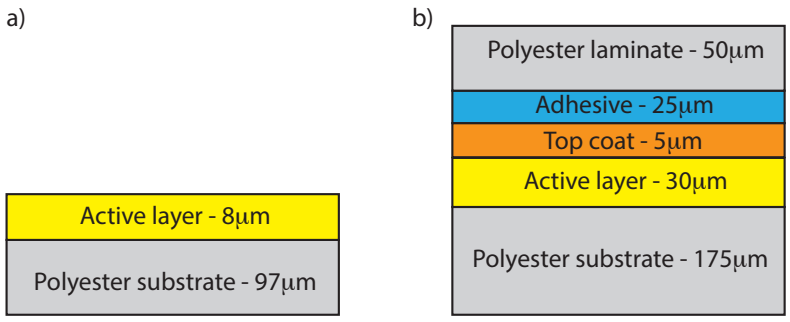

Figure 4.9: Composition of GAFCHROMIC a) HD-V2 and b) EBT2 film

RCF is a simple passive diagnostic which enables instantaneous measurement of particle spatial profile-intensity dose distribution. However, it does require 24 hours for it to develop fully. It is usually stacked with a number of layers with filters between each layer to measure the energy spectrum of the proton beam. The stack typically consists of a front aluminium layer, to stop heavy ions, to prevent the RCF being exposed to any transmitted laser light and to shield it from any debris from the target. The film is layered in a stack configuration with filters, such as copper, placed in between each layer of film, as illustrated in figure 4.10(a). Using different types of material or thickness of specific filters, the energy sampled by the RCF layer can be adjusted if required. Protons above a few MeV energy will stop in the first few layers of the stack, whilst higher energy protons stop further into the stack, with earlier layers acting as energy filters. Also, a stack composed of these films presents a limited maximum energy resolution of 2 MeV due to the thickness of each film. As protons are absorbed in material they present a distinctive response curve called a Bragg peak, illustrated in figure 4.10(b). This peak is due to the increasing scattering cross section between protons and the RCF film, as the energy of protons decrease.

A calculation of the energy deposited in the active layer for a given proton energy can be made using the SRIM (Stopping Range of Ions in Matter), Monte carlo software [157]. Using the data for ion stopping, the energy deposited in the

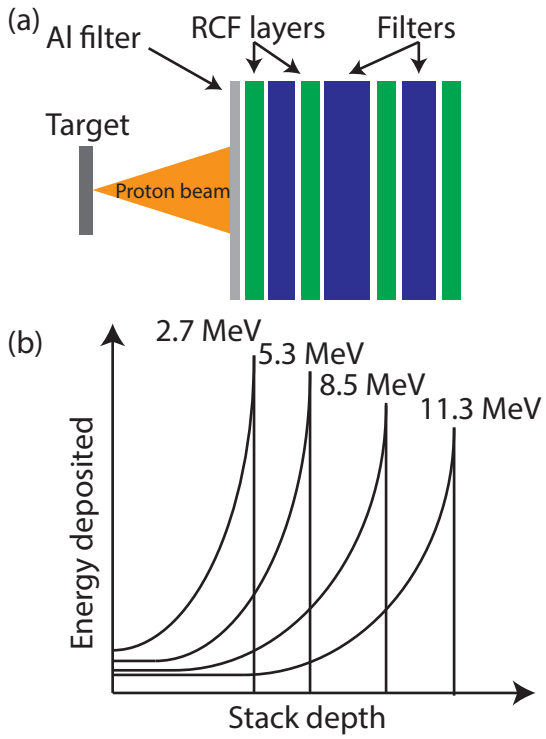

Figure 4.10: Typical stack set up and energy deposited as a function of material depth.

active layer for a range of ion energies can be calculated.

RCF does not give absolute particle numbers, only dose, and therefore it has to be calibrated to a known source every time it is scanned. For the RCF used in this thesis, the calibration for protons was carried out using RCF that was irradiated using the cyclotron at the University of Birmingham, delivering well-characterised proton beam currents. The calibrated RCF is scanned using the same scanner and software setting, thereby giving an absolute dose of the proton energy deposited in the RCF.

Thomson parabola ion spectrometer

A Thomson parabola ion spectrometer is used to measure the energy spectra of different ion species within a small solid angle [158–161]. It uses parallel magnetic and electric fields to disperse ions, that enter a pin-hole, according

to their velocity and charge-to-mass ratio (q/m). This is a particularly useful diagnostic of laser-plasma interactions as a number of ion species are accelerated from the foil. Thomson parabola ion spectrometers use an electric field generated by a potential difference across a pair of electrodes to separate ions according to their q/m and a magnetic field generated by a pair of permanent magnets, held within a yolk to minimise fringe fields to cause deflection of the ions, proportional to their energy. Both fields are perpendicular to the initial direction of travel of the ions. The set-up of the Thomson parabola spectrometer is illustrated in figure 4.11.

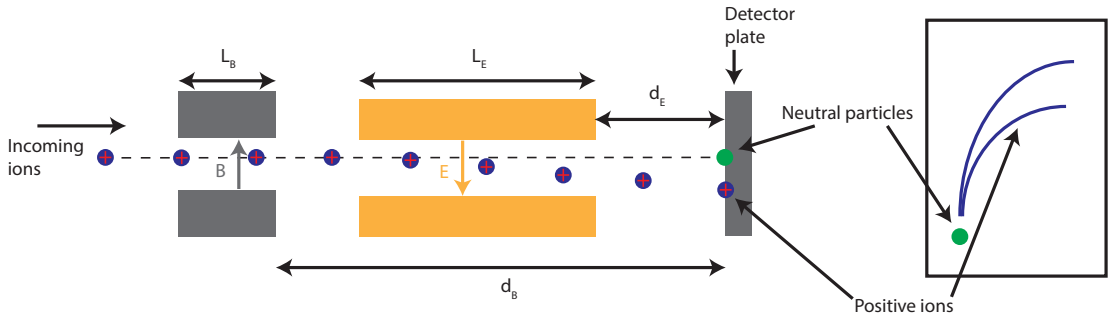

Figure 4.11: Top-down view of a Thomson parabola spectrometer

The Lorentz force equation can be used to calculate the ion dispersion assuming that the fields are uniform and there are no fringe fields. The dispersion due to the magnetic (B_o) and electric fields (E_o) are shown below, where D_B and D_E are the deflections due to the magnetic and electric fields respectively

$$D_B = \frac{qB_oL_B}{mv_z}\left(\frac{1}{2}L_B + d_B\right) \tag{4.2}$$

$$D_E = \frac{qE_oL_E}{mv_z^2}\left(\frac{1}{2}L_E + d_E\right) \tag{4.3}$$

where v_z is the velocity perpendicular to the fields. L_B and L_E are the lengths of the magnetic and electric fields along the axis defined by the ion initial direction

of propagation. d_B and d_E are the drift distances from the magnetic and electric fields, respectively.

The ions accelerated from the laser-plasma interaction are non-relativistic. Ions with different q/m form separate parabolic traces at the detector plane, with the energy determined by the length from the point of zero deflection. Towards higher energies, the ion tracks are closer together and can merge. As these tracks begin to merge it is no longer possible to resolve the maximum energy and distinguish each species by q/m. A number of alternative methods can be used to resolve the maximum energy and increase the charge to mass resolution. One method is to increase the magnitude of the electric field. However, there is a limit to the potential difference that can be sustained across the electrodes before break down occurs. Another method is to increase the length of the plates so that the ions feel the effect of the field over a longer distance, but the low energy ions will begin to collide with the plates causing a discharge. However, Carroll *et al* [162] presents the idea of angling one of the electrodes and Gwynne *et al* [163] shows that the shape of the electrode can be optimised. Finally the drift distance from the end of the electrodes to the detector can be increased so that the ions have a longer distance to travel and will result in an enhanced separation.

Image plate

The detector used in the Thomson parabola spectrometers used in the experiments presented in this thesis is image plate (IP). An example of the parabolic traces obtained is shown in figure 4.12. IP is a reusable film that is sensitive to a range of ionising radiation and was developed for medical purposes such as X-ray radiography [164]. The active layer in the IP consists of phosphor, crystals of europium doped barium fluorohalide phosphor ($BaFBr:Eu^{2+}$) and has a grain size of 5 μm, coated onto a plastic support layer.

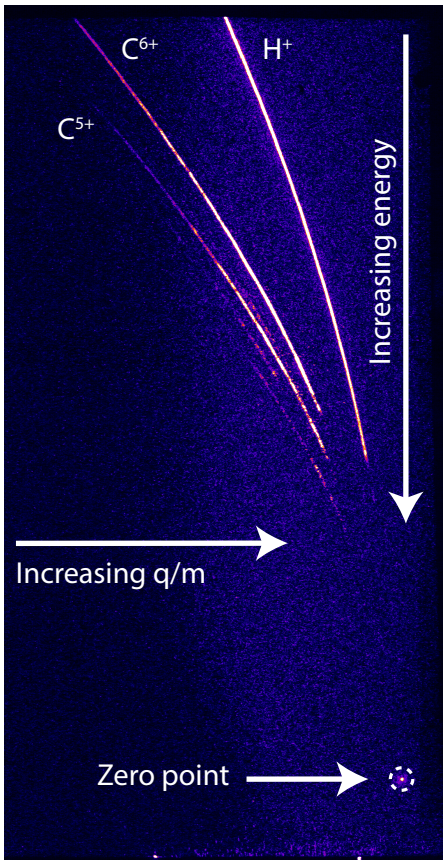

Figure 4.12: Example of raw experimental data on an image plate detector showing dispersed ions from a Thomson parabola spectrometer.

When a charged particle is absorbed in the active layer, electrons from the Eu^{2+} are excited to a metastable state. The electrons can only be released if the plate is illuminated by a laser, typically in the optical wavelength. When the trapped electron is released it will emit a photon at $\sim$ 400 nm by photo-stimulated luminescence (PSL) [164]. The PSL photons are then detected by a photomultiplier. As the metastable state decays and emits a photon, the original signal is lost and therefore it is possible to erase the IP by scanning it multiple times or exposing it to a bright light source.

IPs can be used as detectors for a number of different diagnostic instruments, such as X-ray spectrometers, electron spectrometers and as discussed in the previous section Thomson parabola spectrometers. A disadvantage of IP is that it records all these signals simultaneously which can make the identification of a

particular signal a difficult task. However this can be avoided by using the correct shielding on the diagnostic. Also, IPs typically have to be scanned relatively soon after being exposed to the signal, usually within a few hours, as the excited electrons can spontaneously decay. When using IPs they have to be carefully calibrated. In order to calibrate the flux for a Thomson parabola spectrometer California resin 39 (CR-39), a nuclear track detector which enables absolute ion numbers to be measured, can be used. Calibration measurement for IPs have been made for protons [165] and carbon ions [166].

Laser transmission diagnostic

An important measurement in the investigation of laser-driven ion acceleration from ultra-thin nanometer targets, is the transmitted laser light arising due to target-transparency. The transmitted laser light from the target is intercepted by a Polytetrafluoroethylene (PTFE) screen which is placed $\sim$ 6 cm from the target rear and in contact with the RCF stack, as illustrated in figure 4.13 with an example of the experimental data.

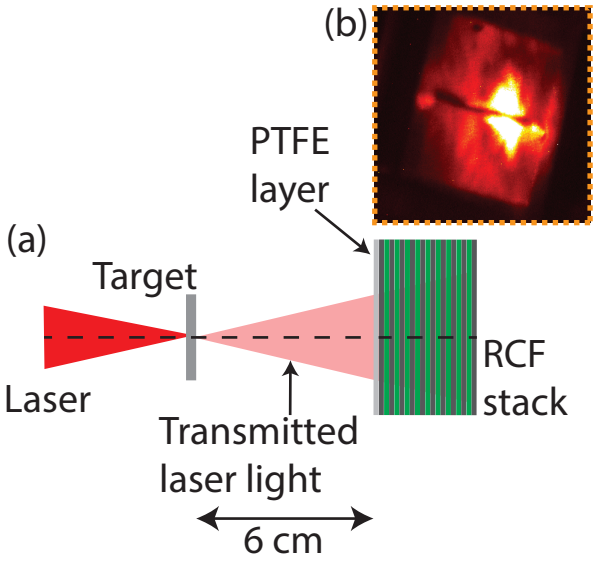

Figure 4.13: (a) Schematic of the setup of the PTFE screen in front of the RCF stack and (b) example of the experimental data

Two CCDs (Charge-Coupled Devices) are placed outside the chamber, which measure the intensity of the transmitted beam in fundamental and 2nd harmonic, as illustrated in figure 4.14. Light is directed to the CCDs using a large aperture mirror and directed through a window to avoid the path of the focussed laser beam. This is due to the inherent electromagnetic pulse (EMP) generated in petawatt laser-solid interactions. The imaging system itself consists of a lens coupled with a beam splitter and two CCD cameras ensuring that the images are both identical. By selection of the appropriate interferometric filter, the cameras measure the spatial-intensity profile of the light at 1ω and 2ω. These filters are placed in front of each camera together with appropriate neutral density (ND) filters to decrease the amount of incoming light in order to avoid saturation and damage to the CCD camera.

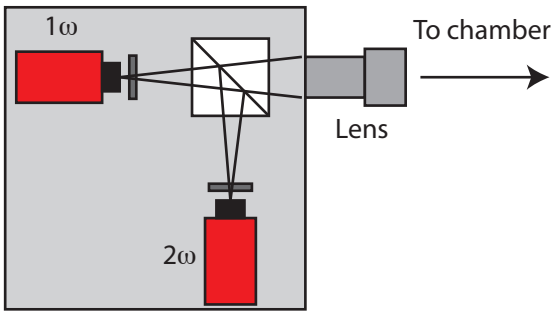

Figure 4.14: Schematic the camera set up to capture the transmission data in 1ω and 2ω outside the chamber.

Single-shot autocorrelator diagnostic

The temporal profiles of pulses shorter than a few nanoseconds are difficult to measure using typical photodiodes. A simple method to temporally measure such a pulse is to use a single-shot autocorrolator [150]. Here, two copies of the pulse, with one delayed in time, are directed into a non-linear crystal with a small angle between their axes of propagation. The beam is then passed through a focusing

lens and the signal that is propagating along the optical axis is recorded by CCD camera. A small hole is cut in the reflecting mirror before the target chamber and a small portion of the beam is picked off. This is then directed to a number of laser diagnostics [167]. A particularly useful diagnostic for this thesis is the near field second order autocorrelator, in which the temporal profile of the laser pulse is measured by taking a line-out across the the captured image. However, the resolution of this autocorrelator is of the order of 100 fs. The autocorrelator can be used to give an indication of the temporal width on the rising edge of the pulse, which is discussed in chapter 6. An example of a trace is shown in figure 4.15.

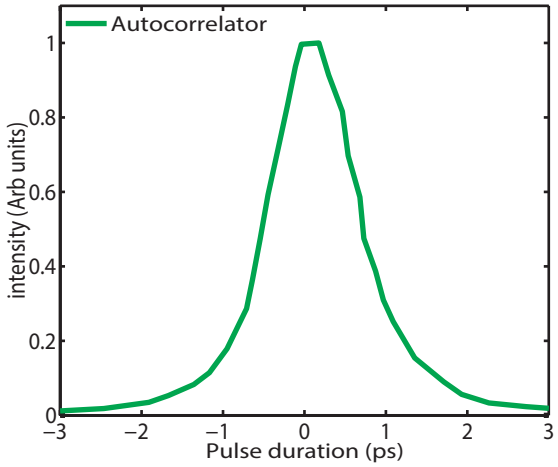

Figure 4.15: Example of the autocorrelation trace extracted from the near field image.

4.4 Simulation tools

Simulations are an important tool for understanding experiment results, since the interaction being studied are only picosecond in duration and hence measurements cannot easily be made. Also not all parameters in a dense plasma can be measured. Even though a range of diagnostics are utilised on the experiment,

the majority of the data is recorded as a time integrated measurement. To gain a full understanding of the fundamental underlying physics numerical modelling is required. These simulations can be used guide experimental design and help with the interpretation of experimental measurements.

PIC codes

Particle-in-cell (PIC) simulations were utilised to investigate the underlying physics of the experiment. PIC codes utilise the kinetic description of a plasma, where it considers the plasma as a collection of particles interacting with the various fields assoicated with the electromagnetic radiation and those induced in the plasma. It offers a good compromise between the amount of detail and calculation time required but are limited by the number of particles and the duration of the interaction that can be modelled in realistic time scales. In PIC simulations the particles are gathered into macro-particles and results in the simulation being less computationally demanding. The basic calculation routine of a PIC code is shown in Fig. 4.16.

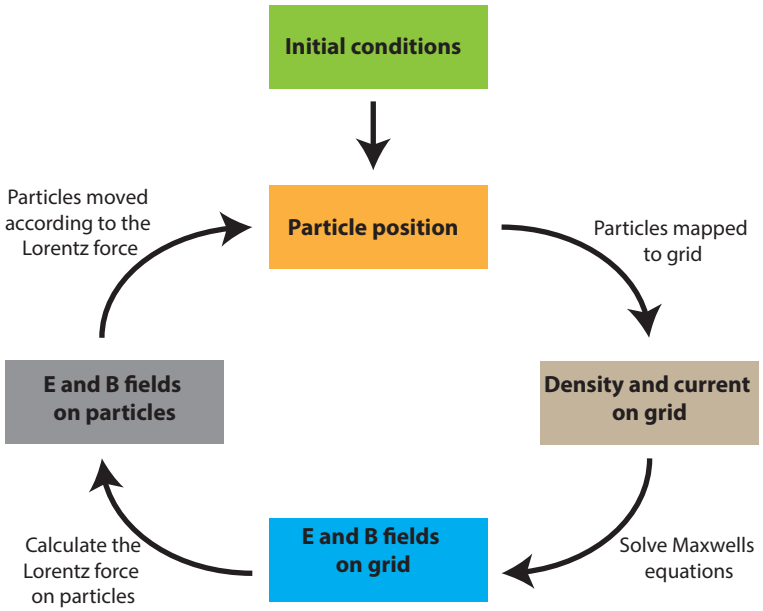

Figure 4.16: Schematic diagram showing the steps involved in a PIC simulation

The initial conditions, such as the laser parameters and particle distributions are defined by the user and is typically based on the experiment parameters or a simplified version of these. For every grid point the current and charge density distribution is calculated and mapped onto the simulation grid. By solving Maxwell's equations the electric and magnetic fields can be calculated at each grid point. The value of these fields at the particle position is calculated by interpolation and the resulting motion is calculated by the Lorentz force. This procedure is repeated for each time step until the simulation is completed. The variables that the user is interested in, such as particle density, particle kinetic energy or the electric and magnetic fields are saved in separate output files at each time step.

With any simulation is it important to avoid numerical aberrations and this can be done by introducing time steps. The PIC code used in this thesis is EPOCH [168], a open source fully relativistic PIC code. An advantage of EPOCH is that users can make alterations to the code to suit their needs. It also has many other features which can be added on such as collisional and QED models.

Chapter 5

Intra-pulse transition between ion acceleration mechanisms

Multiple acceleration mechanisms can take place during the temporal evolution of the interaction of ultra intense laser pulses with thin foils, depending on the laser and target parameters, as shown schematically in figure 5.1. Early in the interaction, when the intensity is $\sim 10^{18}$ W/cm^2, target normal sheath acceleration (TNSA) is the dominant acceleration mechanism. Fast electrons are transported through the target from the front to the rear side, where they form an electrostatic field, accelerating ions into a divergent beam with a thermal spectrum [89]. As the intensity increases to $\sim 10^{20}$ W/cm^2 on the rising edge of the pulse, radiation pressure acceleration (RPA) becomes increasingly important. A layer of electrons at the target front side is compressed and driven forward, setting up an electrostatic field which accelerates ions [58]. Compared to TNSA this mechanism is predicted to result in higher ion energy with a narrow energy spread [122, 169]. However, in the case of ultrathin foils, the remaining target electron population thermally expands, resulting in a decrease in electron density n_e. At the same time, the critical density, n_{crit} of the laser pulse increases due to the relativistic corrected gamma factor, γ. At some point in time when $\gamma n_{crit} > n_e$ the laser

pulse will propagate through the plasma. The onset of transparency will occur in ultra thin foils reducing the effectiveness of RPA [170]. The transmitted laser pulse will volumetrically heat the electrons resulting in an energy enhancement of the TNSA ion population; this effect is known as transparency-enhanced ion acceleration or break-out afterburner (BOA) [133, 138]. In the BOA scheme energy transfer is stated to occur between the electrons and ions, propagating in the same direction, through the relativistic Buneman instability [83]. The Buneman instability is a two stream instability that occurs when the electrons are driven by the laser pulse with a similar velocity to the plasma ions, giving rise to a resonant energy transfer from the electrons to the ions. Alternatively ion acceleration can result from further heating of electrons in the sheath. The multiple ion acceleration mechanisms that occur over the course of the interaction between the laser pulse and the foil are shown schematically in figure 5.1.

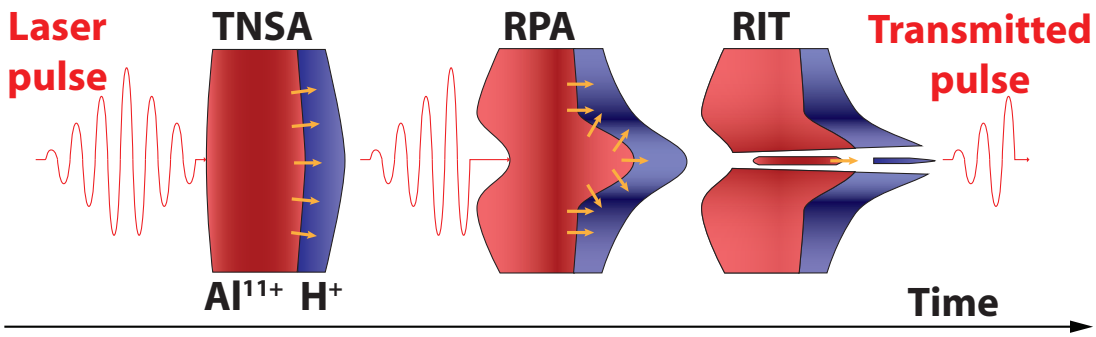

Figure 5.1: Schematic illustrating the intra-pulse transition between different ion acceleration mechanisms in a two species target. (1) TNSA driven by energetic electrons early in the interaction, (2) a hole-boring-RPA phase in which Al ions are accelerated into the back of the expanding proton layer, giving rise to radial expulsion. (3) the onset of RIT and electron energy coupling to the moving sheath accelerated ions.

This chapter presents a characterisation of the intra-pulse transition from the radiation pressure dominated to the relativistic transparency regime in ultra-thin foil targets. The resulting spatial-intensity profile of the measured proton beam

is used to probe the intra-pulse dynamics and investigate the transition between acceleration mechanisms. Numerical PIC simulations are used to understand the temporal interaction and assist in the interpretation of the experimental measurements. The study focuses on the generation of a ring in the proton beam. We note that ring features in the beam of accelerated protons have been observed previously in experiments using Vulcan petawatt laser system. With thick foils (tens of microns) Clark *et al* [93] attributed a measured ring in the spatial profile of the proton beam to magnetic fields forming on the rear surface of the target created by the fast electron transport inside the target. MacLellan *et al* [49, 50] reported ring features in beams from several hundred micron thick targets, arising from self-generated resistive magnetic fields within the target. For thick targets fast electron transport physics plays a key role, whereas this is not the case for the ultra-thin targets investigated here.

5.1 Experimental Set-up

The experiment was performed using the Vulcan petawatt laser, as described in chapter 4. The Vulcan petawatt laser delivers pulses with duration of t=(0.8±0.2) ps at FWHM, which were focused to a spot diameter of 8 μm (FWHM) using a f/3 off-axis parabola. A single plasma mirror was employed to increase the intensity contrast from 10^8 to $\sim 10^{10}$ at $\sim$ 40 ps prior to the peak of the pulse [126]. This resulted in an on-target laser pulse energy of $E_L = (200 \pm 25)$ J, giving a calculated peak intensity, $I_L = 2 \times 10^{20}$ W/cm^2. The laser polarisation was switched between linear and circular by inserting a $\lambda/4$ wave plate in the focusing beam, while the laser focus was aligned to near-normal incidence onto Al foil targets with a thickness, L, varied between 10 nm and 400 nm.

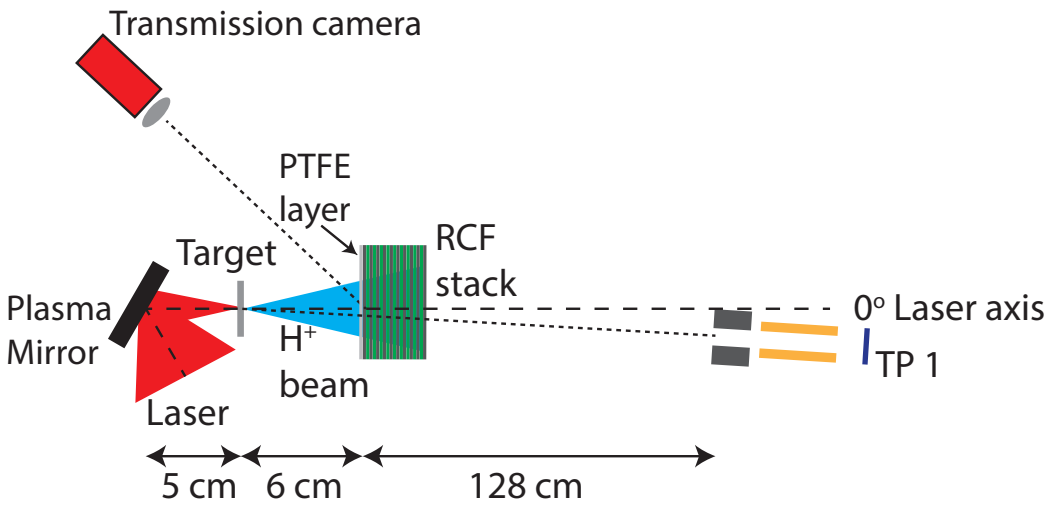

Figure 5.2: Schematic of the experimental set-up. The focussing laser is reflected off a plasma mirror to increase contrast, onto a nanometre scale thickness target. The three main diagnostics: the radiochromic film stack (RCF); with a PTFE layer (for transmitted laser light); and a Thomson parabola, to measure the spatial-intensity and spectral profile of the proton beam respectively.

A range of techniques were used to diagnose laser-plasma interaction. Measurement of the 2D spatial-intensity distribution of the beam of accelerated protons was achieved using a stack of RCF dosimetry film with dimensions of 6.5 cm × 5.0 cm. This enabled the spatial-intensity distribution to be measured in discrete energy bands for proton energies (E_{prot}) ranging from 2.7 to 45 MeV. The stack was positioned 6 cm from the rear of the target, as illustrated in figure 5.2.

The percentage of laser light transmitted through the target was measured for the fundamental harmonic by imaging a thin PTFE scatter screen positioned at the front of the stack. The fluorescence of the screen generated by the transmitted laser light, was imaged using a CCD camera. In order to calibrate the transmitted light on the PTFE screen, the screen was illuminated using the laser without a target in place. The images taken in this shot were used as a reference, enabling conversion of the images taken during normal shots, into laser energy transmitted through the target.

The RCF had a horizontal slit cut through the centre of the stack to provide a line-of-sight to a high resolution Thomson parabola spectrometer (TP) which was

placed at 10° with respect to laser axis. The TP was placed at 10° to allow other diagnostics to have a line of sight to the target. The dispersed ions from the TP spectrometer were recorded on standard BAS-TR2025 (TR) type image plate, calibrated for extraction of the total ion flux. This image plate has no protective layer in front of the active phosphorous layer. This enabled the spectrum of protons and heavy ions to be determined, with a low energy detection threshold of 5 MeV for protons. Early in the experiment, when carrying out preparatory shots, slotted CR-39 was placed in-front of the image plate. This provided an absolute calibration for the image plate in terms of ion numbers and confirmation of the effective magnetic field strength when solving for the ion energy. The minimum energy needed for a proton to be transmitted through the CR-39 was determined using SRIM [171]. The TP was placed 134 cm from the rear of the target, with a 200 μm pinhole at the entrance giving a solid angle of 17.5 nSr.

5.2 Experimental results

Using the RCF stack, characteristic spatial-intensity signatures of individual ion acceleration mechanisms can be resolved. It will be shown below that this enables the transition between mechanisms to be investigated.

Figure 5.3 shows an example of proton spatial-intensity profiles from the laser pulse interacting with a $L = 40$ nm target. At low energies (E_{prot} = 2.7 - 8.5 MeV) the proton beam is dominated by a ring, labelled feature **A**. This feature is present for all targets for which RIT occurs and has been reported in previous studies in the RIT regime [80, 126, 172]. At high proton energies the annular structure is no longer present and the profile is dominated by a narrow high density distribution, feature **B**, for energies E_{prot} = 11.6 - 40.1 MeV. This high energy component of the proton beam has also been reported by Powell *et al* [126]

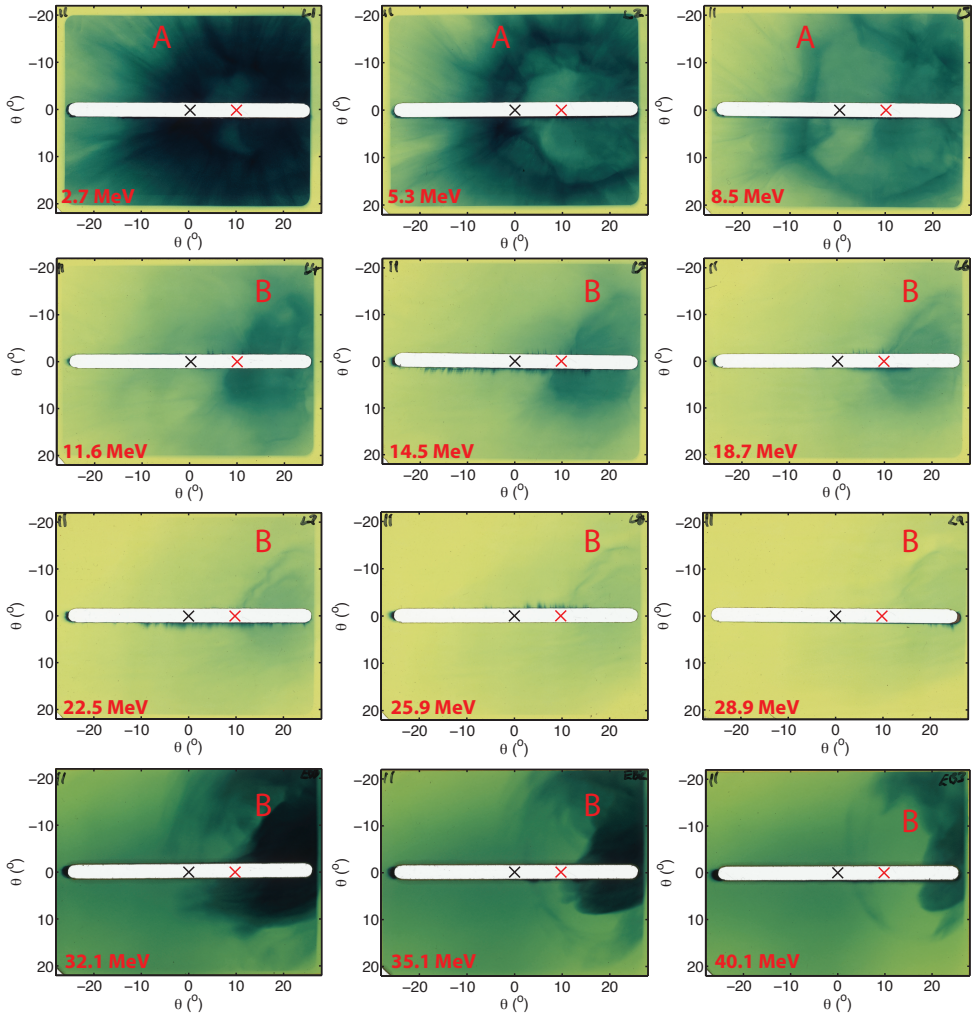

Figure 5.3: Example proton spatial-intensity profiles at stated energies from the RCF stack for irradiation of a 40 nm Al target. The cross at 0° represents laser axis in black and at 10^o indicates the position sampled by the Thompson parabola diagnostic.

and similar features are observed by Palaniyappan *et al* [71], and is explained by the formation of a plasma jet during transparency. In some cases feature **B** can be seen within the annular profile at low energies. From this example, we can see that there are multiple processes leading to different populations of protons which have different spatial-intensity characteristics. Previous studies have been carried out to separate each component of the proton beam and to distinguish between these proton populations [126, 173].

The spectral profile of the proton beam was recorded by the TP and an example of a raw Thomson spectrometer image plate scan is shown in figure 5.4. It should be noted, that both figure 5.3 and figure 5.4 are from the same shot for a $L = 40$ nm target. The spectrum from the RCF and TP is shown in figure 5.5 with the TP spectrum (black line) and RCF spectrum (blue line).

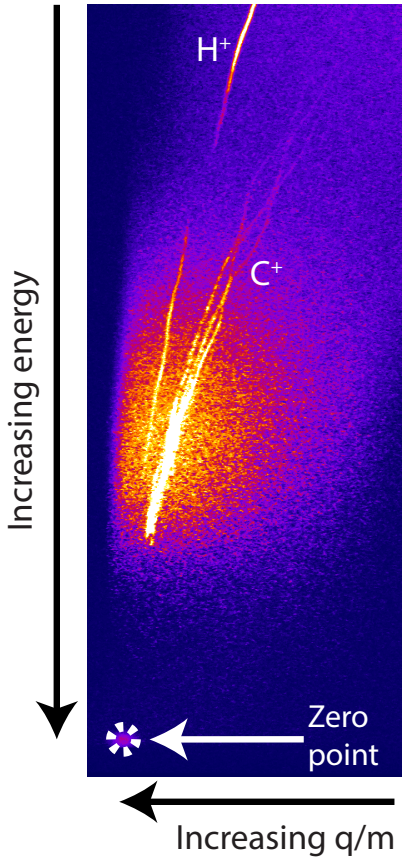

Figure 5.4: Example scan of the image plate used in the dispersion plane of the Thomson Parabola spectrometer for, laser interaction with $L = 40$ nm Al foil. A modulation in the proton track is observed.

As the proton beam is sampled by the RCF stack at discrete energies, a number of points can be extracted to form a spectrum. This enables a full spectrum of the different proton acceleration components to be determined. The spectral data extracted from the RCF is shown to be consistent with the data from the TP in figure 5.5. Both diagnostics have a different low energy cut off, 2.7 MeV and 5 MeV for the RCF stack and TP respectively.

A clear break or modulation can be seen in the proton track in the TP image in figure 5.4, where low energy and high energy components can be distinguished. This modulation is also seen in the proton spectrum in figure 5.5. Typically the spectra measured from micron-thick targets exhibit an exponential drop, for a sheath accelerated beam. Referring back to the RCF data shown in figure 5.3, for the energy range of 2.7 - 8.5 MeV, the annular profile (feature A) is observed. However at energies greater than 8.5 MeV the ring is no longer visible and the collimated structure (feature B) can be seen. This transition from the annular ring structure to the collimated structure may explain the break in the TP spectrum as this could be produced by two different populations of accelerated protons. The low energy spectrum resembles a low energy TNSA profile, whilst the high energy component has a broad plateau-like spectrum. Similar broad ion spectra have been reported by Kar *et al* [122].

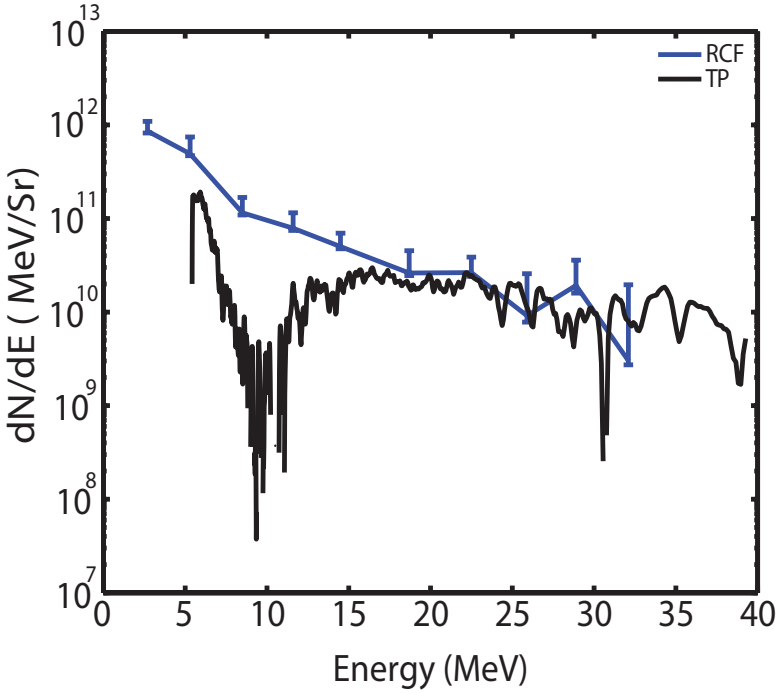

Figure 5.5: Spectrum from the TP (black line) overlaid with a RCF (blue line) for the same 40 nm Al target example data in figure 5.3 and 5.4.

Studies by Powell *et al* [126] and Wagner *et al* [173] have shown that by irradiating the target at an angle, the different components of the proton beam can be separated. In order to compare this result with previous work, two shots were taken, one keeping the target at an angle of incidence $\theta_L = 0°$ and the other at $\theta_L = 25°$. The first layer of the RCF stack, $E_{prot} = 2.7$ MeV, is displayed in figure 5.6.

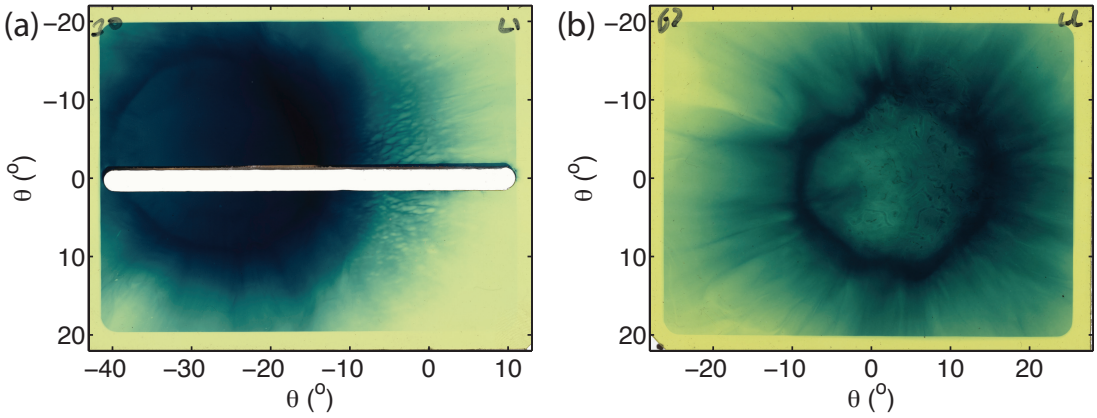

Figure 5.6: Measured spatial-intensity profile of the proton beam from an $L = 10$ nm Al target at $E_{prot} = 2.7$ MeV, for target rotation: (a) $\theta_L = 25°$ and (b) $\theta_L = 0°$.

In figure 5.6(a) $\theta_L = 25°$ and (b) $\theta_L = 0°$. Here we are interested in the direction at which the annular proton ring propagates with respect to target angle. 0° indicates laser axis direction in figure 5.6. In figure 5.6 (a) the centre of the ring is at $\theta = 25°$, whereas in (b) the centre of the ring is close to $\theta = 0°$. This demonstrates that the centre of the ring component of the proton beam is directed along target normal and therefore it is formed during the sheath acceleration phase of the interaction. The high energy component of the beam is always found to be directed along the laser axis.

A third feature that is observed in the spatial profile of the beam is bubble-like structure, which can be seen in figure 5.6 (a) close to the laser axis. These have been observed in previous studies by Palmer *et al* [80] and Powell *et al* [126] using nanometer thin targets and are interpreted as arising due to a Rayleigh-

Taylor (RT)-like instability [80]. In this scenario, the photons act like a light fluid and the plasma acts like the dense fluid. It was found by Palmer *et al* [80] that as the target thickness is reduced, the instability growth rate increases, with the 5 nm-thick diamond like carbon (DLC) target showing the highest degree of instability growth. Small density perturbations lead to a local increase in the laser intensity and therefore radiation pressure, which drives the instability. Although this feature is not the focus of this chapter, bubble-like structures were observed in shots taken on $L < 20$ nm Al targets, with structures also observed with $L =$ 40 nm Al target foils.

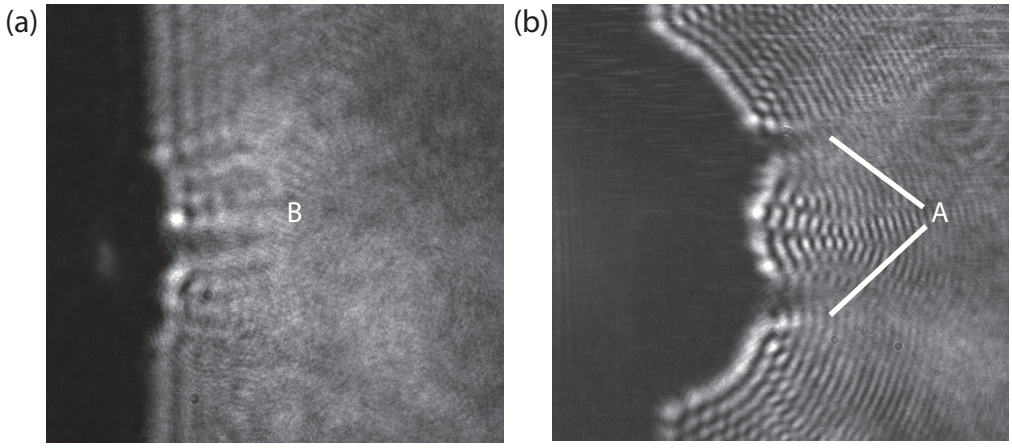

Figure 5.7: Transverse optical probe measurement of the rear surface expanding plasma of a 40 nm Al target at (a) $t = 10$ ps and (b) $t = 120$ ps after the peak of the pulse.

Another diagnostic which can be used to measure a ring-like expansion in the plasma due to density modulation is the transverse optical probe as shown by Powell *et al* [126]. This diagnostic was initially planned to be used on this experiment. However, due to time constraints and difficulties obtaining good quality images no useful data was obtained using the traverse optical probe. Figure 5.7 shows a measurement made by our group on a previous experiment with the same laser parameters and targets [126]. The transverse optical probe enables a measurement of the plasma expansion at a fixed point in time. An example of

optical probing of the expanding plasma at $t = 10$ ps after the peak of the pulse interacts with the target is shown in figure 5.7(a). Evidence of a plasma channel can be seen expanding into vacuum, labelled B. A later time measurement in figure 5.7(b) shows that this process is independent of the ring expansion and occurs on a faster time scale. Figure 5.7(b) shows the rear expansion of the plasma at $t = 120$ ps after the peak of the pulse interacts with the target. The label A highlights features consistent with the annular ring-like expansion and thus with the experimental observations of a ring in the corresponding proton beam. The annular ring profile dependence on target thickness and proton energy is discussed below.

Ring divergence as a function of proton energy

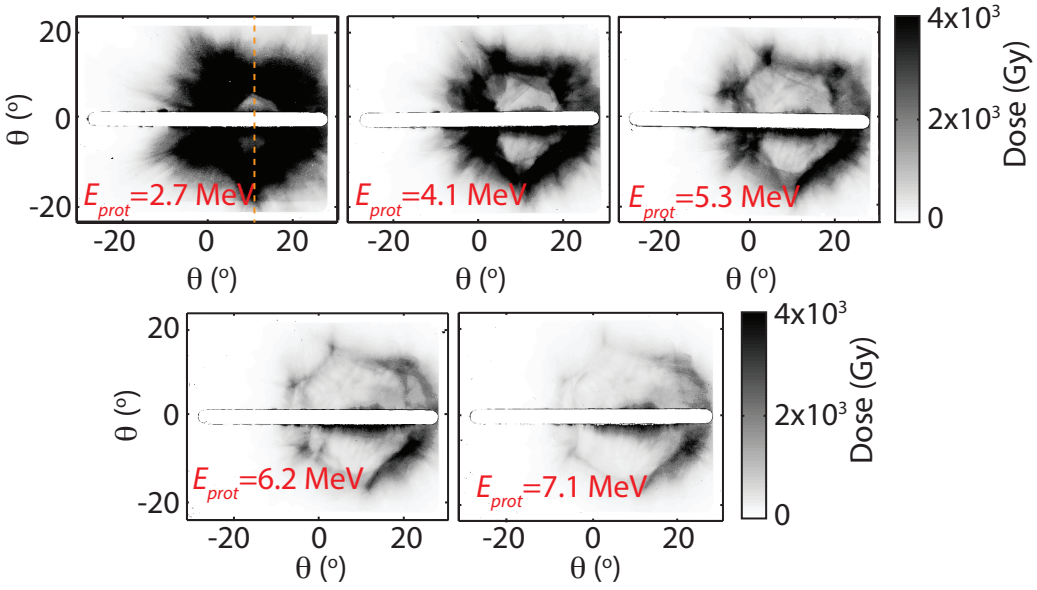

Figure 5.8: Measured proton spatial-intensity dose profile for given proton energies (E_{prot} = 2.7-7.1 MeV) for a $L = 10$ nm Al target.

As discussed earlier, the ring profile measured in the proton beam was observed for targets with a thickness $L \leq 200$ nm and detected up to a maximum proton energy of 8.5 MeV. For higher energies, the annular structure is no longer visible

and a population of low divergence, high energy protons is measured and will be discussed later. The proton ring is centred approximately along target normal for all shots. The opening angle of the structure is observed to vary with target thickness and proton energy. An example of the annular ring profile as a function of proton energy is shown in figure 5.8 for a $L = 10$ nm Al target.

For a fixed thickness of $L = 10$ nm, the opening angle $\Delta\theta$ of the inner part of the ring is observed to increase with E_{prot}. This increase was also measured for $L = 20$ and $L = 40$ nm targets. The corresponding dose profile along the vertical axis was sampled and is shown in figure 5.9. By taking a vertical line-out of the dose profile, it can be seen that the peaks of the beam are increasing in angle with increasing proton energy. The excluded region corresponds to the horizontal slit which was cut through the center of the stack in order to provide line of sight to additional diagnostics.

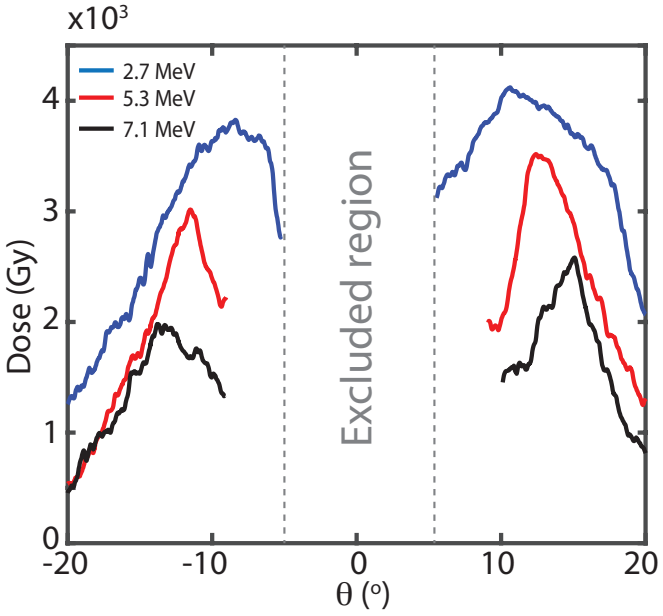

Figure 5.9: Vertical line-outs through the spatial dose profile of the proton beam shown in figure 5.8 for $E_{prot} = 2.7$, 5.3 and 7.1 MeV.

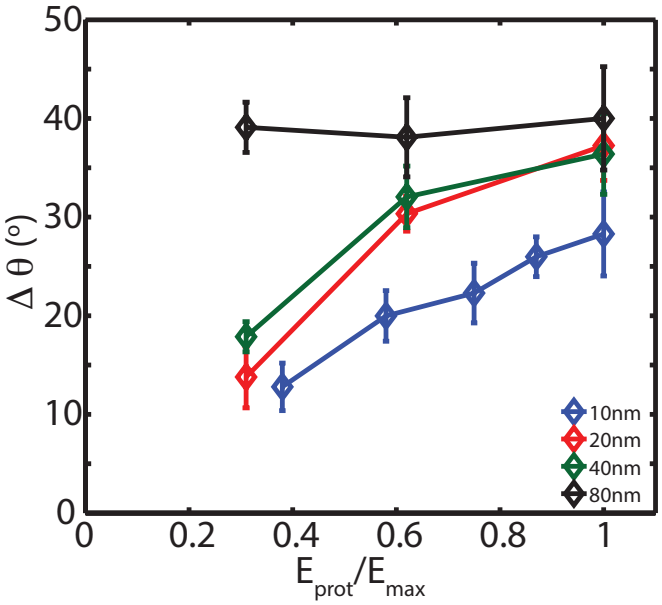

Figure 5.10: Divergence angle $\Delta\theta$ as a function of normalised proton (E_{prot}/E_{max}) energy, from the experimental data for L = 10, 20, 40 and 80 nm.

The quantitative data obtained from the experimental investigation of the divergence angle as a function of proton energy is displayed in figure 5.10 for L = 10-80 nm. The proton energy was normalized to the maximum proton energy of the detected annular component of the beam. The energy dependence of $\Delta\theta$ is shown to increase with target thickness for L<40 nm, whilst for the thicker targets, such as L = 80 nm, the divergence angle does not follow this trend and instead remains constant throughout the RCF layers as E_{prot} increases.

Ring divergence as a function of target thickness

The annular proton beam size is also observed to have a dependence on target thickness, L. Observing the first layer of the RCF stack, E_{prot} = 2.7 MeV, the ring profile was measured for L = 10 - 200 nm, as shown in figure 5.11. The ring is no longer observed for $L \geq$ 400 nm Al target. However it should be noted, that since the maximum measured proton energy decreases with increasing L, and as the ring is only produced in the low energy population, it is possible that it exists at energies below the lower detection threshold (equal to 2 MeV) of the RCF stack.

In figure 5.11 it can be seen that the ring profile in the proton beam increases with target thickness. For L = 10 - 40 nm, radial instabilities, which appear as spoke-like structures, can also be observed in the spatial-intensity profile.

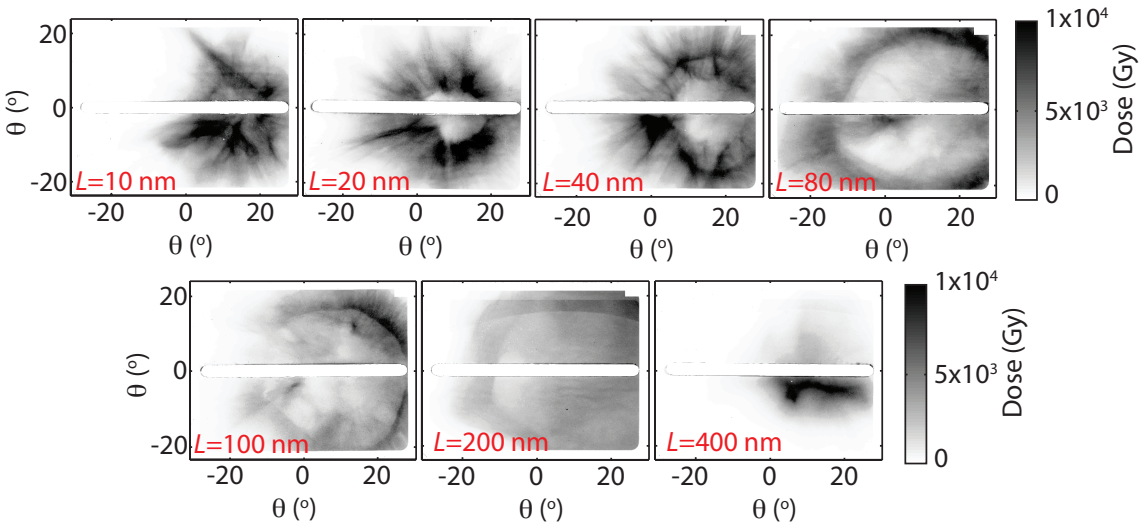

Figure 5.11: Measured proton spatial intensity dose profile for given target thicknesses, L = 10 - 400 nm Al for (E_{prot} = 2.7 MeV)

Figure 5.12 shows the vertical line outs for L = 20, 80 and 100 nm targets which show that the size of the ring profile is increasing. Again the excluded region represents the horizontal slot which was used to provide line of sight to additional diagnostics. Although the line-out is not as smooth as shown in figure 5.9 the peaks of each target thickness can be measured. The opening angle of the profile is seen to increase with target thickness from 20 to 80 nm. However it decreases for L = 100 nm. To quantify the ring profile observed in figure 5.12, the divergence angle is plotted as a function of target thickness in figure 5.13.

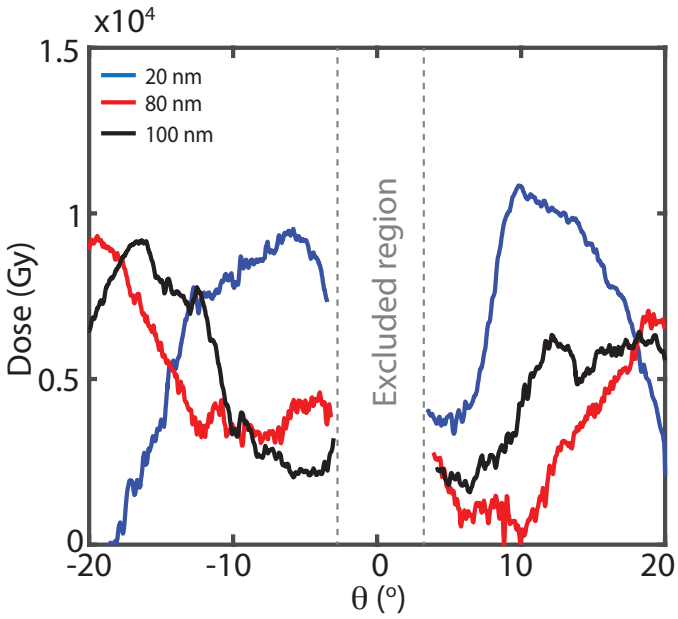

Figure 5.12: Vertical line-outs through the spatial dose profile of the proton beam shown in figure 5.11 for $L = 20$, 80 and 100 nm.

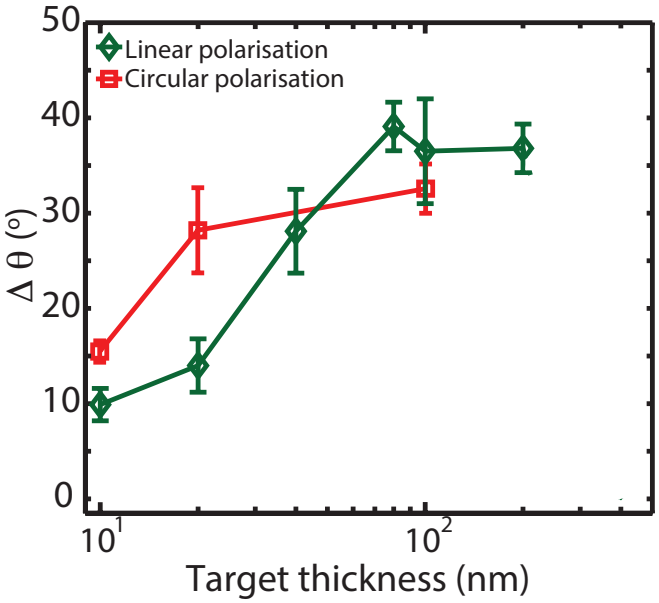

Figure 5.13: Opening angle angle $\Delta\theta$ as a function of target thickness L for linear (green) and circular (red) polarised laser light from the experimental data for fixed energy of $E_{prot} = 2.7$ MeV.

Figure 5.13 displays the full range of targets irradiated with a linear and circular polarised laser pulse in green and red, respectively. It can be seen that the opening angle of the annular proton beam increases for foils $L < 80$ nm and that the largest divergence angle is observed for $L = 80$ nm. Also, it should be noted

that as a plasma mirror is placed in the focussing laser beam line to enhance the contrast, the orientation of the electromagnetic field will be altered slightly due to absorption in the plasma mirror. Therefore, the polarisations are considered to be close to linear and circular polarisation.

For $80 < L < 200$ nm the angle of the ring remains approximately constant and for $L = 400$ nm the ring is not observed above 2.7 MeV. For circular polarised pulses the divergence angle also increases with target thickness, up to $L = 100$ nm. Due to beam constraints and a limited number of shots, only three target thicknesses were irradiated using a circular polarised laser, $L = 10$, 40 and 100 nm. For 10 and 20 nm, the opening angle of the annular structure is larger for the circular polarised case than the linear. This is likely to result from the reduced heating of plasma electrons with circular polarised light. Although we are irradiating the target at $\theta_L = 0^o$ there are two absorption mechanisms at play for linearly polarised light, vacuum heating and j×B heating. Even though vacuum heating is optimised at an oblique incidence angle it will play a role in the energy the electrons absorbed from the laser even at near-normal incidence. Whereas, for the circular polarised light the dominant mechanism is j×B because the oscillating term of the ponderomotive force vanishes and the electron heating effect is reduced. The opening angle of the annular profile of the proton beam in figure 5.13 is larger for the circular polarised light than the linear polarised light. In both polarisation cases, the plasma will expand, however the degree of expansion will be smaller for circular polarised light. Further evidence can be seen for the 100 nm target, where for circular polarised light the target is too thick for hole boring to efficiently accelerate heavy ions. Overall, both laser polarisations result in the same trends, where we see the ring opening angle increases with target thickness, L.

Figure 5.14 shows the raw images of the transmitted linearly polarised laser light for $L = 10$ and 400 nm. The light observed is normalised to the maximum

number of counts measured for the 10 nm case. For the example shown in figure 5.14 it is clear that the maximum transmission is obtained using the thinnest target, $L = 10$ nm, and is no longer observed in $L = 400$ nm.

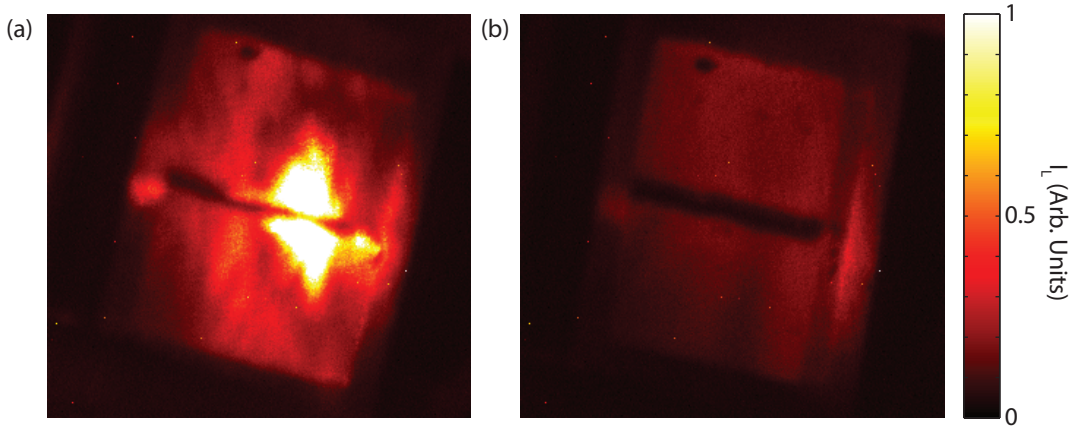

Figure 5.14: Measured transmitted light (at 1ω) recorded with a CCD camera imaging a PTFE screen placed in front of the RCF stack for: (a) $L = 10$ nm; (b) $L = 400$ nm.

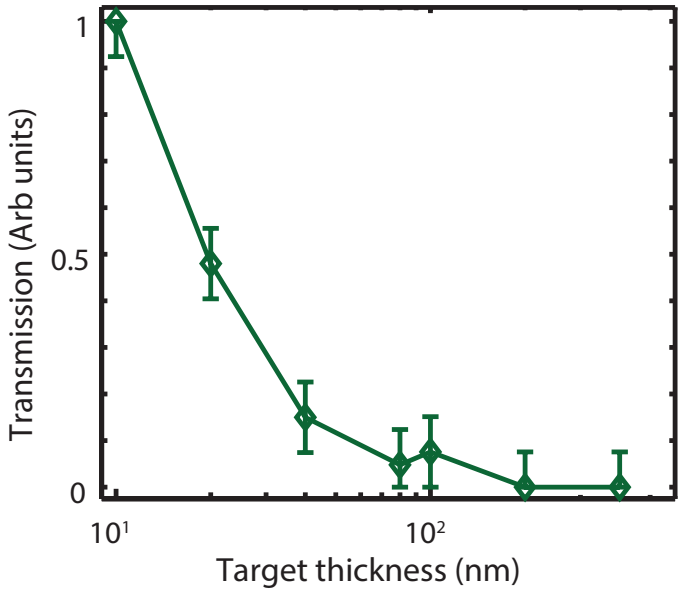

Figure 5.15: Measured transmitted light as a function of target thickness (normalised to the $L = 10$ nm result).

Figure 5.15 shows the normalised transmitted laser light intensity measured for linear polarised light for the full range of target thicknesses and corresponds to the same shots used for the scan of the annular profile as shown in figure 5.13. The laser light transmitted was measured using a CCD camera which measures light imaged on the PTFE screen placed in front of the RCF stack. The camera is triggered just before the laser interacts with the target and we observe a time integrated image of the interaction. The results in figure 5.15 are normalised to the target with the highest transmission value, i.e. $L = 10$ nm. The percentage of laser light transmitted is observed to decrease with increasing L, as expected. The largest percentage of laser light is transmitted for $L = 10$ nm and light is no longer observed for $L =$ of 200 nm [170].

Jet feature

For $E_{prot} > 8.5$ MeV, the annular structure is no longer observed and a low divergence, high energy component is observed, similar to previous studies [126, 172]. In some cases this structure is observed inside the ring or, if irradiating the target at an angle, this structure can overlap with the annular profile causing an enhancement of proton density. The annular beam and the low divergence beam, correspond to two different populations of protons. As discussed earlier in the chapter the ring structure is measured along target normal, indicating that it is driven by the TNSA mechanism. Powell *et al* [126] showed that an enhanced population of protons is accelerated along laser axis due to a self-generated plasma channel, leading to the formation of a plasma jet, which extends into the expanding proton beam. When the target becomes relativistically transparent and the laser pulse propagates through the now relativistically underdense plasma, the laser pulse undergoes self focussing. This arises due to (1) the ponderomotive force expelling electrons from the high intensity regions, forming a plasma channel and (2) the fact that relativistic transparency occurs first on axis and grows

out radially. The electrons accelerated generates an azimuthal magnetic field which maintains the electron jet over an extended distance. As the laser pulse propagates within the plasma channel, electrons in the channel will be directly accelerated [174] and gain more energy from the pulse, resulting in an enhancement to the electrostatic field and thus proton energies. When the target is irradiated at normal incidence, the plasma jet is found within the annular structure.

It is noted that Dover *et al* [172], discusses a similar low divergence structure in the proton beam from nanometre thick diamond like carbon (DLC) targets at zero degrees angle of incidence. They attributed this structure to the buffering effect of heavier, lower charge-to-mass ratio carbon ions pushing the proton layer accelerated by the sheath field. Yin *et al* [133] have identified a "self-cleaning mechanism" via PIC simulations where the expanding, accelerating carbon species in the contamination layer continue to buffer the lower density proton species ahead of the expansion in the relativistic transparency regime. Such a process can occur in many situations in which an intense laser interacts with ultra-thin nanometre foils which have at least two ion species with different charge-to-mass ratios.

Figure 5.16 shows the measured spatial-intensity profile of the low divergence proton beam component observed at higher E_{prot} than the annular structure. The low divergence component of the beam is shown for $E_{prot} = 8.5$-14.5 MeV, for $L =$ 10, 40 and 80 nm. This structure is not measured thicker than this. In some shots this structure reaches energies of 25-30 MeV, but the position of the structure is observed to vary shot-to-shot within an angular range of $\approx 10°$. Figure 5.17 shows the measured divergence angle of the proton beam component shown in figure 5.16. Within the limits of the error bars the divergence angle of the beam does not change as the energy increases. This beam component is therefore less divergent than TNSA beams, a characteristic of RPA mechanisms. The protons here have a relatively low energy compared to what is predicted in simulations

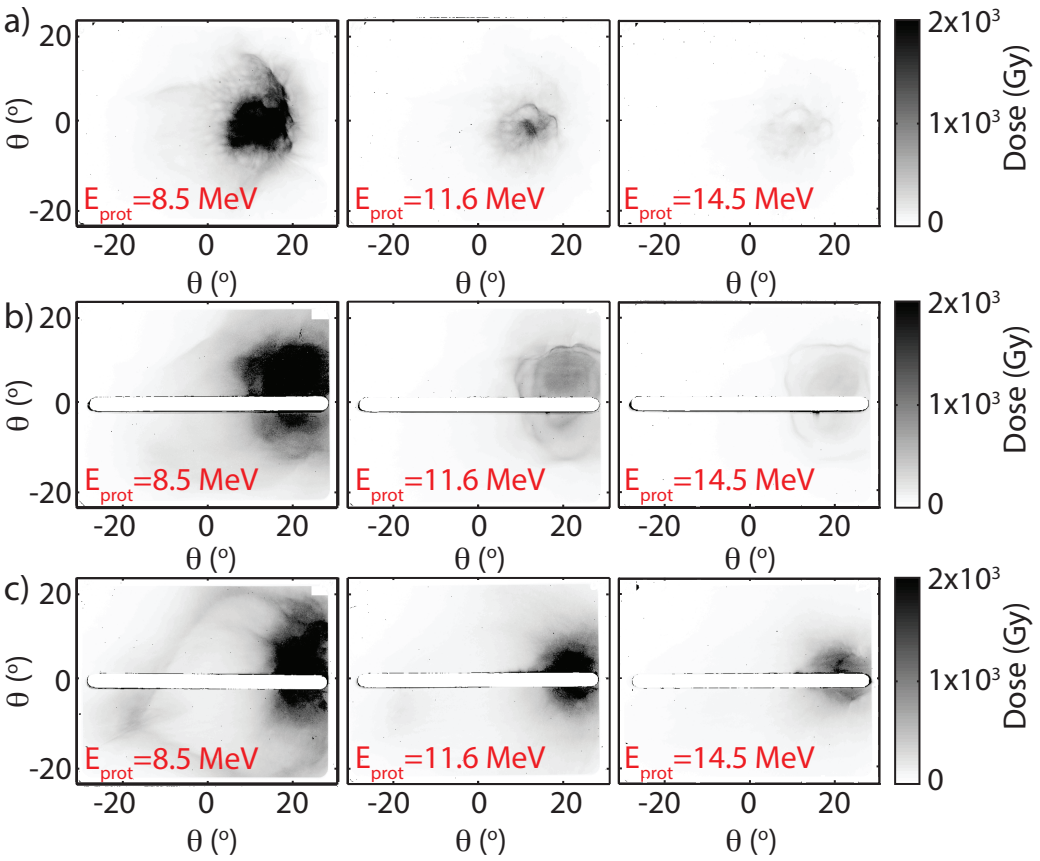

Figure 5.16: Low divergence component of the proton spatial dose profile for given proton energies (E_{prot} = 8.5-14.5 MeV) for: (a) L = 10 nm; (b) L = 40 nm; (c) L = 80 nm.

of RPA for the parameters of the laser. At current laser intensities we are seeing signatures of RPA, however multiple acceleration mechanisms take place over the duration of the laser pulse which makes it difficult to isolate one mechanism in particular.

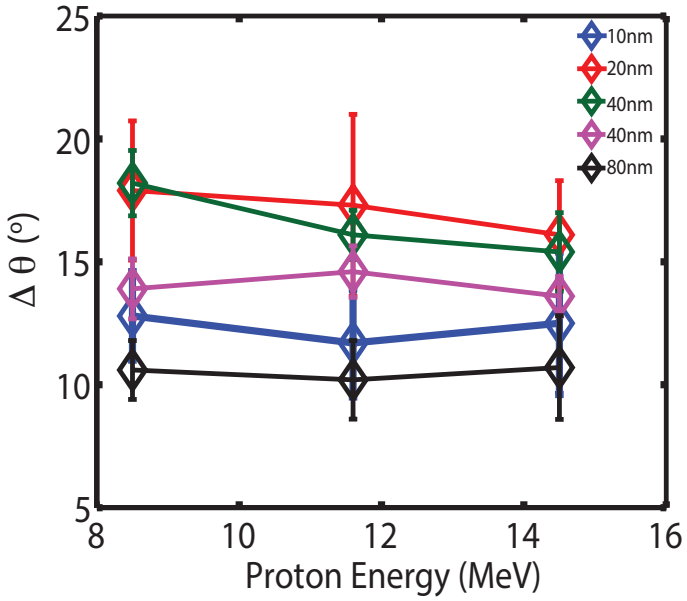

Figure 5.17: Measured divergence angle $\Delta\theta$ as a function of energy of the low divergence component of the proton beam for L = 10, 20, 40 and 80 nm.

5.3 Numerical PIC simulations

To investigate the underlying physics, 2D PIC simulations were performed using the EPOCH PIC code [168]. The dimensions of the simulation box were 130 μm × 72 μm, using 26000 × 7200 cells, in the x and y axes respectively, with boundaries on all sides defined as free-space. The target was initialised as a 2D slab of Al^{11+} ions with a density of $60n_c$ (the density of solid aluminium) with a 10 nm-thick layer of $60n_c$ H^+ on the rear of the target to mimic the contamination layer on the target rear surface in the experiment. Test simulations incorporating an ionisation model have shown that the predominant charge state achieved for aluminium is Al^{11+} for the laser parameters investigated. The electron population is defined to neutralize all of the ions appropriately with the initial electron temperature set to 10 keV. The thickness of the Al^{11+} slab was varied in the range L=20-500 nm, with the hydrogen layer thickness kept constant at 10 nm.

The laser pulse was defined to have a Gaussian temporal profile with a FWHM of 570 fs and was focused to a transverse Gaussian profile with a FWHM of 6 μm at the front of the target. The peak intensity was set to 2×10^{20} Wcm^{-2}. These laser

parameters for the simulation were chosen to replicate the experimental conditions as closely as possible. To account for the laser propagation effects within the expanded target front side [175], it was positioned 30 μm from the simulation box boundary. Computationally intensive test simulations with contamination layers on both the front and rear sides and with binary collisions enabled, show that the front surface proton layer is largely ablated and does not propagate through the Al^{11+} ions. With the exception of these front surface protons, the addition of binary collisions had a negligible impact on the dynamics of the system and these were therefore not included in the simulations reported in this chapter to enable simulations to be performed with available computation resources.

In all of the simulation results it is found that early in the laser-foil interaction (i.e. at the leading edge of the laser pulse profile), electrons are accelerated from the target front side and propagate to the rear side, where they set up a strong, longitudinal sheath field, driving the TNSA mechanism. In this field, the proton population expands faster than the Al^{11+} ions due to their higher charge-to-mass ratio (q/m). This results in layering of the two ion species during acceleration. As the laser intensity continues to increase, the laser light pressure results in the laser pulse hole boring into the target and drives an increased longitudinal expansion of the Al^{11+} ions at the rear side. The maximum degree of this expansion occurs at the center of the laser focal spot where the intensity is highest and decreases off-axis following the Gaussian intensity profile of the laser pulse. During the interaction the electron density drops below the relativistic corrected critical density of the laser pulse. This results in transparency and the transmitted part of the laser pulse drives heating of the electrons over the target volume. As the Al^{11+} layer expands into the rear of the proton layer, the electrostatic field formed at the interface between the two species begins to deflect the slowest protons toward the direction of the local normal to the Al^{11+} expansion profile. The overall target expansion profile is similar to that previously observed

experimentally in intense laser pulse interactions with thin foil targets [176].

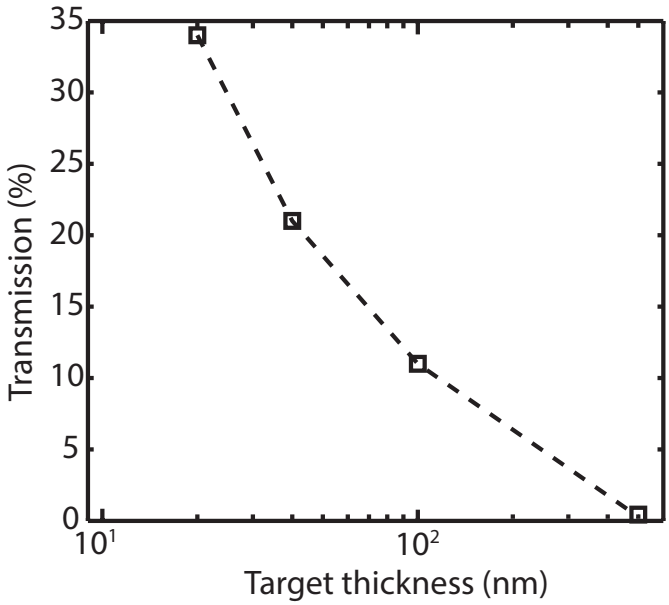

Figure 5.18: Percentage of transmitted light from the simulation as a function of target thickness.

To compare with the experimental measurements, the transmitted light was measured for the simulated target thicknesses, shown in figure 5.18. In the simulation the transmitted light is quantified in terms of the laser electric field at the rear of the target, by calculating the Poynting vector, Eq 2.13, after it undergoes transparency. The transmitted light intensity is normalised to a test simulation with no target, in order to show the relative decrease in intensity arising. This enables the percentage of transmitted laser light to be quantified. The exponential decrease of the transmitted light is reproduced in these simulations. The transmitted light is maximised in the thinnest targets and decreases as the target thickness increases. As expected, the thinnest target, $L = 20$ nm, has the most transmitted light and for $L = 500$ nm no light is transmitted as the target is too thick for the target to undergo RIT over the full thickness. Experimentally, the thickest target, $L = 400$ nm did not undergo RIT. Similarly, in the simulations the 500 nm target does not go transparent. Thus the main features of the onset

of RIT are similar in simulations and experiment.

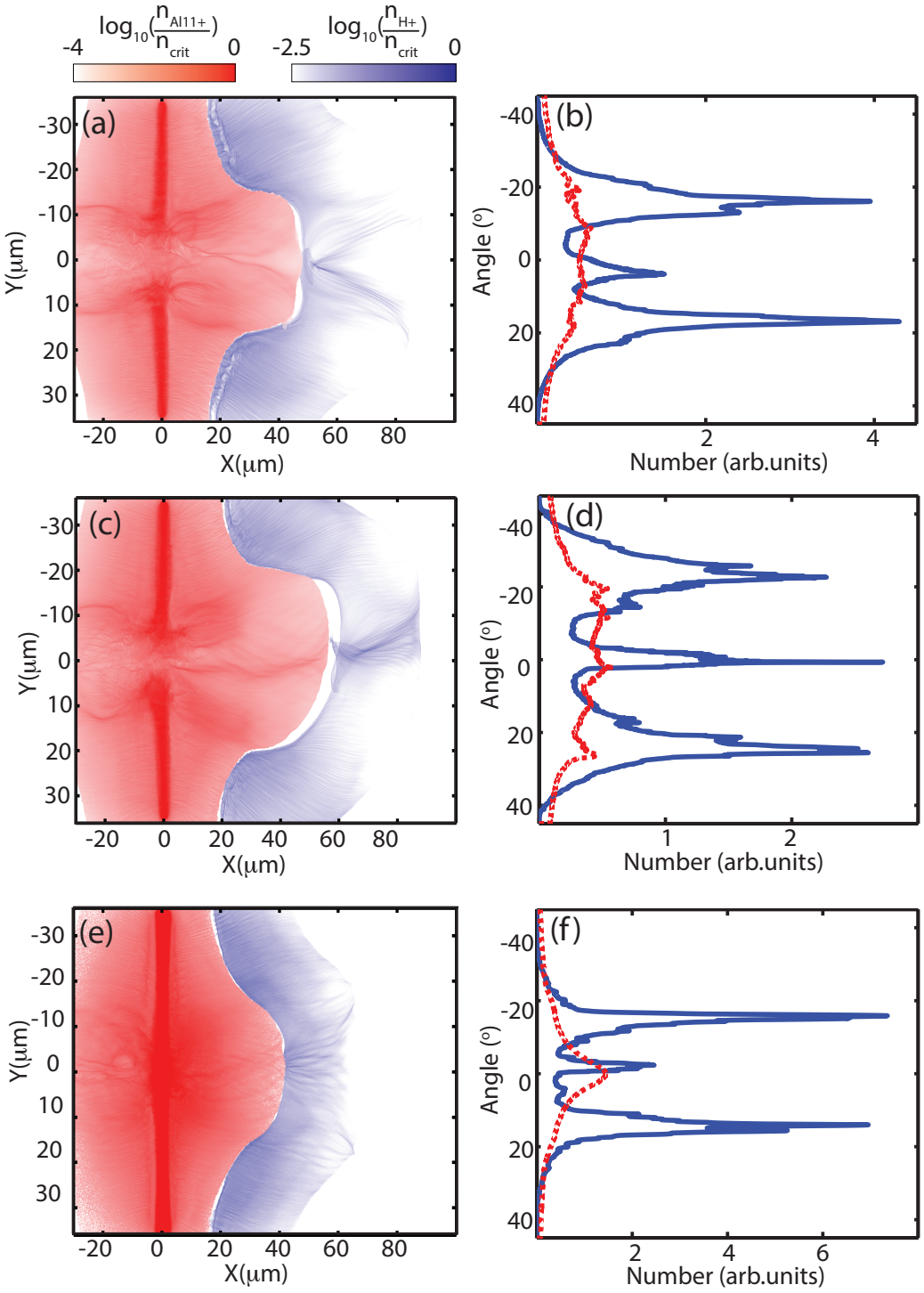

Figure 5.19: Example simulation results showing: (a) Ion densities for the $L = 20$ nm target at $t = 700$ fs: Red - Al^{11+} ions; Blue - protons. (b) Angular projection of the ions, Red dashed line - Al^{11+} ions; Blue solid line - protons, shown in (a). (c-d) same for $L = 40$ nm. (e-f) same for $L = 500$ nm.

Figure 5.19 shows example simulation results for: (a-b) $L = 20$ nm; (c-d) $L = 40$ nm; and (e-f) $L = 500$ nm at the final time step, $t = 700$ fs. $t = 0$ fs is defined as the time when the peak of the laser pulse interacts with the front surface of the target. On the left (a,c,e) the density distribution of the Al^{11+} ions (in red), and protons (in blue), are presented. The right side of the figure (b,d,f) shows the projected distribution of the ions in the same colour scheme. Using the particle momentum data output from the simulations, the particles are projected 6 cm from their positions shown in each time step, to compare with the experimental results. From the density plots shown in figure 5.19, the majority of protons are observed to be distributed off-axis, with very few along the laser axis. This is confirmed in the ion projection figures where a larger population is seen to be accelerated off-axis. As the simulations were carried out in 2D, the ring structure can be observed in the Y dimension as two off-axis peaks and the separation of the two peaks can be measured to give the opening angle of the ring. The annular structure is observed for all target thicknesses, $L = 20$ - 500 nm, simulated. 3D simulations are computationally expensive, produce large outputs and take a lot of time to run. However, test 3D simulations were performed and verify that the channel and jet are also observed [126].

From the plots in figure 5.19, a high density central component is observed in the $L = 20$ and 40 nm targets, which is similar to the observation reported in Powell *et al* [126]. Comparing the proton profiles from the 3D simulation with the experimental data Powell *et al* found good agreement, including an enhancement on one side of the annular structure in the proton beam when irradiating at θ_L =30°.

Figure 5.19 shows the protons over the full energy spectrum in the simulation, whereas experimentally we observe the annular structure only in the low energy component. Thus protons with energy in the lower quartile of the simulation are

considered for comparison to the experimental results, as shown in figure 5.20. Here the final simulation time-step is presented for $L = 40$ and 500 nm with the lower energy quartile of the proton population in green. As the radiation pressure-driven Al^{11+} ion layer expands into the rear of the proton layer, the electrostatic field formed at the interface between the two species deflects the slowest protons towards the direction of the local normal to the Al^{11+} expansion profile. This imparts transverse momentum to the low energy protons, which continue to expand radially after the laser intensity decreases after the peak of the pulse. This behaviour can be observed in figure 5.20(a) and (b) for an $L = 500$ nm target, which does not become relativistically transparent to the laser. Figure 5.20(b) shows the angular distribution of the beam of accelerated protons as a function of time. For $t <$ -300 fs (rising edge of the pulse), TNSA dominates and there is a divergent beam with no observed splitting. At approximately $t =$ -300 fs the radiation pressure is sufficient that the expansion of the Al ions starts pushing the low energy protons to larger angles. The width of the resulting annular profile, $\Delta\theta$ (effectively the ring diameter), increases throughout the remainder of the interaction.

For a sufficiently thin target, heating and expansion of the electron population will result in it becoming relativistically transparent during the laser pulse interaction. As an example, figures 5.20(c) and (d) show the case for $L = 40$ nm, for which RIT occurs at $t = 20$ fs (marked with the dashed line). As with the thicker target, the relatively low energy proton beam component starts to undergo radial deflection at approximately $t =$ -300 fs. However, the overall rate of increase in $\Delta\theta$ is larger due to the increased expansion velocity of the Al ions. Thus, the diameter of the final proton ring depends on whether RIT occurs and, as will be shown below, on when it occurs with respect to the peak of the laser pulse profile.

The opening angle of the ring is investigated as a function of proton energy and

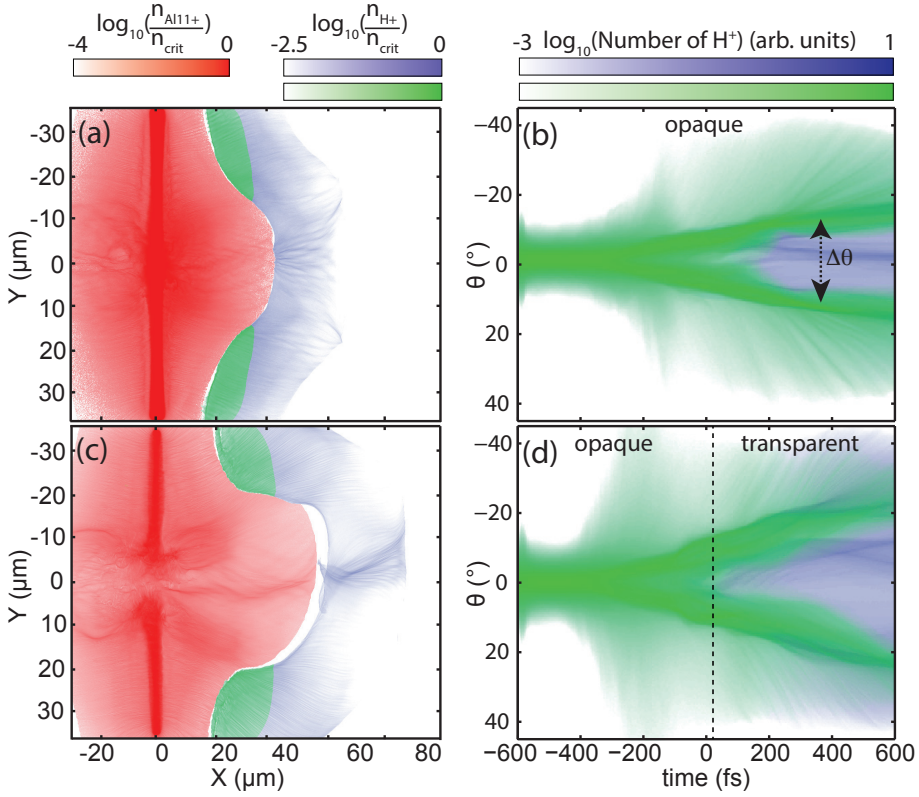

Figure 5.20: Example simulation results showing: (a) Ion densities for an $L = 500$ nm target at $t = 700$ fs: Red indicates Al^{11} ions; Green indicates protons with energy in the lower quartile; Blue represents the remainder, higher energy protons. (b) Angular profile of the protons accelerated from the $L = 500$ nm target as a function of time with respect to the peak of the pulse ($t = 0$). (c) and (d) Same for $L = 40$ nm, for which relativistic transparency occurs at $t = 20$ fs marked with the dashed line and the scales are the same.

target thickness in the simulations and the results are shown in figure 5.21 and 5.22. $\Delta\theta$ increases with E_prot for $L = 20$ and 40 nm, whilst for $L = 100$ nm it changes very little as can be seen in figure 5.21.

If we consider the percentage of transmitted light for each of these targets (figure 5.18), $L = 20$ and 40 nm undergo transparency earlier than $L = 100$ nm. The largest $\Delta\theta$ is found to be at $L = 40$ nm for both laser polarisations as shown in figure 5.22. The overall dependence of $\Delta\theta$ on L is similar for both linear and circular polarisation, with $\Delta\theta$ for the $L = 40$ and 100 nm much lower for the

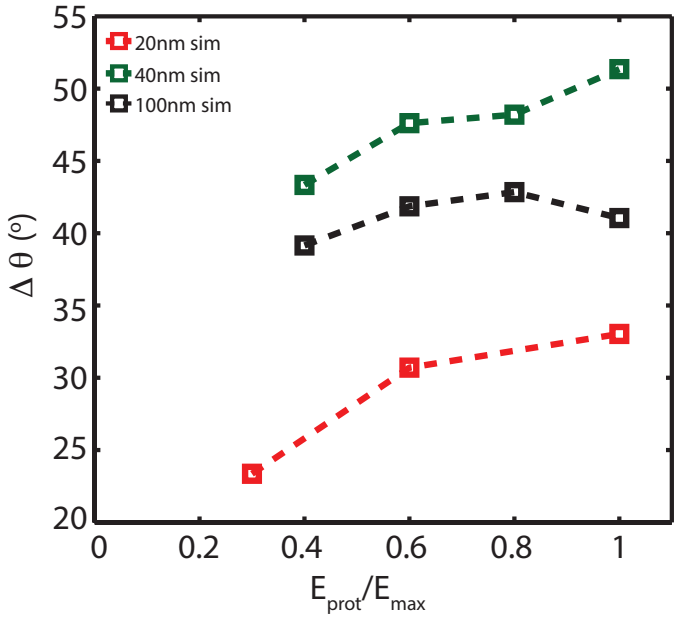

Figure 5.21: Divergence angle $\Delta\theta$ as a function of normalised proton (E_{prot}/E_{max}), energy of the lower quartile from the simulation results for L = 20, 40 and 100 nm.

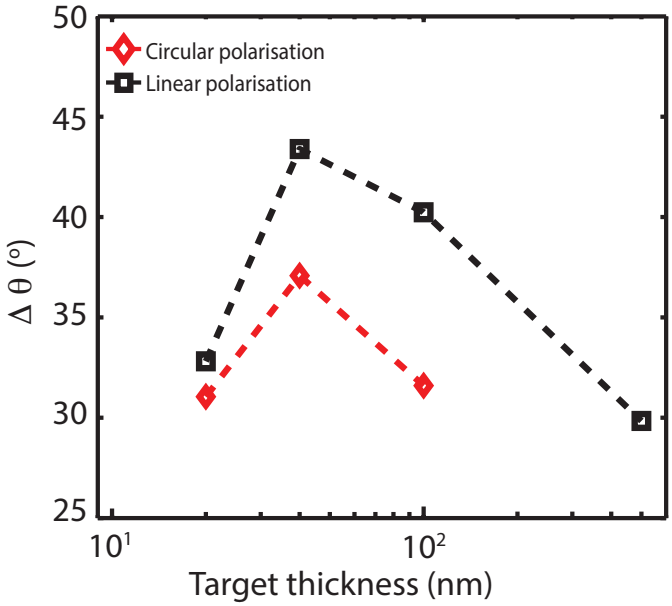

Figure 5.22: $\Delta\theta$ as a function of target thickness L for P- (black) and C- (red) polarised laser light from the simulation results integrated over the lower quartile of the proton energy range.

circular case. This is caused by enhanced heating and therefore expansion of the target when using linear polarisation. For L = 20 nm, $\Delta\theta$ for both cases is comparable. However, for linear polarisation, $\Delta\theta$ is slightly larger than for the

circular case, due to the increased expansion of the front surface. The lowest $\Delta\theta$ is observed for the $L = 500$ nm target, as transparency does not occur at this thickness.

In the simulation results we have observed a two dimensional annular structure in the proton beam and made measurements of how the beam opening angle changes with E_{prot} and L. The transmitted laser light also shows that the degree of transparency decreases as the target thickness increases. Below the underlying physics of how the annular structure appears in the proton beam will be discussed, along with a comparison of experimental and simulation results.

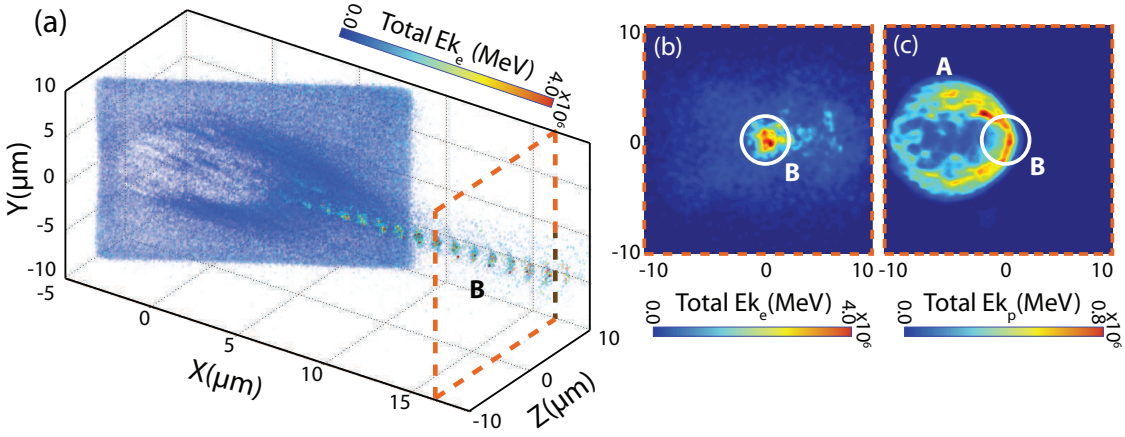

Figure 5.23: 3D PIC simulation (a) showing an example 3D plot of the total energy sampled at 400 fs. Label B corresponds to the electrons which show an energy enhancement as they are directly accelerated by the laser resulting in a jet modulated by the laser frequency. (b) Total electron energy in the 2D plane at $x = 16$ μm, marked in (a). (c) Total proton energy in the 2D plane at $x = 16$ μm. The feature labelled **A** corresponds to the annular component of the proton beam expanding off-axis from the laser propagation. **B** represents the region of enhancement from the energetic electrons accelerated by the laser and forming the jet.

Some 3D simulations have been carried out to check that the plasma ring and jet are not a product of the 2D simulation geometry [126]. 3D PIC simulations are much more computationally demanding than 2D, which constrained the size of the simulation box and resolution used. The dimensions of the 3D simulation box were 60 μm $\times$ 20 μm $\times$ 20 μm, using 3000 $\times$ 360 $\times$ 360 cells, in the x,

y and z directions respectively. To compensate for the reduced dimensions and resolution, the 20 nm Al^{11+} target was expanded to a Gaussian profile with a peak density of $5n_{crit}$ and the electrons were given an initial temperature of 10 keV. The contamination layer were given a similar profile with the H^+ population expanded to give a peak density of $5n_{crit}$. Expanding the target and decreasing the densities, ensures that the areal density is conserved. It should also be noted that the target was initialised at an angle of 30° with respect to the laser axis. The laser pulse had a duration of 200 fs and a peak intensity of 2×10^{20} Wcm^{-2}. The initial purpose of this was to investigate the laser rising edge on the plasma jet formation, see Powell *et al* [126].

The simulations performed show the formation of a plasma jet and acceleration of the electrons by the laser field. At $t = 400$ fs this can be seen in the electron kinetic energy plot shown in figure 5.23(a). A clear coupling of laser into the electrons can been seen with the electrons gaining a maximum energy within the region of the channel. Figure 5.23(b) shows a 2D slice in the Y-Z plane of the 3D simulation at $x = 16$ μm, which is marked with a dashed box in figure 5.23(a). Figure 5.23(b) displays the spatial energy distribution of electrons and shows a clear energy enhancement close to laser axis. In the same plane the 2D energy distribution of the protons is also sampled and is shown in figure 5.23(c). A clear annular profile can be seen in the proton distribution, labelled A. The component labelled B is due to the energy enhancement from the electrons in the jet.

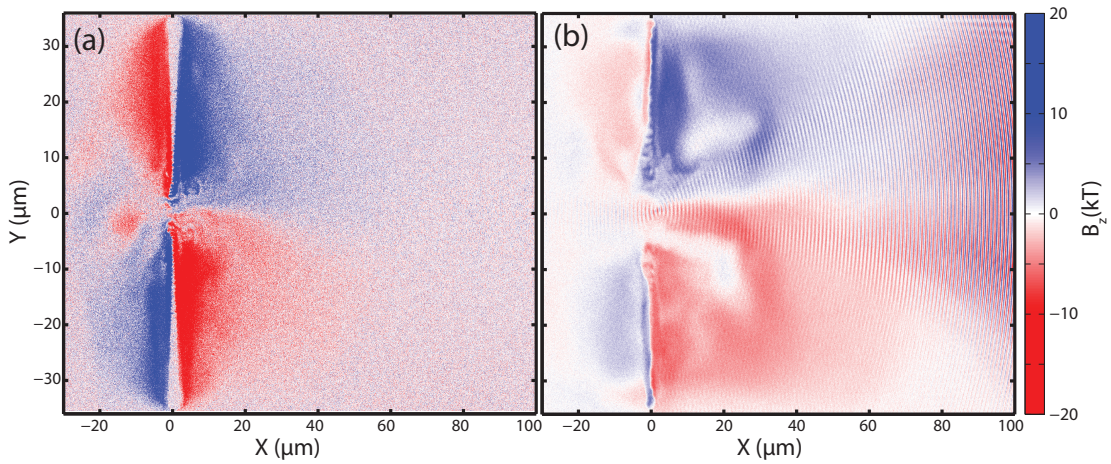

Figure 5.24: 2D PIC simulation results showing the azimuthal (B_z) magnetic field generated at the rear of the target of thickness (a) $L = 500$ nm and (b) $L = 40$ nm.

To explore the jet formation further, the B_Z field from 2D simulations was plotted for target of $L = 500$ and 40 nm, respectively, in figure 5.24(a) and (b). The magnetic field acts to contain the electrons and the additional electron heating drives the electric fields into the expanding ion layers, boosting their energies in the region of the jet. The magnetic field and channelling is similar to that observed in relativistic laser pulse propagation in other types of near-critical density plasmas [175, 177, 178]. The electrons are accelerated along the laser axis to form the jet. These electrons set up a self-generated azimuthal magnetic field that sustains the jet over an extended distance. As shown in figure 5.24, the magnetic field for the $L = 500$ nm and 40 nm targets are different. The field for the $L = 40$ nm simulation extends further from the rear surface of the target due to RIT.

5.4 Comparison of experiment and simulation results

The spatial-intensity profile of the proton beam exhibits distinct features which can be seen in both the experimental and PIC simulations results. It is clear that there are several different ion acceleration mechanisms occurring as the laser-foil interaction evolves, which can be observed in the time-integrated beam profiles in the RCF. To summarise, the observed spatial features are: a high dose, low energy annular structure that is observed in targets from $L = 10$-200 nm (feature A), and a laser-axis collimated proton beam (feature B). Bubble-like features believed to be the result of Rayleigh Taylor-like instabilities are also observed experimentally in targets with $L = 10$-40 nm.

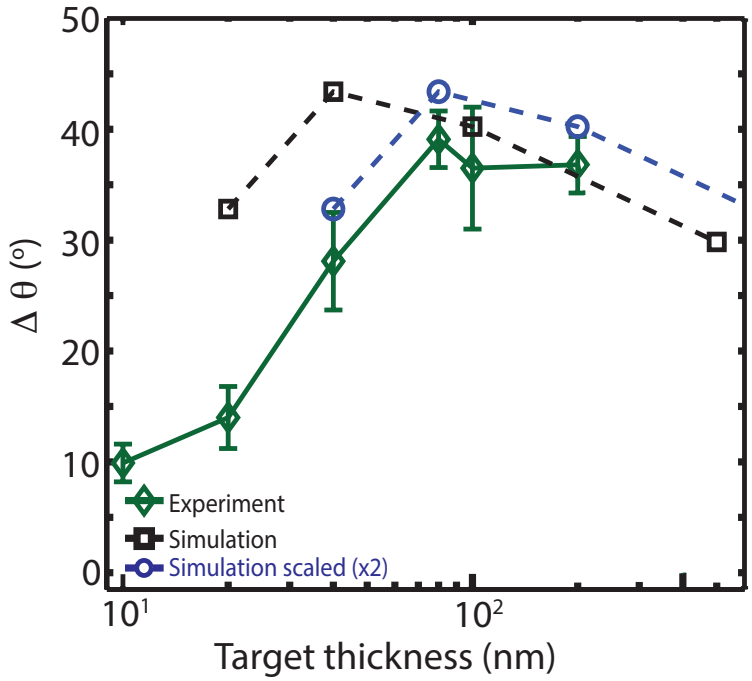

Figure 5.25: Comparison of experiment and simulation results for $\Delta\theta$ as a function of L, for low energy protons ($E_{prot} = 2.7$ MeV in the experiment and integrated over the lower quartile of the proton energy range in the simulations). The simulation results scaled up by a factor of two in target thickness (as determined by the difference in L_{opt}) is also shown.

In the present study, as observed in figure 5.25, both the experiment and simulation results exhibit an optimal target thickness, L_{opt}, which produces the largest opening angle in the low-energy proton ring. The difference in the absolute value (L_{opt} = 80 nm in the experiment and 40 nm in the simulations) is attributed to the idealized parameters and 2D dimensionality of the simulations.

When the target thickness in the simulation results is scaled up by a factor of two to take account of this, good agreement is observed with the experimental trends over most of the thickness range. For $L \geq 400$ nm the simulations continue to show a transverse deflection of the lowest energy protons, whereas the ring is not observed experimentally. It should be noted though, that the maximum measured proton energy decreases with increasing L, and as the ring is only produced in the low energy proton population, it is possible that it exists at energies below the lower detection threshold (equal to 2 MeV) of the RCF stack. Otherwise, the overall measured scaling of the ring size with target thickness is similar to that predicted in the simulations.

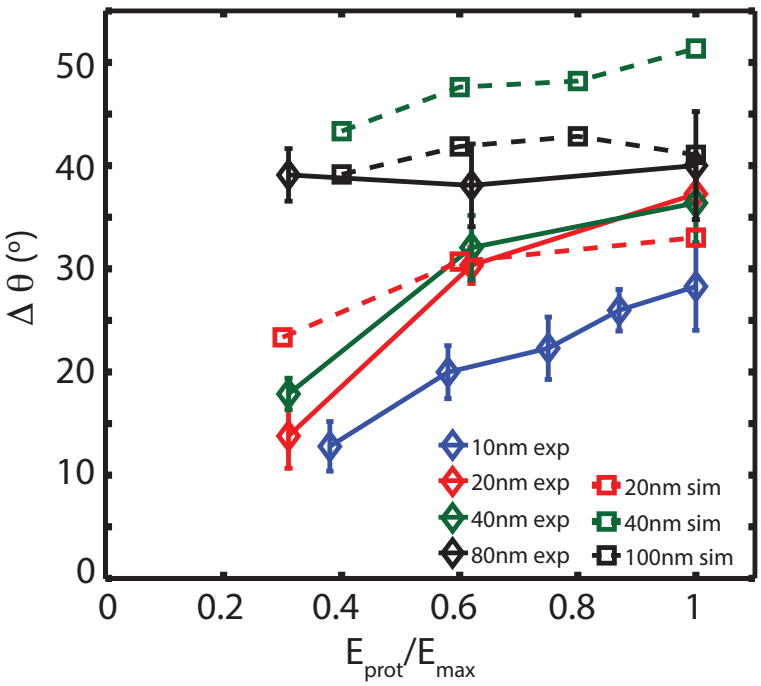

Figure 5.26: Comparison of experiment and simulation results of $\Delta\theta$ as a function of normalized proton energy for given L.

Figure 5.26 shows $\Delta\theta$ as a function of E_{prot}, normalized to the maximum proton energy (E_{max}) of the detected annular component. This is shown experimentally for L = 10-80 nm and compared with the simulations for L = 20-100 nm. The energy dependence of $\Delta\theta$ follows a similar trend in both cases. For $L<L_{opt}$, the increase in $\Delta\theta$ with E_{prot} is much greater than for $L\geq L_{opt}$, which further highlights the change in behaviour when $L = L_{opt}$.

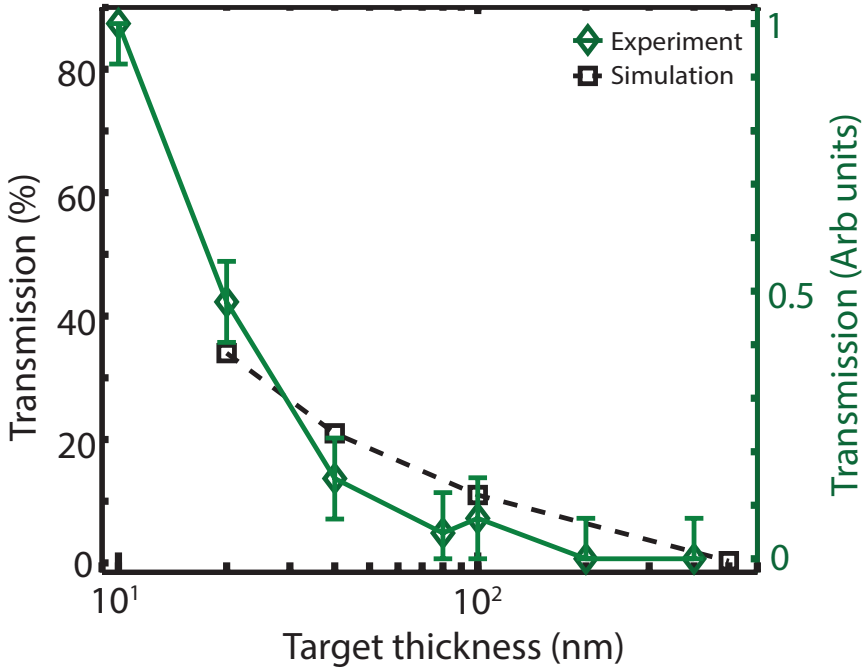

Figure 5.27: Comparison of experiment and simulation results of transmission through the foil as a function of L.

Figure 5.27 compares the transmitted light as a function of L, as measured experimentally and from the simulation results. The percentage of laser light transmitted is observed to decrease with increasing L, as expected. For $L\geq L_{opt}$ (where $\Delta\theta$ varies little with proton energy), the percentage of transmitted light is low. Transmission increases rapidly with decreasing L for $L<L_{opt}$. Thus the onset of RIT is shown to change the ion expansion dynamics, and specifically the proton ring diameter and its variation with proton energy.

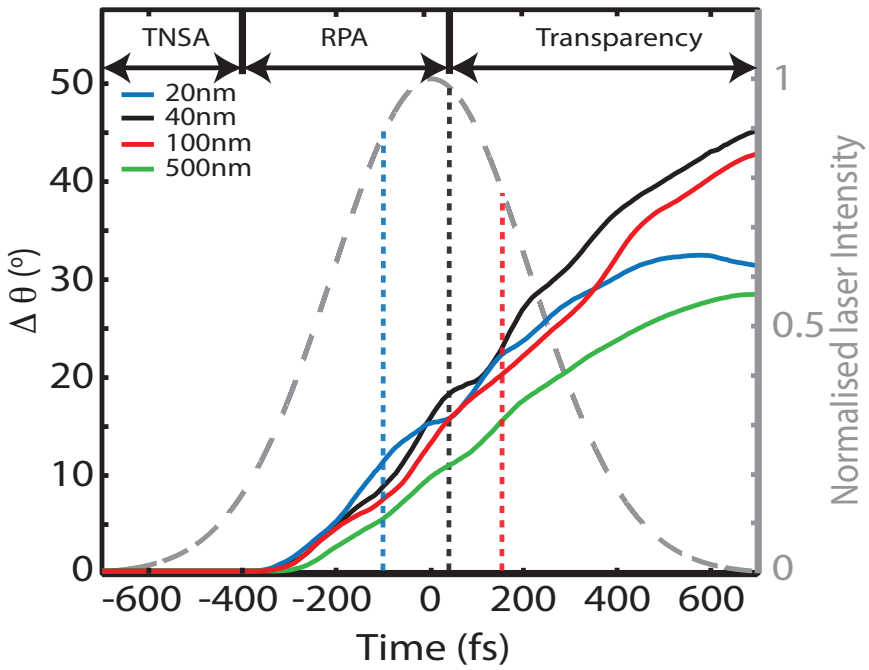

Figure 5.28: Simulation results showing the temporal behaviour of the average ring opening angle for different target thicknesses. The temporal profile of the laser intensity is also shown. Dashed vertical lines are added to indicate the onset of transparency for the corresponding target thickness. Note that the L = 500 nm target does not undergo transparency. The dominant intrapulse acceleration mechanisms are labelled at the top of the figure for the L = 40 nm example case.

In figure 5.28 the temporal evolution of $\Delta\theta$ is shown for L in the range of 20-500 nm, along with the idealised temporal profile of the laser intensity envelope arriving at the target. In all cases the proton beam splits at around t = -300 fs, occurring slightly earlier for small L and later for large L. As the intensity continues to increase, $\Delta\theta$ increases for all L, but the rate of change differs. The rate is generally higher for small L, within the RPA-dominated phase of the interaction. However, if RIT occurs early in the interaction then the final ring beam diameter is smaller than if it occurs near the peak of the laser profile as the structure has less time to develop. This is clearly observed in figure 5.28 when comparing the L = 20 nm and L = 40 nm cases (the dotted vertical line marks the time at which RIT occurs for each L from the simulation). A comparison

with the $L = 100$ nm case, for which RIT occurs on the falling edge of the laser pulse, shows that the largest ring is obtained when RIT occurs near the peak of the laser intensity, where the hole-boring velocity is highest.

5.5 Conclusion

In conclusion, the experimental results show distinct features in the spatial-intensity profile of the proton beam, such as rings, bubbles and regions of energy enhancement. The analysis of the angular emission of the low energy component of the accelerated proton beam provides new insight into ultra-thin Al target dynamics during ion acceleration.

Through PIC simulations using the EPOCH code it was demonstrated that multiple ion acceleration mechanism can occur over the duration of the interaction. During the initial interaction, the TNSA mechanism dominates. As the intensity increases on the rising edge of the laser pulse, hole-boring becomes the dominant mechanism driving bulk ions into the rear of the TNSA accelerated protons. The slow protons are driven radially by the bulk ions, resulting in a low energy annular profile in the proton beam. At some point during the interaction when the target peak electron density drops below the relativistically corrected critical density ($n_e < \gamma n_{crit}$) the target becomes transparent resulting in the laser pulse propagating through it. This will result in transparency enhanced acceleration where electrons are volumetrically heated by the laser pulse. It also results in the generation of a jet and direct electron acceleration in the case of sufficiently expanded plasma. Laser-driven ion acceleration is thus shown to be a complex process where multiple mechanisms can occur when an intense laser pulse irradiates an ultra-thin foil, with the dominant acceleration mechanism changing over the course of the interaction.

Understanding the dynamics of laser-foil interactions is highly important to

the development of ion acceleration. Monitoring how the annular low energy components vary as a function of target thickness enables insight into the transition between RPA and transparency enhanced acceleration mechanisms. This approach to investigating various mechanisms can be combined with measurements of the transmitted light to determine when in the interaction the target becomes transparent. This enables the onset of transparency and its effect on ion acceleration in ultra-thin foils to be investigated.

Chapter 6

Laser contrast effects on proton energies in the transparency regime

In the previous chapter the intra-pulse transition between ion acceleration mechanisms was investigated by examining the spatial profile of the proton beam. As the laser pulse is the driver of the acceleration of ions, the laser intensity contrast is an extremely important parameter. In this chapter, an experimental and numerical investigation focusing on the key role that the rising edge of the laser pulse plays in the acceleration of ions from ultra-thin foils and how variation of the temporal width of the pulse affects proton energies, is reported.

Focused high power lasers pulses typically have a Gaussian spatial and temporal intensity profiles. Ultra-thin, nanometre foils are sensitive to the rising edge of the pulse and undergo expansion over a longer period than the FHWM pulse duration resulting in the peak density decreasing. This influences the interaction dynamics, for example, RIT will take place earlier if the expanded targets electron density drops below the critical density on the rising edge of the pulse. In this chapter, the maximum proton energy is shown to be sensitive to the pulse temporal width

at 1% from the peak of the laser pulse. It is also found that the rising edge of the pulse at this level affects the intra-pulse transition between ion acceleration mechanisms.

Laser rising edge effects on targets at the picosecond time scale have been investigated by Schollmeier *et al* [179]. In their study, it was inferred from simulations that the ps-scale rising edge of the main pulse can alter the target expansion and generate relativistic electrons earlier at low intensities. However, their study investigated the effects on micron-thick targets, where the main acceleration mechanism is dominated by TNSA. Here we investigate laser contrast effects on ultra-thin nanometre targets. A similar study using nanometre-scale targets was carried out by Powell *et al* [126], where they induced a controlled pre-pulse before the peak of the pulse. Numerically, they inferred that maximum proton energy could be achieved in the single pulse case. In this chapter, the contrast of a single pulse laser and the resultant proton energies are investigated.

6.1 Experimental Set-up

The Vulcan Petawatt laser was used for this study, with a similar experimental set up to that described in chapter 5. A laser pulse of energy equal to $E_L = (200 \pm 25)$ J on target with a pulse duration of $t = (1 \pm 0.2)$ ps at FWHM was used. The p-polarised laser pulse was preceded by a 1 - 2 ns pedestal with an intensity contrast ratio of 10^8. The contrast was improved to 10^{10} using a single plasma mirror. An off-axis f/3 parabolic mirror focused the beam to a (8 ± 2) μm FWHM spot diameter resulting in a calculated peak intensity of $I_L \approx 2 \times 10^{20}$ W/cm^2. The laser pulse was focused onto Parylene (C_8H_8) targets, which were angled at 25° to the laser axis, enabling the proton beam components to be separated along target normal (TNSA) and laser axes (RPA) [126]. The target thickness, L, was fixed at 100 nm.

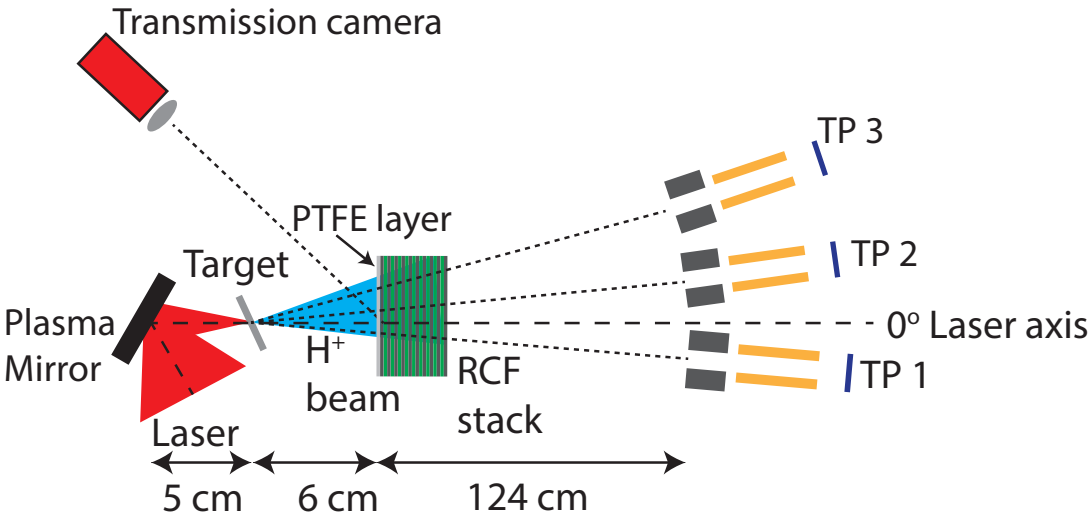

Figure 6.1: Schematic of the experimental set-up. The focusing laser pulse is reflected off a plasma mirror to increase contrast, then focused onto a nanometre thick target. The main diagnostics are a radiochromic film stack (RCF) with a PTFE layer (for transmitted laser light) and three Thomson parabola spectrometers, to measure the spatial and spectral profiles of the proton beam, respectively.

The main diagnostics used on the experiment were a RCF stack, three Thomson parabola spectrometers at angles -5.1°, 8.6°, 22.6° with respect to laser axis, and a thin PTFE scatter screen positioned at the front of the RCF stack to measure the transmitted light. The amount of laser light transmitted through the target was measured for the fundamental harmonic. The fluorescence on the scatter screen generated by the transmitted laser light, was imaged using a CCD camera. The transmitted light on the PTFE screen is calibrated using the laser pulse without a target in place. The images taken in this shot is used as a reference, enabling conversion of the images taken during normal shots, into laser energy transmitted through the target.

The RCF stack was placed 6 cm from the target rear with a horizontal slot cut through the centre to provide a line-of-sight to the Thomson parabola (TP) spectrometers. A 2D spatial-intensity distribution of discrete proton energy bands ranging from 2.7 to 70 MeV was measured using the RCF stack with dimensions

of 6.5 cm × 5.0 cm. As the target was angled at 25°, the different components of the proton beam, produced by the various acceleration mechanisms could be separated.

Thomson spectrometer details			
Parameter	TP 1	TP 2	TP 3
Angle (°)	-5.1	8.6	22.6
Distance from TCC (cm)	117	133	56
Pinhole diameter (μm)	200	200	100
Solid angle (nSr)	22.9	17.7	25.0

Table 6.1: Configuration of the three Thomson parabola spectrometers used.

Three Thomson parabola spectrometers were utilised in the experiment. Each spectrometer consisted of a 0.95 T, 50 mm long magnet and electric field plates which were 150 mm long, with the potential difference across the plates set to 24 kV, producing a field with magnitude equal to 4.8 MV/m (with a separation of 5 mm between the electric field plates). Details of each spectrometer are given in table 6.1.

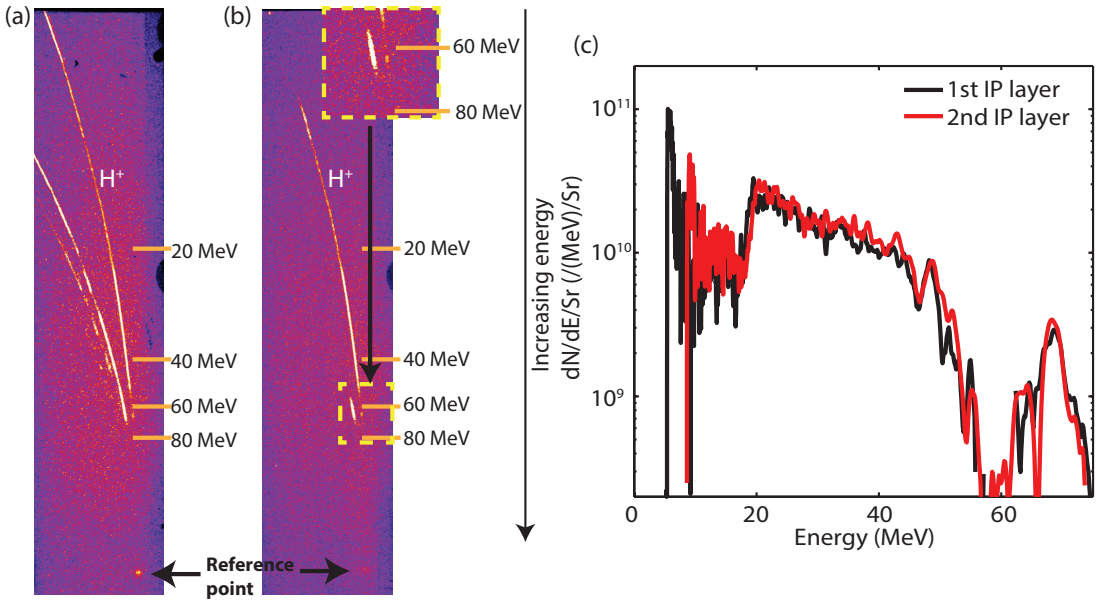

Figure 6.2: (a-b) Raw scans of the Thomson spectrometer image plates for the same shot showing (a) 1st layer and (b) 2nd layer. (c) Proton spectra extracted from (a) and (b) with the 1st layer in black and 2nd layer in red.

The ion spectra were measured using standard TR image plate, which has no protective layer in front of the active phosphorous layer. Two layers of image plate were placed together to measure high energy protons [171]; Due to their high charge-to-mass ratio and large cross section the energetic protons will continue to pass through the first layer of IP onto the second layer. Figure 6.2 (a) and (b) display the example raw traces obtained from TP 1 with the spectra extracted from these traces shown in figure 6.2 (c). The proton spectra extracted from each image plate show a good agreement with each other, although the low energy, < 10 MeV component on the 2nd layer is not observed, due to the low energy protons being stopped in the first layer of image plate.

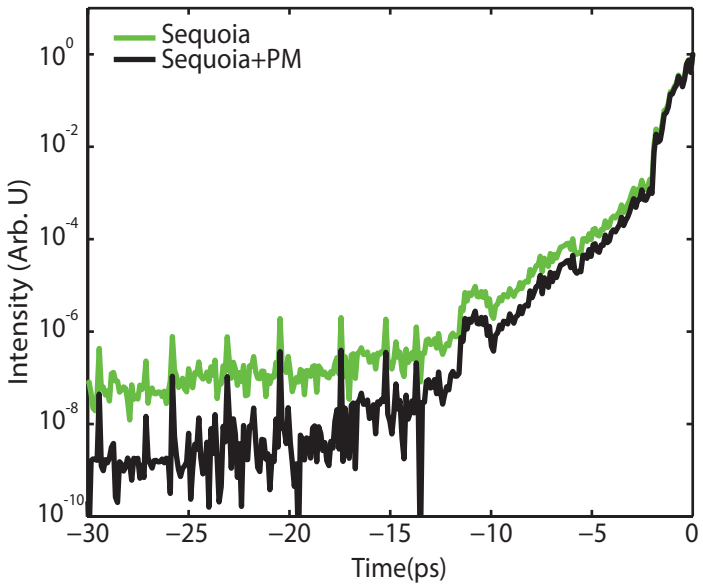

Figure 6.3: Third order scanning cross-correlator (Sequoia) contrast measurement of the ps OPCPA pre-amplification stages (green) and the contrast enhancement due to the plasma mirror (black).

The contrast measurement of the TAP laser pulse is made up of the combined ps and ns OPCPA pre-amplifiers, stretcher and compressor. In order to examine the contrast in the initial stretcher stage, the amplifier chain is bypassed and the pulse is relayed from the front end directly to the compressor chamber, giving

a high repetition rate [153]. This allows the front end of the OPCPA, and the stretcher and compressor system, to be characterized using a third-order cross correlator (Sequoia). An example of the measurements ∼30 ps prior to the peak of the pulse is shown in figure 6.3. The enhancement in contrast calculated using plasma mirror reflectivity measurements [180], is plotted along with the initial Sequoia measurement.

Although it is useful having contrast measurements before the experiment, a shot-to-shot measurement of the contrast is required. It is impossible to have a highly resolved temporal profile using present day diagnostics due to the pulse duration being in the sub-picosecond to femotosecond range. However, a single shot autocorrelator can provide a typical measurement of the pulse width. On TAP there are a range of laser diagnostics, one particular diagnostic to measure the laser pulse duration is the near field single shot autocorrelator and is used to measure the sub-aperture of the leakage taken from the laser pulse before it enters the interaction chamber [167]. The autocorrelator trace is calculated by taking line outs across the near field image.

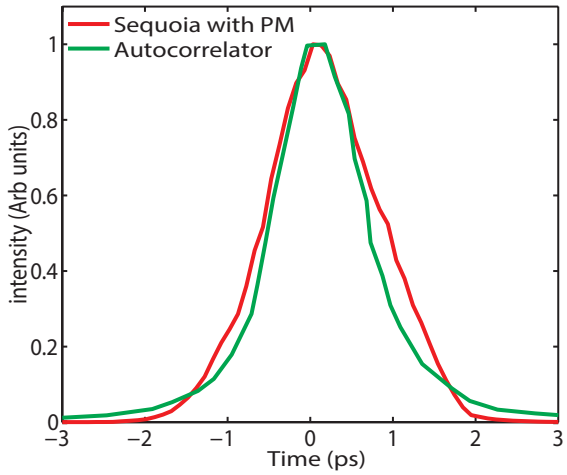

Figure 6.4: (a) Example of the autocorrelator trace (green) with the Sequoia trace (red)

Figure 6.4 displays an example of the autocorrelator measurement with the

third order cross correlator (Sequoia) trace from figure 6.3. The on-shot near field autocorrelator in TAP is employed to investigate how sensitive ultra-thin foils are to the laser contrast and how the resultant proton energy is affected by the rising edge of the laser pulse.

6.2 Experimental results

In order to investigate laser-driven ion energy scaling, the most common approach is to measure the high energy cut-off or the maximum energy of the ion spectra. By irradiating a 100 nm CH target with a linearly polarised laser pulse, a maximum proton energy of 68 MeV was obtained. The corresponding beam spatial-intensity profile in the RCF is displayed in figure 6.5 (a). Figure 6.5 (b) displays the raw image plate for the three TPs and the spectra obtained from the RCF, TP 1, TP, 2 and TP 3 are shown in figure 6.5 (c). The spectra shown in figure 6.5 corresponds to the same shot as shown in figure 6.2.

By angling the target with respect to the laser axis, the individual components could be spatially separated, otherwise they would be expected to overlap at normal incidence [126]. The overlapping of the individual components of the proton beam was discussed in chapter 5. By irradiating the target at an angle, the centre of the annular structure is shown to be directed along target normal ($\sim$20°). Along laser axis, between 0° and 10°, an enhanced component of the proton beam can be observed (for all laser shots). The dosimetry film in the stack was used to detect protons up to 55.3 MeV and the final layers were made up of image plate, detecting energies up to 68 MeV. Extracting the proton data from the image plate first required removing the electron signal. This is done by subtracting the final layer of image plate from the first two layers to remove the electron signal and background. This accounts for the white areas seen on the detector in figure 6.5 (a). This enable a clear differentiation between the proton

and electron signal.

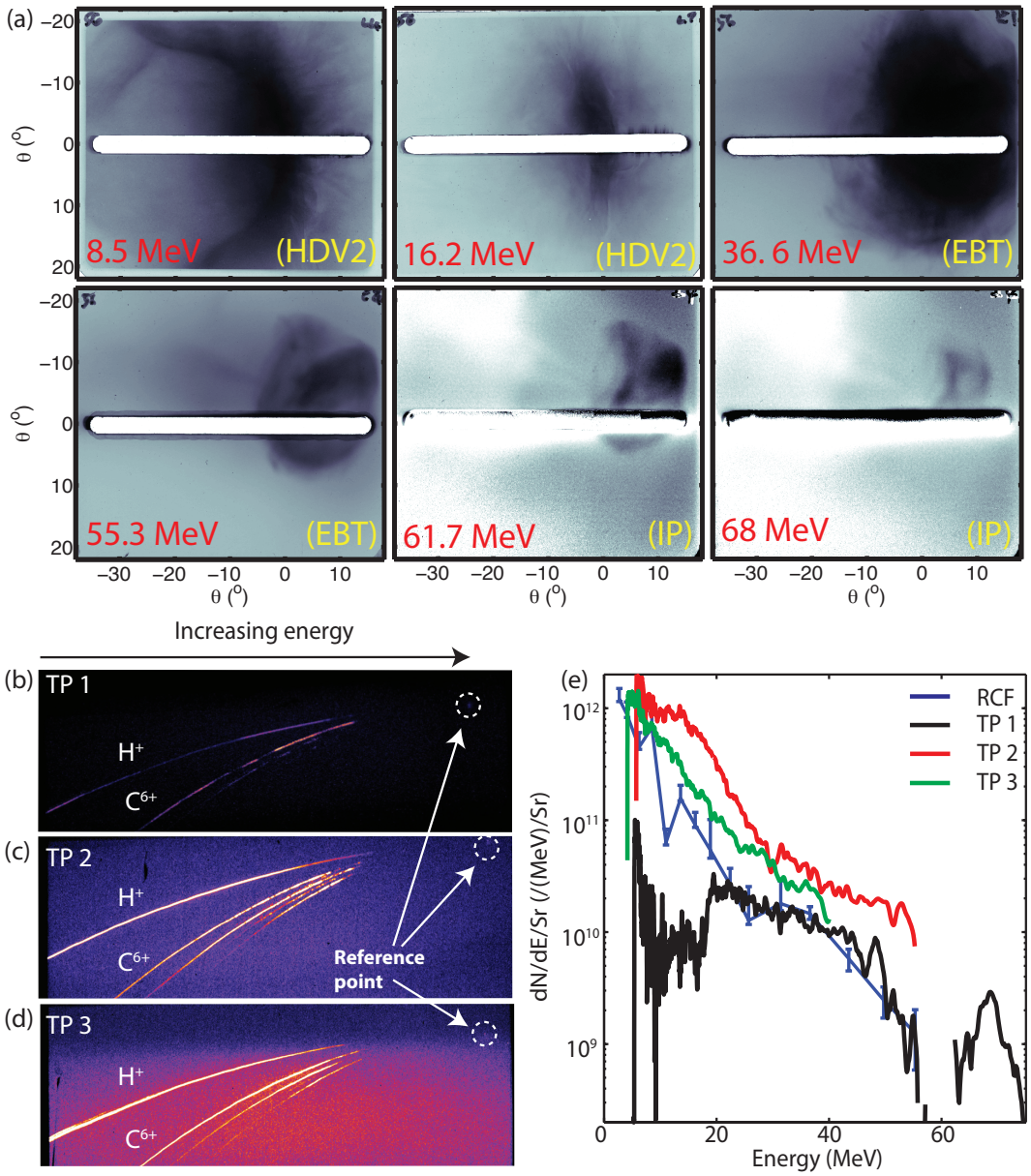

Figure 6.5: (a) Spatial-intensity profile of the proton beam in the RCF stack and image plate at given energies, (b-d) displays the raw image plate data as measured in the dispersion plane of the TP (e) the spectra from the RCF and TPs.

The ion traces obtained from the three TPs, used to measure the energy spectrum of the proton beams are shown in figure 6.5 (b-d). The contrast of all three images was kept the same to show the difference in flux of the protons in each TP. Figure 6.5 (e) displays the extracted spectra from the three TPs and the RCF. Overall the spectrum from all 4 diagnostics follows a TNSA-like distribution. However, TP 1 shows a break in the spectrum with a peak at 68 MeV. This feature could not be included in the RCF spectra, as the image plate in the stack at this energy is not calibrated to give the proton flux. In order to calibrate the image plate, a well characterised beam from an accelerator is required to do a number of scans of energy deposition and flux as described in chapter 4. Also, at low energies the measured spectrum from TP 1 is close to an order of magnitude lower in flux compared to the other two TP detectors, as shown in figure 6.5 (e). As the laser pulse is linearly polarised, the target will undergo expansion, with TNSA the dominant acceleration mechanism in the early stages of the interaction. This will result in a large population of rear surface protons being accelerated in the target normal direction. As the intensity of the laser pulse increases, a transition takes place where the hole boring mechanism dominates. This results in a small population of protons being accelerated along the laser axis direction. The low proton flux observed from TP 1 is seen in all shots.

In studies prior to this, the highest proton energy detected using the Vulcan petawatt laser was 55 MeV, reported by Robson et al [181]. On this experimental campaign, energies of 68 MeV were observed by irradiating a 100 nm CH target as shown in figure 6.6. However, in the past year, even higher energies of 85 MeV have been reported [21] using similar low density plastic targets and a similar laser system. Figure 6.6(a) displays the peak proton energy cut-off from 100 nm targets for all three TPs; with TP 1 shown in red, TP 2 in black and TP 3 in blue. Multiple repeat shots were performed at this target thickness as this produced the highest proton energies. Figure 6.6 (a) shows this was not always the case

however, as a large variation in proton energies, between 20 and 68 MeV, was measured.

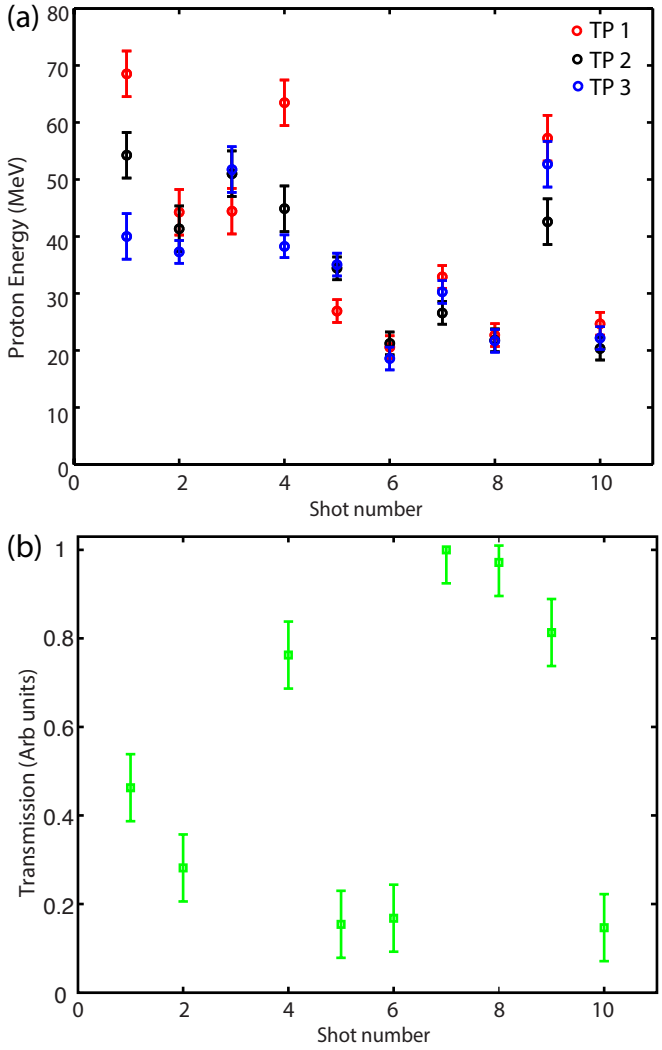

Figure 6.6: (a) represents the proton energy as a function of shot number for each TP and (b) shows the transmission of the laser pulse from a 100 nm CH target.

The corresponding laser light transmitted for each of these shots is displayed in figure 6.6(b). The transmission data is normalised to the maximum light transmitted through the 100 nm thick target. The targets used in this campaign are Parylene, which has a lower density (1.11 g/cm^3) than Al (2.7 g/cm^3) targets used in the experiment reported in chapter 5. The CH targets will undergo RIT a

lot earlier than an Al target of the same thickness. This is due to a large difference in areal density, a 10 nm CH target has an areal density of 1.11×10^{-6} g/cm^2 compared to 2.7×10^{-6} g/cm^2 for 10 nm Al. The 10 nm Al target can thus be more appropriately compared to a 25 nm Parylene target. From this point onwards, the focus of this chapter will be the proton energies measured using TP 1, in the laser axis direction.

The transmission from the 100 nm target also shows a variation, indicating that shot-to-shot the plasma dynamics are changing, giving rise to these irregularities.

One can observe that the maximum proton energy achievable is sensitive to the degree of transmitted light; indicating that, even though the target thickness is kept the same, the onset of transparency does not occur at the same time for each case. Therefore as the target thickness is fixed, the fluctuation could be due to the laser pulse energy or contrast for example. The laser energy for each of the shots presented was measured ($E_L = (200 \pm 25)$ J on target) and there was no correlation between the maximum proton energy and laser energy.

To further examine the sensitivity of the maximum proton energy and transmission, the contrast of the laser is investigated. As the on-shot temporal profile cannot be measured in the femotosecond regime, the second order autocorrelator traces is used to investigate the contrast. An example of three autocorrelator traces for pulses with the same laser energy are shown in figure 6.7 (a).

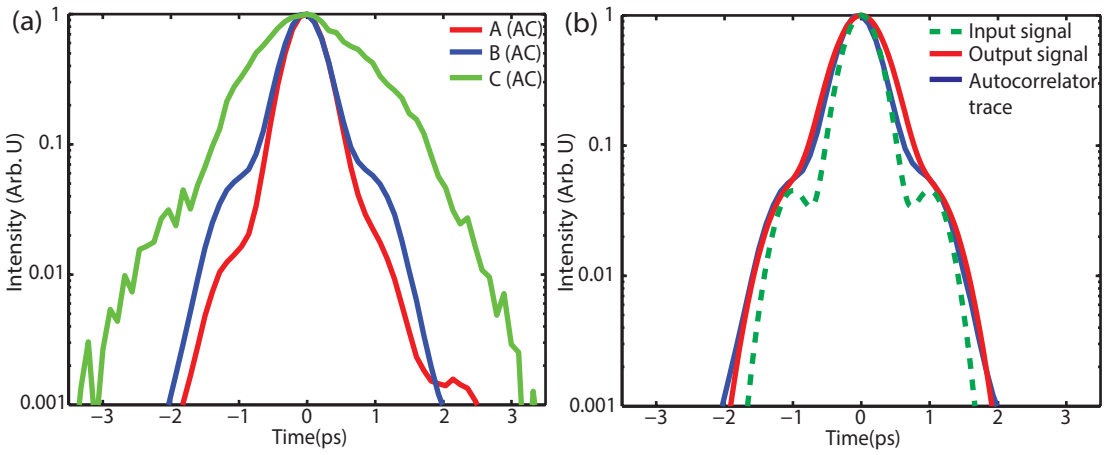

Figure 6.7: (a) Example of three autocorrelation traces and (b) modelled input and output of the autocorrelator pulse signals used to replicate the laser pulse profile at the target based on the autocorrelator trace.

Using the autocorrelator, the temporal width for each laser shot was observed to differ shot-to-shot as shown in figure 6.7 (a). The autocorrelator does not provide a measure of how intense the rising edge of the laser pulse is but it provides a measure of the temporal width of the pulse. For the three examples, the temporal duration of the pulse varies, with the shortest **A** (in red) and longest **C** (in green). In order to measure the temporal width of the laser pulse profile at the target, the rising edge of each case is modelled using an input pulse to give a similar output profile to the autocorrelator trace measured from the experiment. An example of this is shown in figure 6.7(b). As discussed in chapter 4, the final mirror in the Vulcan petawatt laser chain after the compressor directs the laser pulse into the interaction chamber. A small hole is cut in this mirror to sample a small portion of the laser pulse and is directed to the autocorrelator. The autocorrelator measurement made on the experiment is used to work backward to model the laser pulse on target, as illustrated in figure 6.8. The input pulse rising edge (2) and width is varied until the rising edge of the output pulse matches the autocorrelator trace (1).

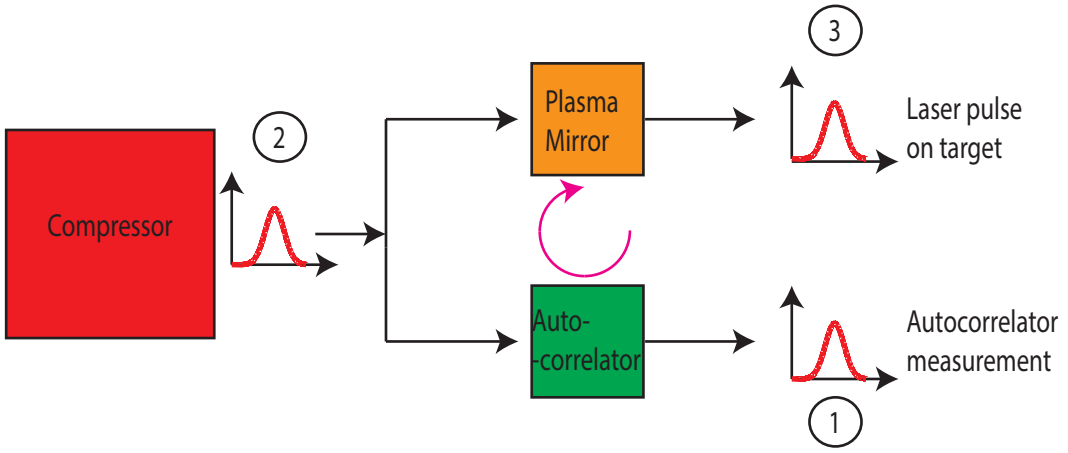

Figure 6.8: Schematic outlining the method used to model the laser pulse profile (2) and the laser pulse on target after the plasma mirror (3) using the Autocorrelator trace (1).

The resultant input signals modelled for the three autocorrelator traces is shown in figure 6.9 (a). The contrast enhancement achieved using the plasma mirror was calculated using reflectivity as a function of intensity measurements and used to model the pulse profile (3) on target [180]. The profile on target was modelled to show how the rising edge of the pulse varies after the plasma mirror as it removes the low level ASE and any pre-pulses. The modelled pulses on target are plotted in figure 6.9 (b). To compare the temporal profile of the pulse on target, the Sequoia trace is plotted alongside the modelled laser profiles. The Sequoia measurements represents the average pulse profile of the laser system and it is essential to compare the modelled pulses to the Sequoia.

The corresponding resultant proton spectra measurements, made using TP 1 from the three modelled pulses is shown in figure 6.10 with the same colour scheme used in figure 6.9.

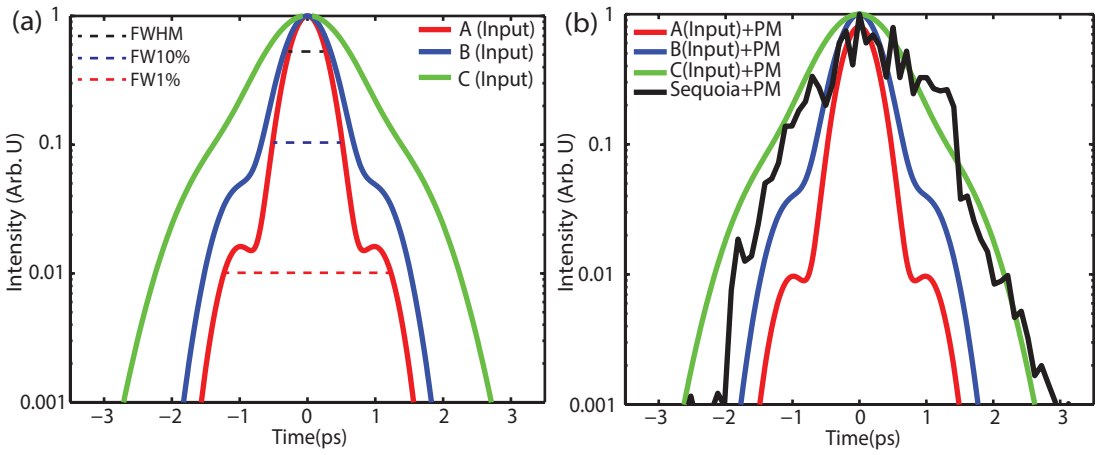

Figure 6.9: (a) Input signal of three laser pulse traces modelled before the plasma mirror and (b) the same traces used to model the laser pulse at the target with the plasma mirror reflectivity measurements and plotted alongside the Sequoia measurement.

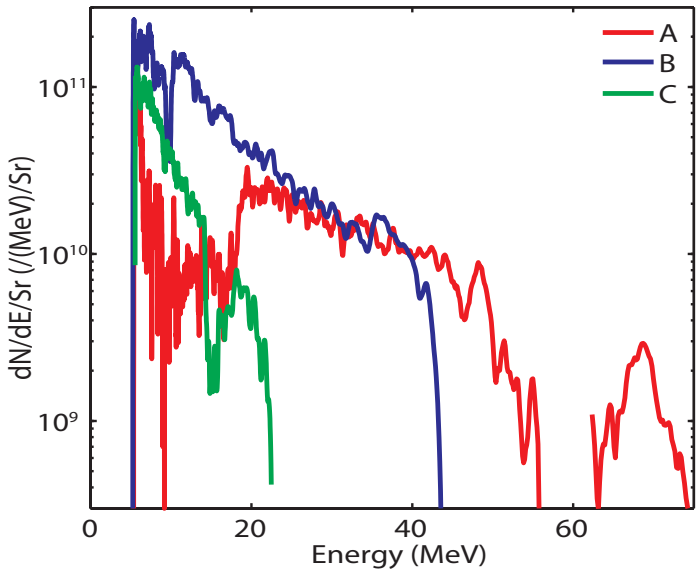

Figure 6.10: Proton spectrum measured using TP 1, corresponding to the pulses shown in figure 6.9.

The maximum proton energy is observed to correlate with the width of the laser pulse. The rising edge of the pulse induces ionisation and thus expansion of the target. The density gradient at the target front side affects the absorption, as discussed in chapter 2. The key point is that for each pulse, the rising edge can vary from shot-to-shot, which can significantly change the laser-plasma interaction physics, including maximum proton energies. The pulse labelled **A** has

a short temporal width in comparison to **B** and **C**, whereas the profile **C** has a slower rising edge (the intensity is higher at a given time relative to the peak). Case **A** produced proton energies of 68 MeV, whilst pulse **C**, only produced maximum energies of 24 MeV. To investigate how the laser rising edge affects the proton maximum energy, the duration of the pulses at three fixed intensities 50%, 10% and 1% of the peak intensity of the pulse is considered, as shown in figure 6.7(a).

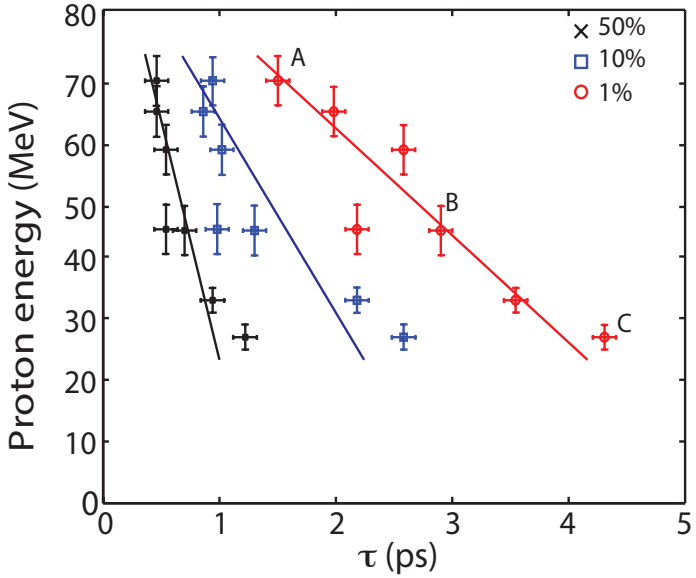

Figure 6.11: Experimental results showing the proton energy as a function of pulse duration at 50% (black), 10% (blue) and 1% (red) of the peak intensity.

Figure 6.11 shows the maximum proton energy plotted as a function of the duration at 50% (black), 10% (blue) and 1% (red) of the peak intensity of each modelled laser pulse. Considering firstly the 50% (FWHM), this parameter varies from ~ 0.5 to ~ 1.2 ps, showing that the temporal width increases as the resultant maximum proton energy decreases. Since the proton energy, for a given target thickness, shows a small correlation with the FHWM, two further pulse duration measurements were made at 10% and 1% of the peak intensity. A stronger correlation emerges between the maximum proton energy and the duration at the

1% level (where the intensity is $\sim 10^{18}$ W/cm^2). The pulse duration at 1% varies from $\sim$ 1.5 ps to $\sim$ 4.3 ps depending on the pulse profile, which can radically alter the expansion dynamics of the target.

6.3 Numerical PIC simulations

In order to understand how the rising edge of pulse affects the underlying physical mechanisms, 2D simulations were performed using the fully relativistic EPOCH PIC code [168]. The simulation box was defined as 195 μm $\times$ 69 μm using 39000 $\times$ 5760 simulation cells, with all simulation boundaries defined as free-space. The thickness of the target was fixed at $L = 100$ nm and was initialised as a 2D slab containing $60n_c$ C^{6+} and $60n_c$ H^+ resulting in $n_e = 420n_c$. The electron population was defined to neutralise all of the ions appropriately with an initial electron temperature of 10 keV. The target was angled at 30° to the laser axis to match the experimental conditions. The laser pulse was defined to have a Gaussian temporal profile with a FWHM of 400 fs and was focused to a transverse Gaussian profile with a 6 μm FWHM focal spot at the front of the target. The intensity was set to $2{\times}10^{20}$ Wcm^{-2}.

In order to vary the rising edge profile of the pulse, a secondary pulse (pre-pulse) was implemented to peak 600 fs before the main pulse. This is similar to the double pulsing method utilised by Powell *et al* [126]. The intensity of the pre-pulse was varied up to 16% with respect to the main pulse peak, with the intensity of the main pulse being reduced correspondingly such that the total energy of the laser pulse is conserved. By increasing the intensity of the rising edge, this will result in an increased temporal width at 10% and 1%. Therefore case **Z** has the largest temporal width at 1% from the peak of the pulse, whilst case **X** has the smallest. The different cases are colour coded, such that case **X**

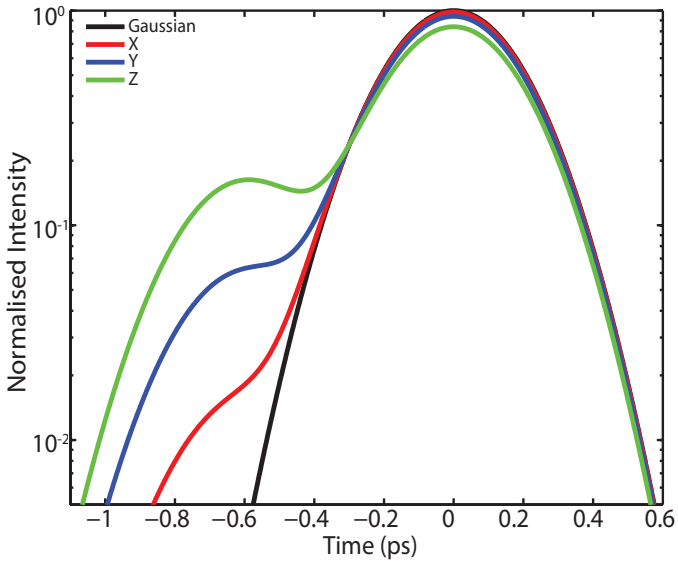

Figure 6.12: Example illustration of the laser pulse intensity profiles modelled in the simulation for the rising edge of the laser pulse. The duration of the pulse at the 1% level of the peak of the pulse is increased from 1.3 ps to 1.55 ps.

in red, case **Y** in blue and case **Z** is green. This colour scheme will be consistent throughout this section of this thesis. Both laser pulses are linearly polarised with a wavelength of $\lambda_L = 1.05$ μm. Examples of the laser pulses are displayed in figure 6.12, with an example Gaussian pulse in black, similar to the modelled pulses shown in the experiment section. To account for the laser propagation effects due to the expansion of the front surface [175], the target was positioned 30 μm from the incoming laser boundary.

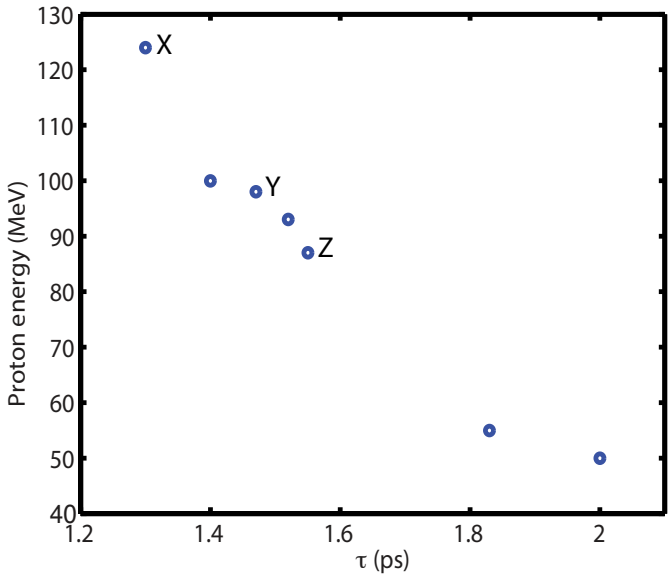

Figure 6.13: Simulation results showing the maximum proton energy as a function of pulse duration at the 1% level with the three main example cases labelled **X**, **Y** and **Z**.

The corresponding proton energy, from the final time step of the simulation, as a function of the temporal width of the laser pulse at 1% is plotted in figure 6.13. The three example cases, presented in figure 6.12, are labelled **X**, **Y** and **Z** in figure 6.13 with additional simulation results for varying τ plotted alongside them.

The simulation studies exhibit a similar trend to the experimental findings shown in figure 6.11, where the proton energy was measured to decrease as the width of the pulse increased at 1%. The case where the temporal width of the pulse at 1% is the shortest, corresponds to the maximum proton energies. It should noted that due to the dimensionality of the simulation the proton energies in 2D are exaggerated and are considerably higher compared to the experimental results. However, the general trends are similar. In order to increase τ beyond 1.6 ps in the simulations, the peak to peak separation of the two pulses was increased to 900 fs and 1100 fs in two simulations for a peak intensity 10% of the main pulse. These correspond to the two highest τ data points shown in figure 6.13.

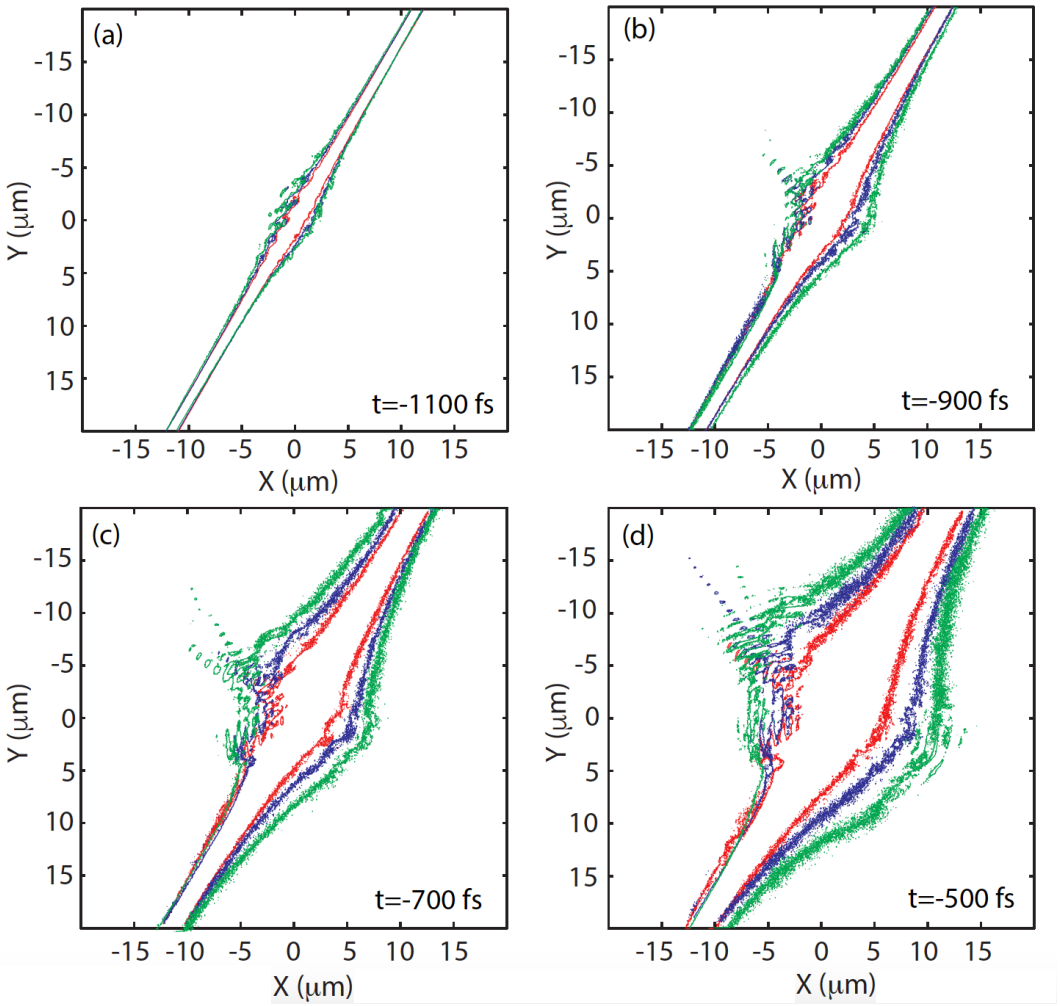

Figure 6.14: Simulation results show the electron density at $0.25n_{crit}$ for case **X** in red, **Y** in blue and **Z** in green at (a) t= -1100 fs (b) t= -900 fs (c) t= -700 fs and (d) t= -500 fs.

To understand the variation in proton energies due to the rising edge of the pulse, the expansion of target is investigated. A contour map of the electron density at $0.25n_{crit}$ is shown in figure 6.15 for (a) t = -1100 fs, (b) t = -900 fs, (c) t = -700 fs, and (d) t = -500 fs, prior to the interaction of the peak laser intensity for all three example rising edge profiles. This value of n_{crit} was used to quantify the pre-expansion of the plasma. It is shown in figure 6.15 that each of the cases expand at different rates, with case **Z** expanding far greater due to the longer rising edge of the pulse. In this case, the leading edge of the pulse

will heat electrons earlier compared to the other cases resulting in an increased thermal expansion of the target. This results in RIT occurring earlier during the interaction as shown in case **Z** (figure 6.14 (d)). For the other cases, the expansion of the target is reduced, resulting in RIT later in the interaction.

If RIT takes place earlier on the rising edge profile, the hole boring RPA phase of the laser pulse is less efficient. Observing the front surface of the target, the degree of hole boring is greater for case **X** than case **Z**, shown in figure 6.14 (d). This could explain why a small population of high energy protons are accelerated close to the laser axis in the proton spectra obtained from the experiment. The steeper rising edge restricts the degree of expansion, resulting in a reduced density gradient. When the main peak of the pulse interacts with this gradient it is sufficient to drive electrons forward into the target. This effect is less apparent in the other cases because of the large temporal width at the 1% level, resulting in the target expanding a great deal before the peak of the pulse can interact with it.

The electron population expansion drives, a expansion in the ion population. The expansion of the C^{6+} and proton population are shown in figure 6.15 for cases **X** and **Z**. Figure 6.15 (a-c) presents the results for case **X** for (a) t =-300 fs, (b) t = 100 fs and (c) t = 700 fs with respect to the time at which the peak of the pulse interacts with the target. Figure 6.15 (d-f) presents the corresponding results for case **Z** at the same time steps. The final time step of the simulation, t = 900 fs, is shown in figure 6.17. As discussed earlier, the expansion of the ions for case **Z** is faster than in case **X** due to the larger width on the rising edge. The expansion of the proton front is plotted as a function of time in figure 6.16 for all three cases.

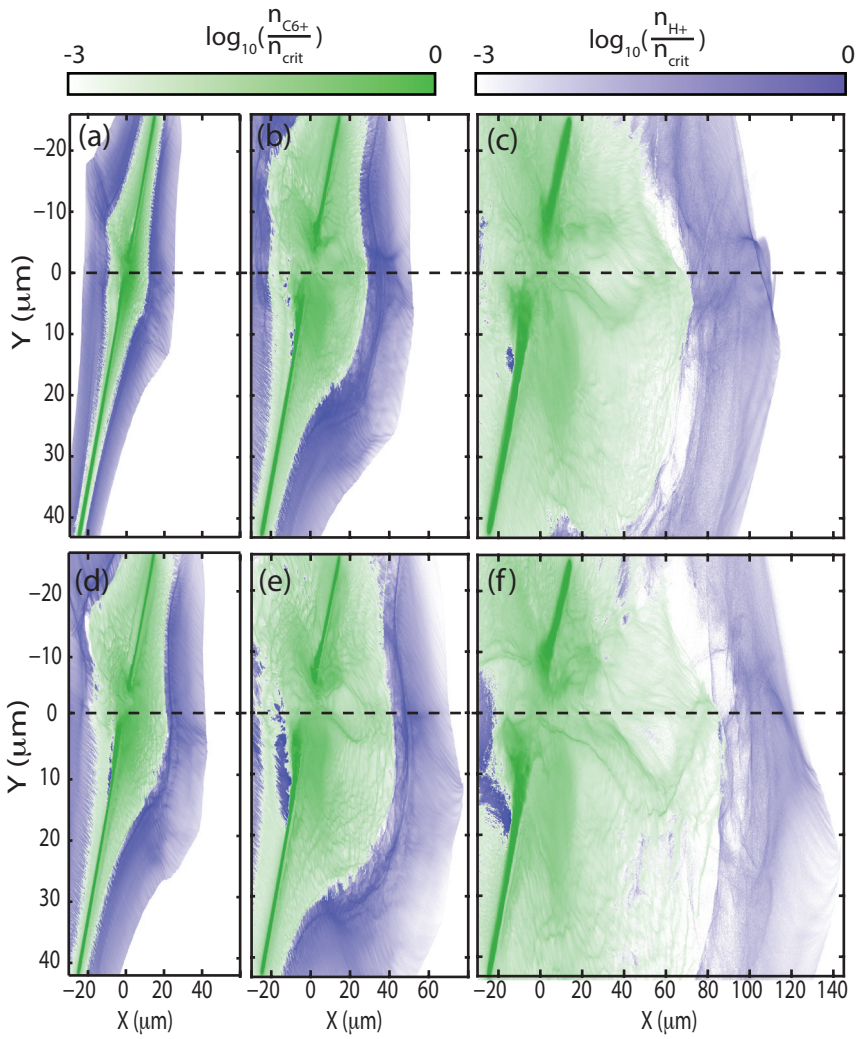

Figure 6.15: (a-c) Simulation results from case **X**, showing the ion density for C^{6+}, in green, and protons, in blue for: (a)t = -300 fs (b) t = 100 fs and (c) t= 700 fs. (d-f) represents the same time steps for case **Z**.

The expansion of the protons was tracked along the laser axis (Y= 0 μm) and the results are plotted in figure 6.16. The laser axis component was chosen to compare with the experimental results, as the highest energy protons were observed along this axis. Similar to the electron expansion shown in figure 6.14, the proton expansion in case **Z** along laser axis is much greater than the other two example cases. As previously noted, RIT occurs earlier in this case compared to the other two example cases due to the increased degree of electron population expansion. In case **X**, transparency occurs closer to the peak of the pulse where the hole boring RPA mechanism dominates, as discussed in the previous chapter.

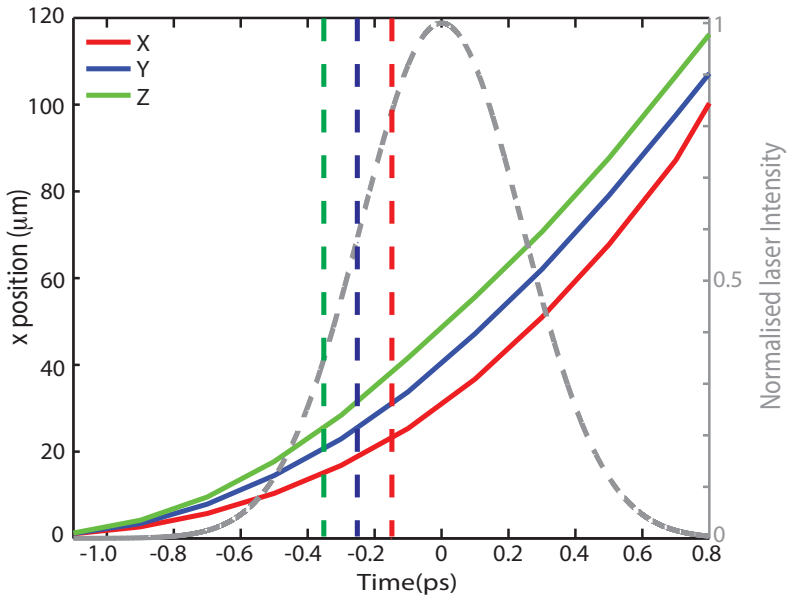

Figure 6.16: Position of the proton front along the laser axis (Y= 0 μm) as a function of time. The temporal profile of the laser intensity is also shown in gray with dashed vertical lines added to indicate the onset of transparency for the corresponding cases. The three cases plotted as: **X** in red, **Y** in blue and **Z** in green.

These simulation results demonstrate that the rising edge of the pulse even on the picosecond time-scale can a have significant effect on the target plasma expansion. This expansion strongly affects the underlying laser driven ion acceleration mechanisms.

The rising edge of the pulse does not only affect the expansion of the target, but also the maximum proton energies. Figure 6.17 displays the ion densities and kinetic energy for cases **X**, (a-b) and **Z**, (c-d), at $t = 900$ fs. Experimentally the highest proton energies were observed close to laser axis, as measured by TP 1, where the energies ranged from 20 - 70 MeV. Figure 6.17(b), case **X**, shows a population of highly energetic protons directed along the laser axis which is not observed for case **Z**. This is due to the hole boring acceleration being dominant in case **X** as the target has a smaller degree of expansion compared to case **Z**. A large population of high energy protons, in case **Z**, are directed in the target normal direction which is not present in case **X**. The enhancement along laser

axis can be observed in more detail by analysing the energy of the protons along laser axis.

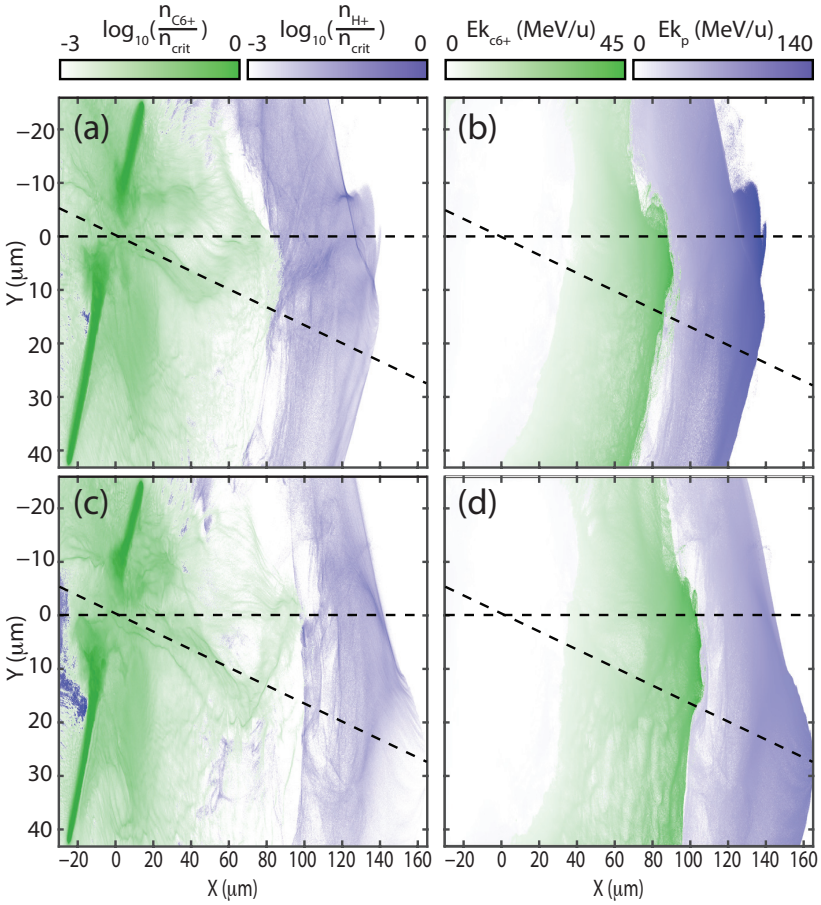

Figure 6.17: Simulation results showing: (a) Ion densities and (b) kinetic energy for the L = 100 nm target at 900 fs after the interaction of the laser pulse peak for case **X**: Green - C^{6+} ions, Blue - protons. (c-d) Same for case **Z**

Figure 6.18 shows the proton energy as a function of direction of laser axis propagation, X. Figure 6.18(a-c) presents case **X** for (a) t = -300 fs, (b) t = 0 fs and (c) t = 600 fs, respectively, and (d-f) presents case **Z** for the same times. Early, at t = -300 fs the TNSA mechanism dominates and the layer expands more quickly for case **Z**. Prior to t = 0 fs, both cases experience RPA due to the laser pressure at the target front surface. In case **Z**, the target has become transparent earlier, resulting in less efficient RPA but still experiences a slight

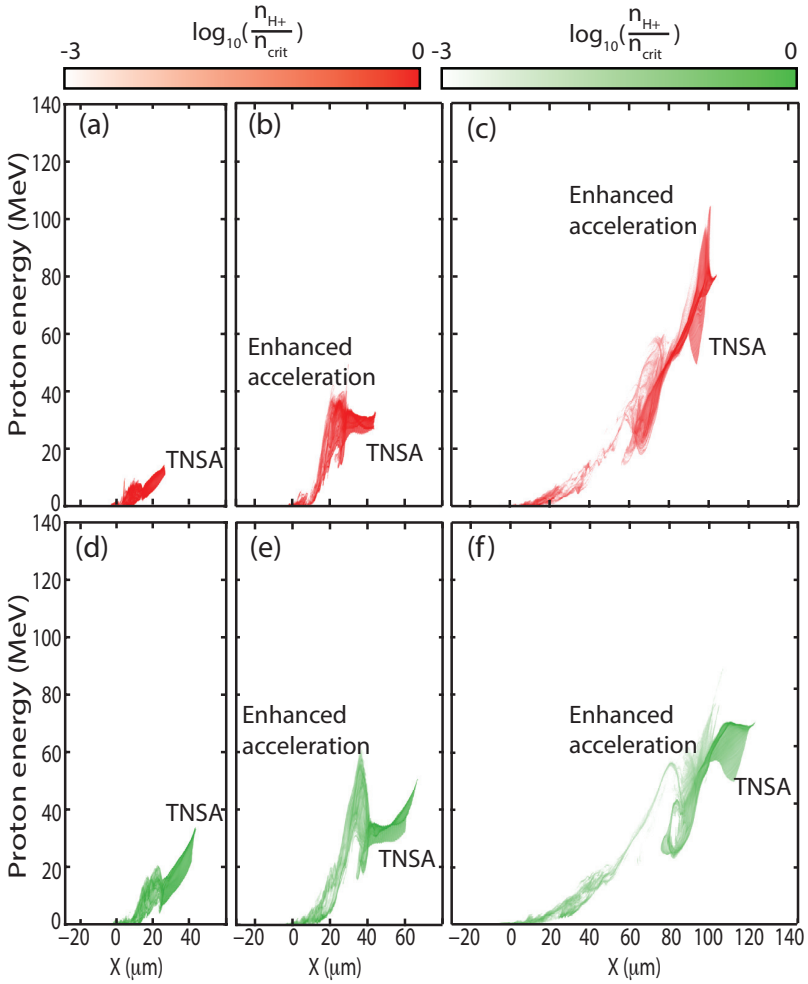

Figure 6.18: Energy-space plot of the proton beam denisty along laser axis for (a) t = -300 fs, (b) t = 0 fs and (c) t = 600 fs for case **X** and (d-f) same time steps for case **Z**.

enhancement at t = 0 fs. In case **X**, transparency later than in case **Z** enabling the hole boring front to push further into the target as shown in the electron expansion in figure 6.14. This leads to enhanced acceleration as shown in figure 6.18(b) and when the target eventually undergoes RIT, the protons accelerated from the hole boring propagate through and overtakes the TNSA accelerated protons. Therefore, inducing a relatively small expansion, as in case **X**, results in an energy enhancement along laser axis. The result of this can be seen at t = 600 fs. Here, the peak proton energy in case **Z** only reaches ∼70 MeV whereas in case **X** the peak energy reaches ∼110 MeV. Inducing a small pre-expansion in the

target enables laser axis accelerated protons to be enhanced by the front surface hole boring whereas large pre-expansion can result in less efficient acceleration of protons along this axis.

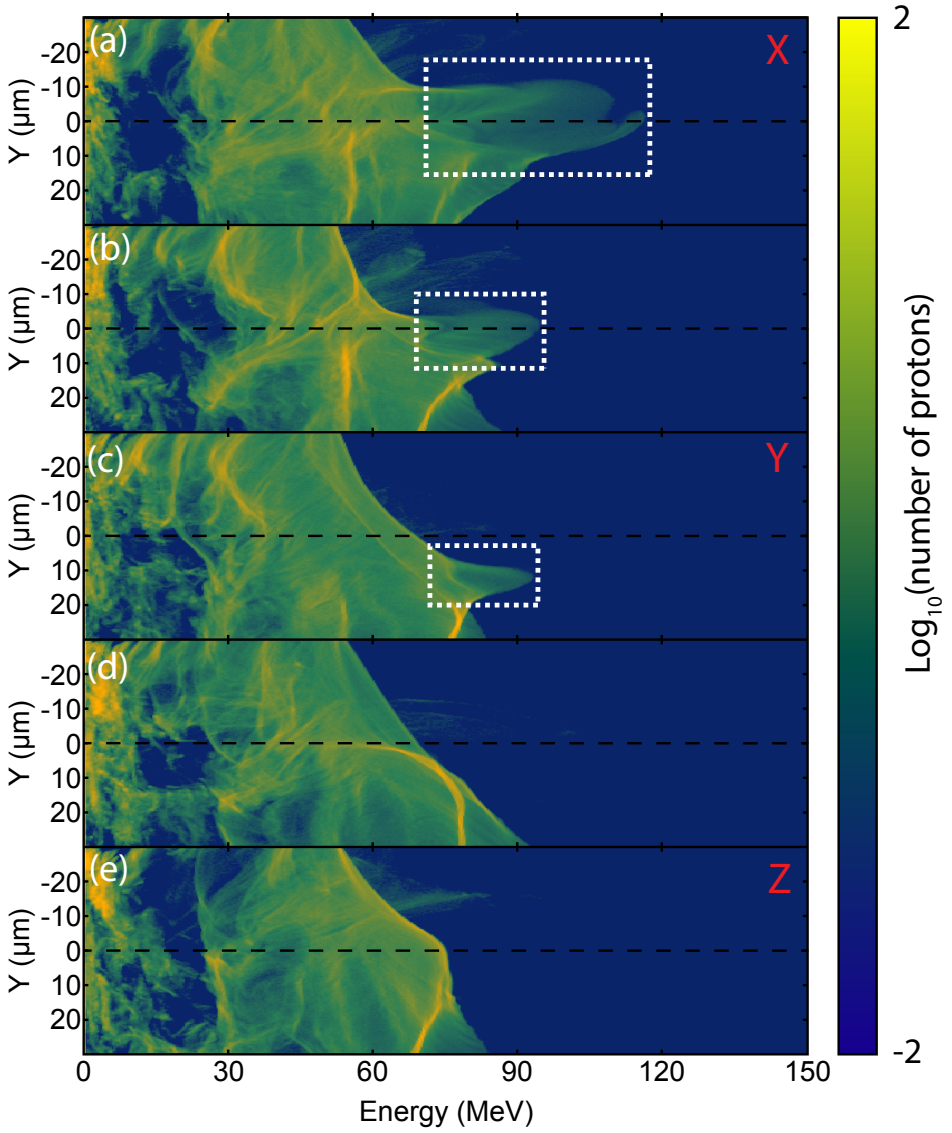

Figure 6.19: Simulation result showing the energy distribution of the protons across the Y dimension of the simulation for all studies carried out (a) $\tau_{1\%} = 1.3$ ps (b) $\tau_{1\%} = 1.4$ ps (c) $\tau_{1\%} = 1.47$ ps (d) $\tau_{1\%} = 1.52$ ps and (e) $\tau_{1\%} = 1.55$ ps with cases **X**, **Y** and **Z** labelled.

Figure 6.19 shows the spatial distribution of protons in the Y direction as a function of energy for all studies carried out. From top to bottom the temporal

width of the laser pulse at 1%, from the peak, with (a) $\tau_{1\%} = 1.3$ ps, (b) $\tau_{1\%} = 1.4$ ps, (c) $\tau_{1\%} = 1.47$ ps, (d) $\tau_{1\%} = 1.52$ ps and (e) $\tau_{1\%} = 1.55$ ps. The effect of expansion of the target, discussed earlier, can be observed in the proton beam accelerated along the laser axis. In case **Z**, where the 1% temporal width is the smallest, a large population of protons are predominantly accelerated along laser axis to high energies. As the temporal width is increased and a large degree of expansion is induced in the target, the number of protons accelerated along laser axis starts to decrease as shown in figure 6.19. The proton energies along laser axis vary from $\sim$ 80 MeV to $\sim$ 120 MeV due to the rising edge of the laser pulse in the simulation. As the temporal width at 1% of the pulse increases, the protons begin to be predominantly accelerated along the target normal axis due to the pre-expansion of the target, resulting in inefficient radiation pressure acceleration of the front surface along laser axis. This simulation study of the rising edge effects on the proton energy shows good agreement with the trends measured in the experiment, as shown in figure 6.20.

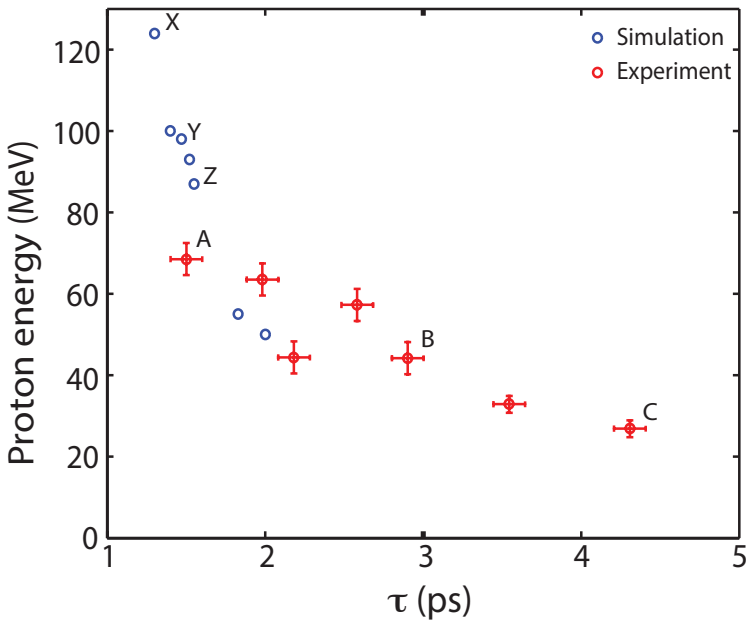

Figure 6.20: Comparison of the experimental and simulation results of the proton energy as a function of the temporal width at 1% of the peak.

Figure 6.20 displays the maximum proton energy as a function of the temporal width at 1% from the experimental and simulation results. A similar trend is seen in both studies where the proton energies decrease as the temporal width increases. As the simulations produced a similar result to the experimental study, we conclude that the degree of pre-expansion of the target plays a major part in the acceleration of protons. The variation of the proton maximum energy is a result of the rising edge of the laser pulse, which affects the expansion of the target and thus the multiple acceleration mechanisms that take place over the course of laser-plasma interactions. Having a short temporal width at the 1% level induces a small expansion of the target and also, unlike the long temporal width case, RIT occurs near the peak of the pulse which enables a longer period of hole boring at the front surface. This results in a population of protons being accelerated along laser axis rather than target normal and overtakes the protons accelerated by the TNSA mechanisms.

6.4 Summary and conclusion

In summary, the effects of target expansion from the rising edge of the ultra-intense laser pulse interacting with ultra-thin CH foils, in the transparency regime has been investigated.

The effects of the rising edge profile of the laser pulse has on the resultant peak proton energies was investigated. During the experimental campaign the rising edge of the pulse was observed to vary for each shot and this resulted in a range of maximum proton energies. Through a numerical investigation it was found that the expansion of the target was different for each case of the rising edge profile studied and this gave rise to a variation of maximum proton energies. It has been shown that the energy of accelerated protons is extremely sensitive to the rising edge of the pulse on the picosecond time-scale, and in turn the degree of

expansion in the target. The expansion induced by the rising edge of the pulse, or the temporal width at 1% from the peak of the pulse, plays a vital role in the optimisation of proton acceleration mechanisms. Higher proton energies are predicted, when ions experience a limited expansion prior to the onset of RIT. The resultant proton energies from the simulation study gave similar trends to the results obtained from the experiment.

Using thick target Sahai *et al* [145] studied the effect of relativistically induced transparency acceleration (RITA), discussed in chapter 3, where the rising-edge laser profile interacts with a target with an electron density gradient. The front surface plasma dynamics inferred in these studies could be applicable to the results presented in this chapter, albeit for nanometer-thin targets. The rising edge of the laser pulse, whether it is long or short, affects the plasma expansion and more importantly the plasma scale length. This study by Sahai *et al* [145] could possibly explain why the proton energies are sensitive to the rising edge of the laser pulse.

The work presented here highlights the need for improving the laser contrast on the picosecond time-scale. If these conditions can be met experimentally, proton energies are expected to be higher and stable for a given target thickness. These results provide new insight into the interaction physics taking place in the transparency regime of laser-solid plasma interactions. They demonstrate that for the currently available laser systems, by improving the contrast, it is possible to achieve higher and stable proton energies by reducing the target expansion prior to the onset of RIT.

Chapter 7

Summary and Conclusions

Significant progress has been made in the field of laser-driven ion acceleration in the past decade, however challenges still remain to find new methods of optimising the ion beam properties before they can be used for the proposed applications discussed in chapter 1.

This thesis has described work from a series of experiments and numerical PIC simulations designed to investigate the acceleration of protons from high intensity laser-solid interactions using ultra-thin foils in the relativistic transparency regime. Both experiments with nanometre-scale targets were performed on the Vulcan Petawatt laser and have provided significant advances in understanding the multiple acceleration mechanisms involved. PIC simulations were used to provide insight into the physics underpinning of these acceleration mechanisms and the cumulative effects of multiple mechanisms occurring over the duration of the laser pulse.

7.1 Summary of main results

Intra-pulse transition between ion acceleration mechanisms

The work presented in chapter 5 identified a number of ion acceleration mechanisms taking place over the duration of a pico-second laser interaction. From the experimental study, distinct features in the spatial-intensity profile of the proton beam, such as a low-energy annular profile, bubble-like structures and regions of energy enhancement were observed. Two of these features, the ring profile and the region of enhanced proton energy, were observed to be a signature of the transition between acceleration mechanisms [126] and were investigated in detail. The annular profile was observed at low proton energies, and the divergence angle varied with target thickness and resultant proton energy. The component of the accelerated proton beam which experienced the energy enhancement, associated with the formation of a localised electron jet [126] at the rear surface of the target, is observed to have a low divergence angle, similar to the ion beams predicted by RPA studies [58].

The underlying dynamics of the experiment were investigated using PIC simulations. It was demonstrated that multiple ion acceleration mechanisms take place over the duration of the interaction. Initially the TNSA mechanism dominates the process and protons from the rear surface are accelerated by the sheath field. As the intensity of the Gaussian temporal profile of the laser increases, a transition takes place from the TNSA phase to the hole-boring RPA mechanism. This acceleration mechanism drives the bulk target ions, in this case the Al ions, into the rear of the accelerated TNSA protons. The slow TNSA protons are driven radially by the bulk ions giving rise to a low energy annular profile in the proton beam. The third transition occurs when the electron density of the target drops below the relativistically corrected critical density ($n_e < \gamma n_{crit}$), and the target becomes transparent to the laser pulse, in a process known as relativistic induced

transparency (RIT). This results in the propagation of the laser pulse through the now underdense target and gives rise to volumetric heating of electrons, leading to a transparency enhanced acceleration. Moreover, when the target undergoes RIT, a localised electron jet forms at the rear of the target. In this channel, the proton energies are enhanced, resulting in a low divergence beam accelerated along laser axis.

Laser-driven ion acceleration using ultra-thin foils is a complicated process, especially when RIT takes place. Over the course of the interaction, multiple acceleration mechanisms can occur, with the dominant mechanism changing over the duration of the laser pulse. An important application of annular proton beams was demonstrated by Temporal *et al* [182], for a proton-driven fast ignition scheme [35]. Using an annular proton beam in conjunction with a secondary uniform proton beam, the total energy required for ignition can be reduced by a factor of two compared to using a single uniform beam.

Laser contrast effects on laser-driven proton energies in the relativistic induced transparency regime

Building upon the insights developed in the previous investigation, the results reported in chapter 6 explore the role that the laser contrast and target expansion have on accelerated proton energies. Using a fixed target (CH) thickness of 100 nm, the temporal rising edge effects of typical experimental laser pulses on maximum proton energies was studied. The maximum energy of the protons was found to range from 20 - 70 MeV for identical target thicknesses and the shot-to-shot temporal width of the laser pulse at the target was modelled using a second order autocorrelator. Measuring the temporal width of the pulse at 50%, 10%, and 1% temporal width of the pulse, the proton energies were seen to have a clear correlation with the 1% level. As the temporal width increased, the proton energies decreased. Also, the level of transmission of the laser-pulse through the

target for each shot is observed to be sensitive to the laser contrast.

To understand the effect the rising edge profile has on laser-driven ion energies, 2D PIC simulations were carried out. These studies investigated a number of laser pulse profiles where the rising edge varied in order to observe the effects on the target expansion and resultant proton energies. Furthermore, this study focused on the variation of the 1% temporal width of the pulse, which was the level at which the maximum proton energies were found to be sensitive experimentally.

The numerical simulations produced a similar trend to the experimental study, where it was concluded that the degree of target pre-expansion plays a major role in the acceleration of protons. As the 1% temporal width of the pulse is increased, there is increased heating which drives early expansion of the target and which impacts the multiple acceleration mechanisms that take place over the duration of the laser-plasma interactions. Having a short temporal width at the 1% level induces a small pre-expansion of the target and leads to the target undergoing RIT near the peak of the pulse, which can result in an enhancement of the proton energies in the population accelerated along laser axis. This population of protons gains energy from the hole boring mechanism and overtakes the TNSA proton layer. If the temporal width at 1% is increased, RIT occurs much quicker in the interaction. The hole boring mechanism, in this scenario, is less efficient, resulting in reduced enhancement of the proton energy along the laser axis. In this case the TNSA mechanism dominates and the highest energy protons are accelerated along target normal. This investigation revealed that the rising edge of the laser intensity profile, especially at 1%, can lead to variation in the maximum proton energy, shot-to-shot, through pre-expansion of the target.

It has been shown that the temporal width at 1% from the peak of the pulse is an important laser parameter that needs to be considered in laser-driven ion acceleration from ultra-thin nanometre foils. Temporal variation at this level can lead to a range of maximum proton energies and can alter the underlying plasma

dynamics of the target, resulting in RIT occurring sooner when the temporal width is increased. Improving the laser contrast on the picosecond time-scale could result in higher and more stable proton energies.

7.2 Concluding remarks

This thesis has described experimental and numerical studies of laser-driven ion acceleration, using a present state-of-the-art high power laser system. The results show that a multi-species target can give rise to a low energy annular profile in the spatial-intensity profile of the proton beam due to multiple acceleration mechanisms occurring over the duration of the laser pulse. Also, variation in the temporal width, at the 1% level, of the laser pulse profile can result in a range of proton energies for fixed target parameters. These studies highlight the sensitivity of laser-solid interactions using ultra-thin foils, as they give rise to multiple acceleration mechanisms and the laser contrast can affect the physical dynamics of the target.

The progression of laser-driven ion acceleration closely depends on the development of new laser technology. Future laser systems such as the Vulcan 10PW project [183] and ELI [184–186], have been proposed to provide laser energies of 300 J in 30 fs pulse durations with intensities of up $\sim 10^{23}$ W/cm^2 when focused, resulting in steeper pulse profiles. Extrapolating the laser intensity scaling of maximum ion energy to this intensity [5, 87], GeV protons are predicted and at these intensities RPA mechanisms are expected to dominate. For current laser facilities and technology, improvements in reducing the rising edge of the laser pulse, in particular having a short temporal width at the 1% level from the peak of the pulse, have been shown to give higher proton energies with recent experimental evidence, in chapter 6, pointing towards this.

Investigating the dynamics of laser-solid interactions using ultra-thin foils, is

highly important to the development of ion acceleration. Proposed mechanisms, such as the light-sail mode in the radiation pressure acceleration regime, have predicted ion energies much higher than are currently attainable experimentally, and rely on interactions in this ultra-thin nanometre scale regime. Furthermore, in order to be desirable for applications, the quality of accelerated beams have to be improved. Thus, the main focus of current research is not only on ion energies achieved but also the spatial-intensity profile of these ions. Researchers around the world are developing new ideas and techniques to push the boundaries of laser-driven ion acceleration: many are investigating acceleration mechanisms such as RPA and transparency enhanced acceleration, whilst some are fine-tuning ion beams generated from the TNSA process. In the future ion beams accelerated from laser-solid interactions could be an invaluable tool for researchers.

Bibliography

[1] P. Gibbon. Short Pulse Laser Interaction With Matter: An Inroduction. Imperial College Press, 2005.

[2] R. J. Gray. On Mechanisms and of and Laser-Coupling to Fast and Electrons in Ultraintense Laser-Solid Interactions. PhD thesis, University of Strathclyde, 2013.

[3] T. J. M. Boyd. The Physics of Plasmas. Cambridge University Press, 2003.

[4] O. Tresca. Optimisation and control of high and intensity laser accelerated ion beams. PhD thesis, University of Strathclyde, 2012.

[5] H. Daido et al. Review of laser-driven ion sources and their applications. Reports on Progress in Physics, 75(5):056401, 2012.

[6] R. Wideröe. Über ein neues prinzip zur herstellung hoher spannungen. Archiv für Elektrotechnik, 21(4):387–406, 1928.

[7] E. O. Lawrence. Methods and apparatus for the acceleration of ions., 1934.

[8] T. Tajima et al. Laser electron and accelerator. Phys. Rev. Lett., 43(4), 1979.

[9] W. P. Leemans et al. Gev electron beams from a centimetre-scale accelerator. Nature Physcis, 2(10):696, 2006.

[10] W. P. Leemans et al. Multi-gev electron beams from capillary-discharge-guided subpetawatt laser pulses in the self-trapping regime. Phys. Rev. Lett., 113(24):245002, 2014.

[11] A. Modena et al. Electron acceleration from the breaking of relativistic plasma waves. Nature, 377(6550):606, 1995.

[12] V. Malka et al. Electron acceleration by a wake field forced by an intense ultrashort laser pulse. Science, 298(5598):1596, 2002.

[13] S. P. D. Mangles et al. Monoenergetic beams of relativistic electrons from intense laser-plasma interactions. Nature, 431(7008):535, 2004.

[14] C. G. R. Geddes et al. High-quality electron beams from a laser wakefield accelerator using plasma-channel guiding. Nature, 431(7008):538, 2004.

[15] J. Faure et al. A laser-plasma accelerator producing monoenergetic electron beams. Nature, 431(7008):541, 2004.

[16] W. I. Linlor. Ion energies produced by laser giant pulse. Appl. Phys. Lett., 3(11):210, 1963.

[17] S. J. Gitomer et al. Fast ions and hot electrons in the laser-plasma interaction. Physics of Fluids, 29(8):2679, 1986.

[18] D. Strickland et al. Compression of amplifed chirped optical pulses. Optics Communications, 55(6):447, 1985.

[19] P. Maine et al. Generation of ultrahigh and peak power and pulses by and chirped pulse and amplification. IEEE Journal of Quantum Electronics, 24(2):398, 1988.

[20] R. A. Snavely et al. Intense high-energy proton beams from petawatt-laser irradiation of solids. Phys. Rev. Lett., 85(14):2945, 2000.

[21] F. Wagner et al. Maximum proton energy above 85 MeV from the relativistic interaction of laser pulses with micrometer thick CH_2 targets. Phys. Rev. Lett., 116(20):205002, 2016.

[22] L. Romagnani et al. Dynamics of electric fields driving the laser acceleration of multi-mev protons. Phys. Rev. Lett., 95(19):195001, 2005.

[23] M. Borghesi et al. Measurement of highly transient electrical charging following high-intensity lasersolid interaction. Applied Physics Letters, 82(10):1529–1531, 2003.

[24] W. Wieszczycka Proton radiotherapy accelerators. River Edge, New Jersey: World Scientific Publishing Co Pte Ltd, 2001.

[25] V. S. KhoroshkovProton beams in radiotherapy. European Journal of Physics, 19(6):523, 1998.

[26] S. Bulanov et al. Oncological hadrontherapy with laser ion accelerators. Physics Letters A, 299(23):240 – 247, 2002.

[27] V. Malka et al. Practicability of protontherapy using compact laser systems. Medical Physics, 31(6):1587–1592, 2004.

[28] K. Krushelnick et al. Ultrahigh-intensity laser-produced plasmas as a compact heavy ion injection source. IEEE Transactions on Plasma Science, 28(4):1110–1155, 2000.

[29] J. Lindl. Development of the indirect?drive approach to inertial confinement fusion and the target physics basis for ignition and gain. Phys. Plasmas, 2(11):3933–4024, 1995.

[30] M. Tabak et al. Ignition and high gain with ultrapowerful lasers. Phys. Plasmas, 1(5):1626–1634, 1994.

[31] P. McKenna et al. Influence of low-temperature resistivity on fast electron transport in solids: scaling to fast ignition electron beam parameters. Plasma Physics and Controlled Fusion, 57(6):064001, 2015.

[32] M. H. Key. Status of and prospects for the fast ignition inertial fusion concept. Phys. Plasmas, 14(5):055502, 2007.

[33] R. Kodama et al. Fast heating of ultrahigh-density plasma as a step towards laser fusion ignition. Nature, 412(798-802), 2002.

[34] J. Fernndez et al. Fast ignition with laser-driven proton and ion beams. Nuclear Fusion, 54(5):054006, 2014.

[35] M. Roth et al. Fast ignition by intense laser-accelerated proton beams. Phys. Rev. Lett., 86(3):436439, 2001.

[36] A. M. Koehler. Proton radiography. Science, 160(3825):303–304, 1968.

[37] N. King et al. An 800-mev proton radiography facility for dynamic experiments. Nuclear Instruments and Methods in Physics Research Section A: Accelerators, Spectrometers, Detectors and Associated Equipment, 424(1):84 – 91, 1999.

[38] M. Borghesi et al. Multi-mev proton source investigations in ultraintense laser-foil interactions. Phys. Rev. Lett., 92(5):055003, 2004.

[39] M. Roth et al. Energetic ions generated by laser pulses: A detailed study on target properties. Phys. Rev. ST Accel. Beams, 5(6):061301, 2002.

[40] A. Y. Faenov et al. Submicron ionography of nanostructures using a femtosecond-laser-driven-cluster-based source. Applied Physics Letters, 95(10):101107, 2009.

[41] M. Borghesi et al. Proton imaging: a diagnostic for inertial confinement fusion/fast ignitor studies. Plasma Physics and Controlled Fusion, 43(12A):A267, 2001.

[42] M. Borghesi et al. Electric field detection in laser-plasma interaction experiments via the proton imaging technique. Phys. Plasmas, 9(5):2214–2220, 2002.

[43] A. J. Mackinnon et al. Proton radiography as an electromagnetic field and density perturbation diagnostic (invited). Review of Scientific Instruments, 75(10):3531–3536, 2004.

[44] L. Willingale et al. Proton probe measurement of fast advection of magnetic fields by hot electrons. Plasma Physics and Controlled Fusion, 53(12):124026, 2011.

[45] S. Kar et al. Dynamics of charge-displacement channeling in intense laser-plasma interactions. New Journal of Physics, 9(11):402, 2007.

[46] L. Romagnani et al. Observation of collisionless shocks in laser-plasma experiments. Phys. Rev. Lett., 101(2):025004, 2008.

[47] P. K. Patel et al. Isochoric heating of solid-density matter with an ultrafast proton beam. Phys. Rev. Lett., 91(12):125004, 2003.

[48] R. A. Snavely et al. Laser generated proton beam focusing and high temperature isochoric heating of solid matter. Phys. Plasmas, 14(9):092703, 2007.

[49] D. A. MacLellan et al. Annular fast electron transport in silicon arising from low-temperature resistivity. Phys. Rev. Lett., 111(9):095001, 2013.

[50] D. A. MacLellan et al. Tunable mega-ampere electron current propagation in solids by dynamic control of lattice melt. Phys. Rev. Lett., 113(18):185001, 2014.

[51] I. Spencer et al. Laser generation of proton beams for the production of short-lived positron emitting radioisotopes. Nuclear Instruments and Methods in Physics Research Section B: Beam Interactions with Materials and Atoms, 183(34):449 – 458, 2001.

[52] P. McKenna et al. Demonstration of fusion-evaporation and direct-interaction nuclear reactions using high-intensity laser-plasma-accelerated ion beams. Phys. Rev. Lett., 91(7):075006, 2003.

[53] K. W. D. Ledingham et al. High power laser production of short-lived isotopes for positron emission tomography. Journal of Physics D: Applied Physics, 37(16):2341, 2004.

[54] P. McKenna et al. Broad energy spectrum of laser-accelerated protons for spallation-related physics. Phys. Rev. Lett., 94(8):084801, 2005.

[55] K. Ledingham. Laser induced nuclear physics and applications. Nuclear Physics A, 752:633 – 644, 2005.

[56] A. Alejo et al. Recent advances in laser-driven neutron sources. Il Nuovo Cimento C, 38C(6):1–7, 2016.

[57] J. Schreiber et al. Invited review article: "hands-on" laser-driven ion acceleration: A primer for laser-driven source development and potential applications. Review of Scientific Instruments, 87(7):071101, 2016.

[58] T. Esirkepov et al. Highly efficient relativistic-ion generation in the laser-piston regime. Phys. Rev. Lett., 92(17):175003, 2004.

[59] A. Macchi et al. Laser acceleration of ion bunches at the front surface of overdense plasmas. Phys. Rev. Lett., 94(16):165003, 2005.

[60] A. P. L. Robinson et al. Radiation pressure acceleration of thin foils with circularly polarized laser pulses. New Journal of Physics, 10(1):013021, 2008.

[61] S. Wilks et al. Absorption of ultra-intense laser pulses. Phys. Rev. Lett., 69(9):1383, 1992.

[62] A. P. L. Robinson et al. Relativistically correct hole-boring and ion acceleration by circularly polarized laser pulses. Plasma Physics and Controlled Fusion, 51(2), 2009.

[63] W. L. Kruer. The Physics of Laser Plasma Interactions. Westview Press, 2003.

[64] A. Macchi. A Superintense Laser-Plasma Interaction Theory Primer. Springer, 2013.

[65] S. C. Wilks et al. Absorption of ultrashort and ultra-intense laser and light by solids and overdense plasmas. IEEE Journal of Quantum Electronics, 33(11):1954, 1997.

[66] I. V. Keldysh. Ionization in the field of a strong electromagnetic wave. Sov. Phys. JETP, 20:1307, 1965.

[67] F. F. Chen. Introduction to plasma physics and controlled fusion, volume 1. Springer, 1984.

[68] F. Cattani et al. Threshold of induced transparency in the relativistic interaction of an electromagnetic wave with overdense plasmas. Phys. Rev. E, 62(1):1234, 2000.

[69] S. Palaniyappan et al. Pulse shape measurements using single shot-frequency resolved optical gating for high energy (80 j) short pulse (600 fs) laser. Review of Scientific Instruments, 81(10), 2010.

[70] S. Palaniyappan et al. Dynamics of relativistic transparency and optical shuttering in expanding overdense plasmas. Nat Phys, 8(10), 2012.

[71] S. Palaniyappan et al. Efficient quasi-monoenergetic ion beams from laser-driven relativistic plasmas. Nat Comms, 6:10170, 2015.

[72] F. Brunel. Not-so-resonant, resonant absorption. Phys. Rev. Lett., 59(1):52, 1987.

[73] W. L. Kruer et al. Jxb heating by very intense laser light. Physics of Fluids, 28(1):430–432, 1985.

[74] A. R. Bell et al. Fast electron transport in laser-produced plasmas and the kalos code for solution of the vlasov fokker planck equation. Plasma Physics and Controlled Fusion, 48(3), 2006.

[75] J. J. Santos et al. Fast electron transport in ultraintense laser pulse interaction with solid targets by rear-side self-radiation diagnostics. Phys. Rev. Lett., 89(2):025001, 2002.

[76] H. Alfven. On the motion of cosmic rays in interstellar space. Phys. Rev., 55(5):425–429, 1939.

[77] A. J. Mackinnon et al. Enhancement of proton acceleration by hot-electron recirculation in thin foils irradiated by ultraintense laser pulses. Phys. Rev. Lett., 88(21):215006, 2002.

[78] Y. Sentoku et al. High energy proton acceleration in interaction of short laser pulse with dense plasma target. Phys. Plasmas, 10(5):2009–2015, 2003.

[79] S. H. Yong et al. Hot-electron recirculation in ultraintense laser pulse interactions with thin foils. Phys. Plasmas, 14(10):103106, 2007.

[80] C. A. J. Palmer et al. Rayleigh-taylor instability of an ultrathin foil accelerated by the radiation pressure of an intense laser. Phys. Rev. Lett., 108(22):225002, 2012.

[81] A. J. Cole et al. Measurement of rayleigh-taylor instability in a laser-accelerated target. Nature, 299:329–331, 1982.

[82] S. P. Sarraf et al. Ion-ion two-stream instability in multispecies laser-produced plasma. Phys. Rev. A, 27(4):2110–2113, 1983.

[83] B. J. Albright et al. Relativistic buneman instability in the laser breakout afterburner. Phys. Plasmas, 14(9):094502, 2007.

[84] O. Buneman. Dissipation of currents in ionized media. Phys. Rev., 115(3):503–517, 1959.

[85] B. J. Albright et al. Theory of laser acceleration of light-ion beams from interaction of ultrahigh-intensity lasers with layered targets. Phys. Rev. Lett., 97(11):115002, 2006.

[86] M. King et al. Energy exchange via multi-species streaming in laser-driven ion acceleration. Plasma Physics and Controlled Fusion, 59(1):014003, 2017.

[87] A. Macchi et al. Ion acceleration by superintense laser-plasma interaction. Reviews of Modern Physics, 85(2):751, 2013.

[88] V. Yanovsky et al. Ultra-high intensity- 300-tw laser at 0.1 hz repetition rate. Opt. Express, 16(3):2109–2114, 2008.

[89] S. C. Wilks et al. Energetic proton generation in ultra-intense laser-solid interactions. Phys. Plasmas, 8(2):542, 2001.

[90] P. Mora. Plasma expansion into a vacuum. Phys. Rev. Lett., 90(18):185002, 2003.

[91] M. Schollmeier et al. Laser beam-profile impression and target thickness impact on laser-accelerated protons. Phys. Plasmas, 15(5):053101, 2008.

[92] J. Fuchs et al. Comparison of laser ion acceleration from the front and rear surfaces of thin foils. Phys. Rev. Lett., 94(4):045004, 2005.

[93] E. L. Clark et al. Measurements of energetic proton transport through magnetized plasma from intense laser interactions with solids. Phys. Rev. Lett., 84(4):670–673, 2000.

[94] M. Zepf et al. Fast particle generation and energy transport in laser-solid interactions. Phys. Plasmas, 8(5):2323, 2001.

[95] M. Kaluza et al. Influence of the laser prepulse on proton acceleration in thin-foil experiments. Phys. Rev. Lett., 93(4):045003, 2004.

[96] P. McKenna et al. Characterization of proton and heavier ion acceleration in ultrahigh-intensity laser interactions with heated target foils. Phys. Rev. E, 70(3):036405, 2004.

[97] M. Borghesi et al. Fast ion generation by high-intensity laser irradiation of solid targets and applications. Fusion Science and Technology, 49(3):412–439, 2006.

[98] Y. Murakami et al. Observation of proton rear emission and possible gigagauss scale magnetic fields from ultra-intense laser illuminated plastic target. Phys. Plasmas, 8(9):4138–4143, 2001.

[99] E. dHumires et al. Proton acceleration mechanisms in high-intensity laser interaction with thin foils. Phys. Plasmas, 12(6):062704, 2005.

[100] A. Pukhov. Three-dimensional simulations of ion acceleration from a foil irradiated by a short-pulse laser. Phys. Rev. Lett., 86(16):3562–3565, 2001.

[101] Y. Sentoku et al. High density collimated beams of relativistic ions produced by petawatt laser pulses in plasmas. Phys. Rev. E, 62(5):7271–7281, 2000.

[102] A. Maksimchuk et al. Forward ion acceleration in thin films driven by a high-intensity laser. Phys. Rev. Lett., 84(18):4108, 2000.

[103] K. Nemoto et al. Laser-triggered ion acceleration and table top isotope production. Applied Physics Letters, 78(5):595–597, 2001.

[104] S. P. Hatchett et al. Electron, photon, and ion beams from the relativistic interaction of petawatt laser pulses with solid targets. Phys. Plasmas, 7(5):2076, 2000.

[105] A. J. Mackinnon et al. Effect of plasma scale length on multi-mev proton production by intense laser pulses. Phys. Rev. Lett., 86(9):1769, 2001.

[106] M. Allen et al. Direct experimental evidence of back-surface ion acceleration from laser-irradiated gold foils. Phys. Rev. Lett., 93(26):265004, 2004.

[107] J. Fuchs et al. Comparative spectra and efficiencies of ions laser-accelerated forward from the front and rear surfaces of thin solid foils. Phys. Plasmas, 14(5):053105, 2007.

[108] T. E. Cowan et al. Ultralow emittance, multi-mev proton beams from a laser virtual-cathode plasma accelerator. Phys. Rev. Lett., 92(20):204801, 2004.

[109] M. Roth et al. Laser accelerated ions and electron transport in ultra-intense laser matter interaction. Laser and Particle Beams, 23(1):95–100, 2005.

[110] G. Marx. Interstellar vehicle propelled by terrestrial laser beam. Nature, 211(22):588–589, 1966.

[111] A. Macchi et al. "light sail" acceleration reexamined. Phys. Rev. Lett., 103(8):085003, 2009.

[112] X. Yan et al. Generating high-current monoenergetic proton beams by a circularly polarized laser pulse in the phase-stable acceleration regime. Phys. Rev. Lett., 100(13):135003, 2008.

[113] O. Klimo et al. Monoenergetic ion beams from ultrathin foils irradiated by ultrahigh-contrast circularly polarized laser pulses. Phys. Rev. ST Accel. Beams, 11(3):031301, 2008.

[114] X. Zhang et al. Instabilities in interaction of circularly polarized laser pulse and overdense target. Phys. Plasmas, 18(7):073101, 2011.

[115] T. Schlegel et al. Relativistic laser piston model: Ponderomotive ion acceleration in dense plasmas using ultraintense laser pulses. Phys. Plasmas, 16(8):083103, 2009.

[116] A. P. L. Robinson et al. Hole-boring radiation pressure acceleration with two ion species. Plasma Physics and Controlled Fusion, 51(9):095006, 2009.

[117] D. Haberberger et al. Collisionless shocks in laser-produced plasma generate monoenergetic high-energy proton beams. Nature Physics, 8(1):95, 2011.

[118] C. A. J. Palmer et al. Monoenergetic proton beams accelerated by a radiation pressure driven shock. Phys. Rev. Lett., 106(1):014801, 2011.

[119] A. Henig et al. Laser-driven shock acceleration of ion beams from spherical mass-limited targets. Phys. Rev. Lett., 102(9):095002, 2009.

[120] F. Dollar et al. Finite spot effects on radiation pressure acceleration from intense high-contrast laser interactions with thin targets. Phys. Rev. Lett., 108(17):175005, 2012.

[121] A. Henig et al. Radiation-pressure acceleration of ion beams driven by circularly polarized laser pulses. Phys. Rev. Lett., 103(24):245003, 2009.

[122] S. Kar et al. Ion acceleration in multispecies targets driven by intense laser radiation pressure. Phys. Rev. Lett., 109(18):185006, 2012.

[123] F. Pegoraro et al. Photon bubbles and ion acceleration in a plasma dominated by the radiation pressure of an electromagnetic pulse. Phys. Rev. Lett., 99(6):065002, 2007.

[124] A. Sgattoni et al. Laser-driven Rayleigh-Taylor instability: Plasmonic effects and three-dimensional structures. Phys. Rev. E, 91(1):013106, 2015.

[125] R. Capdessus et al. Influence of radiation reaction force on ultraintense laser-driven ion acceleration. Phys. Rev. E, 91(5):053105, 2015.

[126] H. W. Powell et al. Proton acceleration enhanced by a plasma jet in expanding foils undergoing relativistic transparency. New Journal of Physics, 17(10):103033, 2015.

[127] M. King et al. Ion acceleration and plasma jet formation in ultra-thin foils undergoing expansion and relativistic transparency. Nuclear Instruments and Methods in Physics Research Section A: Accelerators, Spectrometers, Detectors and Associated Equipment, 829:163 – 166, 2016.

[128] H. Padda et al. Intra-pulse transition between ion acceleration mechanisms in intense laser-foil interactions. Phys. Plasmas, 23(6):063116, 2016.

[129] J. Fuchs et al. Laser-driven proton scaling laws and new paths towards energy increase. Nature Physics, 2(1):48–54, 2006.

[130] J. Fuchs et al. Ion acceleration using high-contrast ultra-intense lasers. J. Phys. IV France, 133:1151–1153, 2006.

[131] A. Henig et al. Enhanced laser-driven ion acceleration in the relativistic transparency regime. Phys. Rev. Lett., 103(4):045002, 2009.

[132] Q. L. Dong et al. Optimization of ion acceleration in the interaction of intense femtosecond laser pulses with ultrathin foils. Phys. Rev. E, 68(2):026408, 2003.

[133] L. Yin et al. Gev laser ion acceleration from ultrathin targets: The laser break-out afterburner. Laser Part. Beams, 24(02), 2006.

[134] L. Yin et al. Monoenergetic and gev ion acceleration from the laser breakout afterburner using ultrathin targets. Phys. Plasmas, 14(5):056706, 2007.

[135] X. Q. Yan et al. Theory of laser ion acceleration from a foil target of nanometer thickness. Applied Physics B, 98(4):711–721, 2010.

[136] B. J. Albright et al. Ultraintense laser interaction with nanoscale targets: a simple model for layer expansion and ion acceleration. Journal of Physics: Conference Series, 244(4):042022, 2010.

[137] D. Jung et al. Efficient carbon ion beam generation from laser-driven volume acceleration. New Journal of Physics, 15(2):023007, 2013.

[138] D. Jung et al. Beam profiles of proton and carbon ions in the relativistic transparency regime. New Journal of Physics, 15(12):123935, 2013.

[139] D. Jung et al. Laser-driven 1 gev carbon ions from preheated diamond targets in the break-out afterburner regime. Phys. Plasmas, 20(8):083103, 2013.

[140] D. Jung et al. A novel high resolution ion wide angle spectrometer. Review of Scientific Instruments, 82(4):043301, 2011.

[141] L. Yin et al. Three-dimensional dynamics of breakout afterburner ion acceleration using high-contrast short-pulse laser and nanoscale targets. Phys. Rev. Lett., 107(4):045003, 2011.

[142] R. J. Gray et al. Azimuthal asymmetry in collective electron dynamics in relativistically transparent laser-foil interactions. New Journal of Physics, 16(9):093027, 2014.

[143] D. Jung et al. Scaling of ion energies in the relativistic-induced transparency regime. Laser and Particle Beams, 33(4):695, 2015.

[144] B. Hegelich et al. Experimental demonstration of particle energy, conversion efficiency and spectral shape required for ion-based fast ignition. Nuclear Fusion, 51(8):083011, 2011.

[145] A. A. Sahai et al. Relativistically induced transparency acceleration of light ions by an ultrashort laser pulse interacting with a heavy-ion-plasma density gradient. Physical Review E, 88(4):043105, 2013.

[146] B. Gonzalez-Izquierdo et al. Optically controlled dense current structures driven by relativistic plasma aperture-induceddiffraction. Nature Physics, 12(5):505512, 2016.

[147] B. Gonzalez-Izquierdo et al. Towards optical polarization control of laser-driven proton acceleration in foils undergoing relativistic transparency. Nature Communications, 7:12891, 2016.

[148] T. Maiman. Stimulated optical radiation in ruby. Nature, 187(4736):493, 1960.

[149] G. Mourou et al. Optics in the relativistic regime. Rev. Mod. Phys., 78(2):309371, 2006.

[150] S. Hooker Laser Physics. Oxford University Press, 2010.

[151] I. Ross et al. The prospects for ultrashort pulse duration and ultrahigh intensity using optical parametric chirped pulse amplifiers. Optics Communications, 144(1-3):125 – 133, 1997.

[152] C. Thaury et al. Plasma mirrors for ultrahigh-intensity optics. Nat Phys, 3(6):424429, 2007.

[153] I. Musgrave et al. Picosecond optical parametric chirped pulse amplifier as a preamplifier to generate high-energy seed pulses for contrast enhancement. Appl. Opt., 49(33):6558–6562, 2010.

[154] C. Danson et al. Vulcan petawatt: Design, operation and interactions at 5×10^{20} W/cm^2. Laser and Particle Beams, 23(1):87, 2005.

[155] C. Danson et al. Vulcan petawattan ultra-high-intensity interaction facility. Nuclear Fusion, 44(12):S239, 2004.

[156] M. Roth. The diagnostics of ultra-short pulse laser-produced plasma. Journal of Instrumentation, 6(9):R09001, 2011.

[157] J. F. Ziegler et al. Srim the stopping and range of ions in matter. Nuclear Instruments and Methods in Physics Research Section B: Beam Interactions with Materials and Atoms, 268(1112):1818 – 1823, 2010.

[158] K. Harres et al. Development and calibration of a thomson parabola with microchannel plate for the detection of laser-accelerated mev ions. Review of Scientific Instruments, 79(9):093306, 2008.

[159] C. G. Freeman et al. Calibration of a thomson parabola ion spectrometer and fujifilm imaging plate detectors for protons, deuterons, and alpha particles. Review of Scientific Instruments, 82(7):073301, 2011.

[160] D. Jung et al. Development of a high resolution and high dispersion thomson parabola. Review of Scientific Instruments, 82(1):013306, 2011.

[161] J. A. Cobble et al. High-resolution thomson parabola for ion analysis. Review of Scientific Instruments, 82(11):113504, 2011.

[162] D. Carroll et al. A modified thomson parabola spectrometer for high resolution multi-mev ion measurements - application to laser-driven ion acceleration. Nuclear Instruments and Methods in Physics Research Section A: Accelerators, Spectrometers, Detectors and Associated Equipment, 620(1):2327, 2010.

[163] D. Gwynne et al. Modified thomson spectrometer design for high energy, multi-species ion sources. Review of Scientific Instruments, 85(3):033304, 2014.

[164] Y. Amemiya et al. Imaging plate illuminates many fields. Nature, 336(6194):89–90, 1988.

[165] A. Manci et al. Absolute calibration of photostimulable image plate detectors used as (0.5-20 mev) high-energy proton detectors. Review of Scientific Instruments, 79(7):073301, 2008.

[166] D. Doria et al. Calibration of bas-tr image plate response to high energy (3-300 MeV) carbon ions. Review of Scientific Instruments, 86(12):123302, 2015.

[167] I. Musgrave et al. Review of laser diagnostics at the vulcan laser facility. High Power Laser Science and Engineering, 3, 2015.

[168] T. D. Arber et al. Contemporary particle-in-cell approach to laser-plasma modelling. Plasma Physics and Controlled Fusion, 57(11):113001, 2015.

[169] A. Macchi et al. Radiation pressure acceleration of ultrathin foils. New Journal of Physics, 12(4):045013, 2010.

[170] V. A. Vshivkov et al. Nonlinear electrodynamics of the interaction of ultra-intense laser pulses with a thin foil. Phys. Plasmas, 5(7):2727, 1998.

[171] A. Alejo et al. Characterisation of deuterium spectra from laser driven multi-species sources by employing differentially filtered image plate detectors in thomson spectrometers. Review of Scientific Instruments, 85(9):093303, Sep 2014.

[172] N. P. Dover et al. Buffered high charge spectrally-peaked proton beams in the relativistic-transparency regime. New Journal of Physics, 18(1):013038, 2016.

[173] F. Wagner et al. Simultaneous observation of angularly separated laser-driven proton beams accelerated via two different mechanisms. Phys. Plasmas, 22(6):063110, 2015.

[174] L. Willingale et al. Characterization of high-intensity laser propagation in the relativistic transparent regime through measurements of energetic proton beams. Phys. Rev. Lett., 102(12):125002, 2009.

[175] R. J. Gray et al. Laser pulse propagation and enhanced energy coupling to fast electrons in dense plasma gradients. New Journal of Physics, 16(11):113075, 2014.

[176] S. Kar et al. Plasma jets driven by ultraintense-laser interaction with thin foils. Phys. Rev. Lett., 100(22):225004, 2008.

[177] M. Borghesi et al. Relativistic channeling of a picosecond laser pulse in a near-critical preformed plasma. Phys. Rev. Lett., 78(5):879–882, 1997.

[178] A. Pukhov et al. Relativistic magnetic self-channeling of light in near-critical plasma: Three-dimensional particle-in-cell simulation. Phys. Rev. Lett., 76(21):3975, 1996.

[179] M. Schollmeier et al. Laser-to-hot-electron conversion limitations in relativistic laser matter interactions due to multi-picosecond dynamics. Phys. Plasmas, 22(4):043116, 2015.

[180] C. Ziener et al. Specular reflectivity of plasma mirrors as a function of intensity, pulse duration, and angle of incidence. Journal of Applied Physics, 93(1):768, 2003.

[181] L. Robson et al. Scaling of proton acceleration driven by petawatt-laser-plasma interactions. Nat Phys, 3(1):58–62, 2006.

[182] M. Temporal et al. Proton-beam driven fast ignition of inertially confined fuels: Reduction of the ignition energy by the use of two proton beams with radially shaped profiles. Phys. Plasmas, 15(5):052702, 2008.

[183] C. Hernandez-Gomez et al. The vulcan 10 pw project. Journal of Physics: Conference Series, 244(3):032006, 2010.

[184] J.-P. Chambaret et al. Extreme light infrastructure: laser architecture and major challenges. Proc. SPIE, 7721:77211D–77211D–15, 2010.

[185] G. Korn et al. Eli extreme light infrastructure science and technology with ultra-intense lasers. CLEO: 2013, page CTu2D.7, 2013.

[186] G. Mourou et al. The extreme light infrastructure: Optics' next horizon. Opt. Photon. News, 22(7):47–51, 2011.